HYDROGEN PERMEATION THROUGH MICROFABRICATED PALLADIUM-SILVER ALLOY MEMBRANES

A Dissertation
Presented to
The Academic Faculty

by

Logan Scott McLeod

In Partial Fulfillment
of the Requirements for the Degree
Doctor of Philosophy in the
George W. Woodruff School of Mechanical Engineering

Georgia Institute of Technology
December 2008

HYDROGEN PERMEATION THROUGH MICROFABRICATED PALLADIUM-SILVER ALLOY MEMBRANES

Approved by:

Dr. Andrei G. Fedorov, Advisor
School of Mechanical Engineering
Georgia Institute of Technology

Dr. F. Levent Degertekin, Advisor
School of Mechanical Engineering
Georgia Institute of Technology

Dr. J. Rhett Mayor
School of Mechanical Engineering
Georgia Institute of Technology

Dr. Meilin Liu
School of Materials Science and Engineering
Georgia Institute of Technology

Dr. William J. Koros
School of Chemical and Biomolecular Engineering
Georgia Institute of Technology

Date Approved: November 11, 2008

To my parents, Dr. Eric Scott McLeod and Dr. Renee Parnell McLeod

ACKNOWLEDGEMENTS

I would first like to thank my parents, Eric and Renee McLeod, without whose steadfast support I would surely have not come this far. Their support and love has been matched only by that of my soon-to-be wife, Cambria Price. For the sacrifices made and support given over the last six years, I am eternally grateful. I would also like to acknowledge the many individuals whose friendship has made my time at Georgia Tech an overwhelmingly enjoyable experience.

The contribution to this work made by my advisors, Dr. Andrei Fedorov and Dr. Levent Degertekin, cannot be understated. While their academic guidance has been exemplary, it has been their patience, generosity, kindness, and genuine interest in my success and well-being for which I am truly grateful.

TABLE OF CONTENTS

LIST OF TABLES

Page

LIST OF FIGURES

Page

NOMENCLATURE

List of Abbreviations

BCC	Body-Centered Cubic
DFT	Density Functional Theory
DRIE	Deep Reactive Ion Etch
FCC	Face-Centered Cubic
IC	Integrated Circuit
IUPAC	International Union of Pure and Applied Chemistry
MEMS	Microelectromechanical Systems
$PdAg_{25}$	Pd-Ag Alloy with 25% weight Ag
PECVD	Plasma-Enhanced Chemical Vapor Deposition
PPM	Parts Per Million
PSA	Pressure Swing Adsorption
PSS	Porous Stainless Steel
PVD	Physical Vapor Deposition
RIE	Reactive Ion Etch
sccm	Standard Cubic Centimeter per Minute
SEM	Scanning Electron Microscope
SSF	Selective Surface Flow
SZM	Structure Zone Model

List of Symbols

Å	Angstrom
$A_{Pd\text{-}Ag}$	Exposed Pd-Ag Surface Area
a	Lattice Parameter

C	Concentration
D	Diffusion Coefficient
D_o	Diffusion Coefficient Pre-Exponential Factor
d_h	Hydraulic Diameter
E	Activation Energy
$\mathrm{F}(\theta)$	Desorption Probability
FR_{Ar}	Flow Rate of Argon
H	Enthalpy or Channel Height
h	Partial Molar Enthalpy
ΔH^o	Enthalpy of Solution at Infinite Dilution
ΔH_{ch}	Heat of Chemisorption
ΔH_{ph}	Heat of Physisorption
h_m	Convective Mass Transfer Coefficient
J	Flux
K_s	Sieverts' Coefficient
k	Rate Constant
k_o	Desorption Pre-Exponential Factor
L	Channel Length
l_{ch}	Equilibrium Atomic Separation for Chemisorption
l_{ph}	Equilibrium Atomic Separation for Physisorption
$\dot{m}''$	Hydrogen Mass Flux
M_{H2}	Molecular Mass of Hydrogen
N_b	Density of Bulk Sites
N_s	Density of Surface Sites
P	Pressure

PP_{MS}	Hydrogen Partial Pressure Measured by the Mass Spectrometer
$\Re$	Universal Ideal Gas Constant
Re	Reynolds Number
R_{latt}	Atomic Radius of Host Lattice Atom
ΔS^{o}	Entropy of Solution at Infinite Dilution
$S(\theta)$	Sticking Coefficient
S	Solubility
S_o	Sticking Coefficient at Zero Coverage
s	Partial Molar Entropy
Sc	Schmidt Number
Sh	Sherwood Number
T	Temperature
t	Thickness
T_m	Melting Temperature
T_s	Substrate Temperature
V	Gas Velocity
W	Channel Width
w	Interaction Energy Between Adsorbed Hydrogen
X_{H2}	Mole Fraction of Hydrogen

Greek Letters

α_{AB}	Selectivity Between Species A and B
β_o	Bulk-Surface Pre-Exponential Factor
δ	Absolute Uncertainty
∂	Partial Derivative
γ	Fraction of Active Membrane Area

Γ	Molecular Bombardment Rate
ζ	Probability of Adsorption/Desorption over Empy/Occupied Sites
θ	Surface Coverage
θ_{oo}	Fraction of Nearest-Neighbor Vacant Sites
Φ	Permeability
μ	Chemical Potential
υ_j	Diffusional Jump Frequency
ν	Kinematic Viscosity
ν_o	Surface-Bulk Pre-Exponential Factor
χ	Atomic H:Pd Ratio

Superscripts

0	Standard State
g	Gas Phase
H	High Pressure Side (used when subscript already occupied)
in	Experimental Apparatus Inlet
L	Low Pressure Side (used when subscript already occupied)
memb	Membrane
n	Pressure Exponent
s	Within the Pd lattice (solid)

Subscripts

abs	Absorption
ads	Adsorption
B	Bulk
b-s	Bulk-Surface
des	Desorption

diff	Diffusion
elast.	Elastic Contribution
elect.	Electronic Contribution
eq	Equilibrium
H	High Pressure Side or Hydrogen Atom
H_2	Molecular Hydrogen
int	Intrinsic
L	Low Pressure Side
S	Surface
s-b	Surface-Bulk
tot	Total

SUMMARY

Energy efficient purification of hydrogen is an important technological challenge with broad applications in the chemical, petrochemical, metallurgical, pharmaceutical, textile and energy industries. Palladium-alloy membranes are particularly suited to this problem due to their high hydrogen permeability, thermal stability, and virtually infinite selectivity. In current systems hydrogen flux is observed to be inversely proportional to membrane thickness which is indicative of the interstitial diffusion mechanism of hydrogen permeation. This observation, along with the high cost of palladium, has motivated continuous efforts to decrease membrane thickness.

Theoretical modeling of membrane performance predicts that as membrane thickness continues to decrease, eventually the permeation rate will no longer be limited by diffusion through the bulk Pd but will become limited by desorption from the permeate surface. If it exists, this is a vital transition to pinpoint due to the fact that below this thickness membrane operating conditions will have a drastically different effect on hydrogen permeation behavior and no additional performance enhancements will result from further decreasing thickness. A handful of experimental results in the open literature contradict these modeling predictions. A new model is developed in this work to explain these contradictions by considering the non-ideal behavior of hydrogen solution into metals which has been neglected in previous models. Additionally, it has been demonstrated that hydrogen permeation through bulk Pd depends on

membrane microstructure, making deposition conditions and post-deposition thermal treatment important issues for repeatable performance.

The interplay of these issues on the performance of ultra-thin, Pd-Ag alloy hydrogen separating membranes is experimentally investigated. It is demonstrated that the hydrogen permeation behavior of sub-micrometer thick Pd-Ag alloy membranes exhibits diffusion-limited behavior in the context of the new model. The microstructure evolution during annealing is characterized and a correlation is drawn with the observed transient hydrogen permeation behavior during initial testing of a new membrane. In addition, two distinct failure modes of the microfabricated membranes are observed and the implications for future Pd-based membrane research are discussed.

CHAPTER 1
INTRODUCTION

Over the last century industrialization and development on the global scale has been powered by harnessing the energy stored in fossil fuels. Fossil fuels are cheap, simple to use and, until recently, seemingly in great abundance. The oxidation of the hydrogen and carbon in fossil fuels in a combustion process liberates a substantial amount of energy and leaves water vapor and carbon dioxide as byproducts. Due to exponentially increasing energy demand, fuel supply shortages, energy security and the mounting evidence that atmospheric concentrations of carbon dioxide are directly impacting global temperature, much recent attention in both the scientific community and popular media has focused on the search for clean, efficient, and renewable energy sources. Among the often touted solutions to the energy problem is the 'hydrogen economy'. In the proposed hydrogen economy molecular hydrogen is utilized as the energy carrier from the point of production to the point of use. Hydrogen is attractive as an energy carrier because it produces zero carbon emissions at the point of use, it is abundant, it can be combined with oxygen electrochemically in a fuel cell to efficiently produce electricity, and transportation and storage are less problematic than with electricity. Along with these potential benefits, hydrogen also has substantial problems. While hydrogen as an element is abundant, the molecular hydrogen needed for fuel is rather scarce. Nearly all terrestrial hydrogen is bound to oxygen in the form of water or to carbon in the previously mentioned hydrocarbon fossil fuels. Once hydrogen is liberated from one of these sources it must then be purified and either utilized immediately or transported/stored for later (or possibly remote) use. The production,

purification, and storage of hydrogen each represent a significant technological hurdle impeding the realization of a hydrogen economy [1].

Apart from the proposed hydrogen economy, there is already a substantial demand for hydrogen in the metallurgical, chemical, petrochemical, pharmaceutical, and textile industries. Roughly 2% of global primary energy utilization is directed to hydrogen production with annual yield of ~850 billion cubic meters. Of this, roughly 58% is dedicated to production of raw chemical materials such as ammonia, methanol, and hydrogen peroxide while an additional 37% is utilized by oil refineries for fractionation and upgrading of heavy hydrocarbons and contaminant removal [2]. The remaining 42 billion cubic meters is spread over a multitude of applications such as semi-conductor doping, fatty acid hydrogenation for food processing, metallurgical processing, and liquid rocket fuel [3]. Whether or not the world embraces the hydrogen economy, it is clear that there will always be a need for a cost-effective and efficient means to purify hydrogen.

1.1 Hydrogen Separation Techniques

The vast majority of hydrogen produced today, over 90%, comes from fossil fuel sources while the remaining fraction comes from electrolysis of water [4]. Depending on the application and available hydrocarbon source, fossil fuels undergo either a steam reforming process [Eq. (1.1)] or a partial oxidation process [Eq. (1.2)] to yield hydrogen.

$$C_nH_m + 2nH_2O \rightarrow nCO_2 + \left(\frac{m}{2} + 2n\right)H_2 \tag{1.1}$$

$$C_nH_m + \frac{n}{2}O_2 \rightarrow nCO + \frac{m}{2}H_2 \tag{1.2}$$

While the ideal reactions are shown above, in reality the resulting product stream is a mixture of H_2, CO_2, CO, H_2O, O_2, Ar, N_2, CH_4, and some heavier hydrocarbon residuals. Before the hydrogen can be utilized it must be separated from the other species in the product stream. Currently available technologies for hydrogen purification include pressure swing adsorption (PSA), cryogenic distillation, and membrane separation. The details of each of these processes along with their respective benefits and drawbacks will be discussed in the following sections. A general comparison is presented in Table 1.

Table 1: Comparison of Hydrogen Separation Techniques [5-9]

Process	H_2 Prod. Rate	Recovery	Purity	Capital Investment	Operating Cost
PSA	>100Nm^3/h	75-90%	>99.99%	Medium	High
Cryogenic Distillation	>500Nm^3/h	90-98%	95-99%	High	High
Membrane Separation	Variable	70-95%	70-~100%	Low	Low

1.1.1 Pressure Swing Adsorption

The Pressure Swing Adsorption process (PSA) is based on the principle that the equilibrium amount of impurities adsorbed on an adsorbent bed increases with increasing pressure. The impurities are removed from the gas stream at high pressure and subsequently released as the pressure "swings" back to a lower level to regenerate the bed. The two most important factors determining gas adsorption are volatility and polarity. Highly volatile and non-polar gases, such as hydrogen, have very little interaction with the adsorbent and pass through the bed exiting with relatively high purity (>99.99%) while other species are left behind. The preferential adsorption of

heavier/polar gas species results in a chromatographic separation from inlet to exit as shown in Figure 1.1. This distribution allows specific loading of the sorbent bed with varying adsorbent materials from inlet to exit to optimize the adsorption/desorption kinetics for each species at the appropriate point in the column. Typically these beds are loaded with a combination of silica gel, alumina, activated carbon, and zeolites to attain the desired performance characteristics [8, 10].

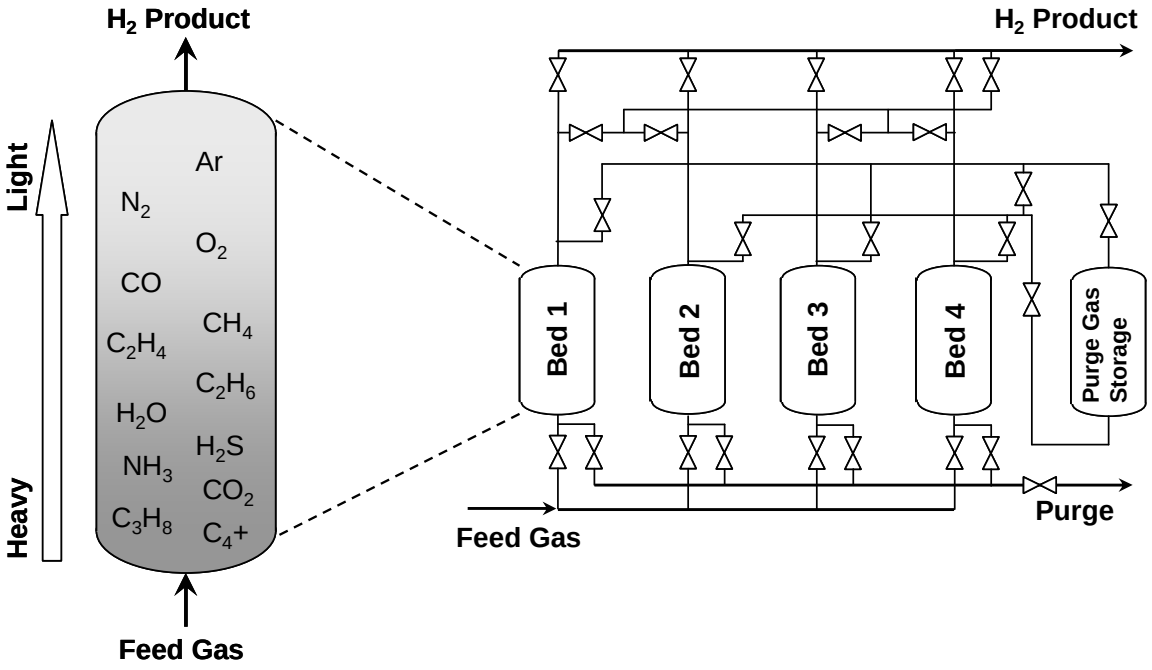

Figure 1.1: Typical four-bed PSA valve and plumbing configuration showing detail of gas adsorption within the sorbent bed.

Once the bed is saturated with impurities it must be regenerated by reducing the pressure and eventually purging the bed in the reverse direction to discharge the contaminant gas species. In order to supply hydrogen continuously the PSA system must have several beds, typically 4-16, operating in staggered succession. Each bed undergoes the following steps during a complete cycle:

1. Adsorption of impurities from the gas stream
2. Co-current depressurization
3. Counter-current depressurization
4. Purge at low pressure
5. Repressurization

In addition to allowing continuous hydrogen separation, having several beds operating in succession also allows the high pressure gas from one bed to be utilized to purge and repressurize the next bed in succession. This sequence of operation reduces the pressurization cost of the next bed and also reduces the hydrogen loss to the dead volume in each bed during the purge step. These savings can be substantial as the PSA feed system pressure is typically 10-60 bar and the purge/offgas pressure 1-10 bar. Figure 1.1 shows a schematic for a typical four bed PSA system. In order to ensure consistent hydrogen purity with minimal waste, careful control over the timing of bed utilization/regeneration must be maintained through precise actuation of the numerous valves in the system.

PSA plants in operation today are capable of producing hydrogen of 98-99.999% purity by mole with a recovery yield of 70-90% at a rate of up to 100,000 Nm^3/h (normal cubic meters per hour, where normal is referenced to standard temperature and pressure) [8, 11]. Due to the capital investment required to build a PSA plant, the logistics of plant operation, and the physical constraints dictated by the necessary impurity residence time on the sorbent bed, there is a minimum hydrogen production rate that must be maintained to economically justify plant operation. The smallest PSA plants in the world produce several hundred Nm^3/h of hydrogen [7].

1.1.2 Cryogenic Distillation

Distillation has been utilized to separate the components of a homogeneous liquid for hundreds, if not thousands, of years [5]. The principles of distillation are quite simple: heat is added to the liquid mixture under the appropriate thermodynamic conditions (temperature and pressure) such that one or more components of the mixture is/are preferentially evaporated into the gas phase. This vapor is collected and the separation is complete. In traditional distillation the main energy consumption requirement is the latent heat of vaporization which must be supplied to evaporate the various components of the mixture. In order to utilize distillation for gas separation the gas mixture must first be liquefied which can be highly energy intensive [12, 13].

For any distillation process, the efficacy of separation is dictated by the relative volatility, defined as the ratio of vapor pressures, of the species to be separated. This definition implies that the thermodynamic conditions are such that all species in the mixture are sub-critical. In the case of cryogenic hydrogen separation this is rarely the case and in fact the hydrogen separation is not due to distillation. As the gas mixture is cooled, the hydrogen is separated as the other species condense out of the gas phase. Due to the volatility of hydrogen relative to the other components of the mixture, adequate separation can be achieved simply by this condensation process. The benefit of this approach is that one has produced a pure hydrogen stream and the remaining gases have been sub-cooled and can now also be separated by the distillation process resulting in profitable by-products. Cryogenic distillation of hydrogen is nearly always performed when purified CO is also desired [14]. Carbon monoxide has become a vital chemical raw material for synthesis of polymers, ethanol, acetic acid, and oxo alcohols and it is

therefore lucrative to utilize a process which simultaneously produces pure product streams of both H_2 and CO. Cryogenic distillation produces a hydrogen stream of 95-99% purity and simultaneously delivers CO with ~97% purity [6].

1.1.3 Membrane Separation

Membranes have been utilized for hydrogen separation/purification since the early 1960's [15]. In the mid-1970's the first successful polymer hydrogen membrane was developed by DuPont using small-diameter, hollow fibers [16]. Over the next several years a handful of companies improved upon the polymer membranes developed by DuPont and brought several novel polymeric membrane materials to market [4, 17]. Due to fairly low hydrogen purity levels, these membranes were largely directed toward applications where high purity was not essential, such as H_2 reclamation from recycled refinery gas or ammonia purge gas. Recent investigations into hydrogen separation membranes cover an enormous variety in materials, separation mechanisms, and operating conditions, each of which may serve as an ideal option for a given application [4].

Membrane separation is based upon preferential mass transport of certain species through the membrane material. This leads to two possible approaches to gas separation: either the gas to be purified permeates the membrane more slowly than the other species and will therefore be enriched in the upstream, or retentate, side of the membrane, or the gas to be separated is a fast permeator and it will be enriched in the downstream, or permeate, side of the membrane. Hydrogen, being a much smaller molecule than most other species in any gas mixture, is typically the fast diffusing species and is therefore collected on the downstream side of the membrane. Economically, this is a potential

drawback of membrane separation compared with PSA as a re-compression cost must then be incurred if the hydrogen needs to be supplied at elevated pressure.

The most basic metrics by which a membrane can be evaluated are the permeability and selectivity. Permeability is defined as the product of flux of a gas species with the membrane thickness divided by the applied partial pressure difference across the membrane. Permeability is useful for comparison between different membrane materials under different test conditions as the effects of membrane thickness and applied pressure are removed leaving only the performance of the material. Selectivity is defined as the ratio of permeabilities between two different species. Materials with both high permeability and high selectivity for the gas species of interest are desirable. Higher permeability reduces the amount of membrane area required for a given application and therefore reduces cost. Higher selectivity increases the purity of the product gas.

In addition to permeability and selectivity, membrane strength, durability, operating environment (compatible gas species), operating temperature range, and susceptibility to fouling are all important factors to be considered in choosing a membrane for a given application.

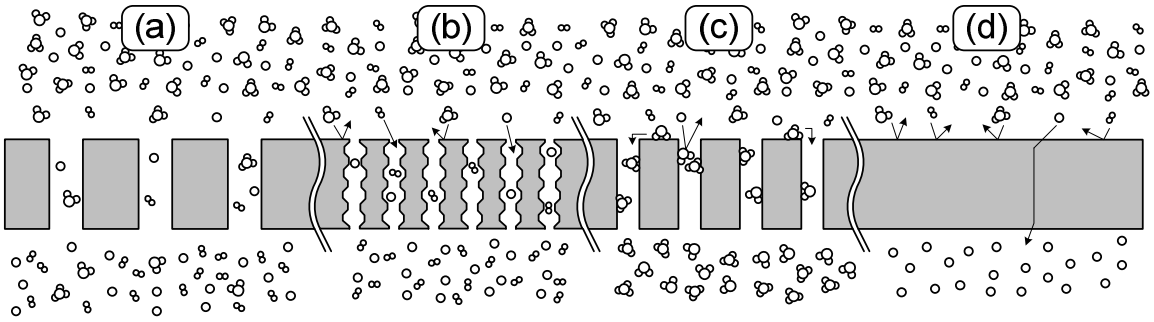

Figure 1.2: Transport mechanisms for membrane-based gas separation: (a) Knudsen diffusion (b) molecular sieving (c) surface diffusion and (d) solution-diffusion.

In any membrane, gas separation can be accomplished by one, or a combination of the following transport mechanisms (Figure 1.2): Knudsen diffusion, surface diffusion, molecular sieving, or solution-diffusion. Knudsen diffusion is characterized by pore dimensions which are smaller than the gas mean-free path [Figure 1.2(a)]. Since collisions with the pore wall occur more frequently than with other gas molecules these interactions dominate the overall transport. The Knudsen diffusion coefficient can be derived from kinetic theory and is proportional to the velocity of a gas species. Different gas species at the same temperature must have equivalent energy and since this energy is largely kinetic, heavier gas molecules have a lower velocity. In fact, the ratio of their velocities, and therefore their relative Knudsen diffusion rate, is proportional to the inverse ratio of the gas molecular weights to the one-half power. Generally, this mechanism alone does not provide adequate selectivity for most applications [18]. Molecular sieving membranes are made either of rigid crystalline structures with well-defined pore size or of tightly-packed amorphous materials with a narrow distribution of pore sizes. In either case, pore size must be below ~10 angstroms (Å) for molecular sieving to occur. These pores physically exclude gas molecules of larger dimensions and can therefore potentially provide excellent selectivity [Figure 1.2(b)]. Surface diffusion involves adsorption of the gas species on the membrane surface, followed by diffusion along the surface through pores or through defects/grain boundaries from one surface to the other [Figure 1.2(c)]. This method has the advantage that the adsorbing species, the one which selectively permeates, can be isolated based on specific surface chemistry. Typically this approach allows larger gas species to permeate more quickly and in some cases their adsorption on the surface blocks the pore structure almost entirely such that

small species cannot penetrate the membrane. This is the basis for the carbon surface-selective flow (SSF) membranes which will be discussed in more detail later. The final mechanism is solution-diffusion [Figure 1.2(d)]. As indicated by the name, the first step in this mechanism is absorption of the gas species into the membrane on the upstream surface. Once absorbed, the gas must diffuse through the membrane and then desorb from the downstream surface. The permeation rate for this process is controlled by both the solubility of the gas species in the membrane and the diffusion coefficient of the absorbed species through the membrane.

In addition to the mechanism employed for separation, it is often useful to categorize membranes based on the materials used. Hydrogen membranes can be broadly categorized into polymer (organic), ceramic, carbon, and metallic. This classification allows a more direct comparison of membrane permeability, selectivity, operating conditions and cost. The permeability and selectivity of the various membrane materials are compared in Figure 1.6. Other relevant information about each membrane type can be found in Table 2.

1.1.3.1 Dense Polymeric Membranes

Polymers are the most widely utilized materials for gas separation membranes [19]. They are preferred for their manufacturability and low cost but lack extremely high selectivity (Table 2) and are limited to low operating temperatures (typically less than 100 ^{o}C).

Polymeric membranes can be further subdivided into either glassy or rubbery depending on whether the operation temperature is above (rubbery) or below (glassy) the glass transition temperature of the polymer. Polymer membranes operate based on a

solution-diffusion mechanism. After absorbing into the membrane, diffusion occurs through creation of local, transient gaps in the polymer matrix by thermally-stimulated polymer chain motion [20, 21]. The permeability of these membranes is dictated by both the solubility of a given gas species in the membrane and the diffusion coefficient for that gas species in the membrane. It is therefore typical to discuss both the solubility selectivity and diffusion selectivity in relation to the total permeability. In general, solubility selectivity favors larger, less volatile molecules, while diffusion selectivity favors smaller molecules which can more easily penetrate the small transient gaps in the polymer matrix [21, 22]. The selectivity of glassy polymers is dominated by diffusion selectivity, which is dictated by the size difference between gas molecules and the size-sieving ability of the material. Due to the additional freedom for motion in rubbery polymers, most gas species exhibit similar diffusion rates and the selectivity is therefore largely dependant on solubility differences between different gases. As a general rule, rubbery polymers have higher flux with lower selectivity and glassy polymers have lower flux but higher selectivity. For hydrogen separations where high purity is required, glassy polymers are employed to take advantage of the diffusion selectivity.

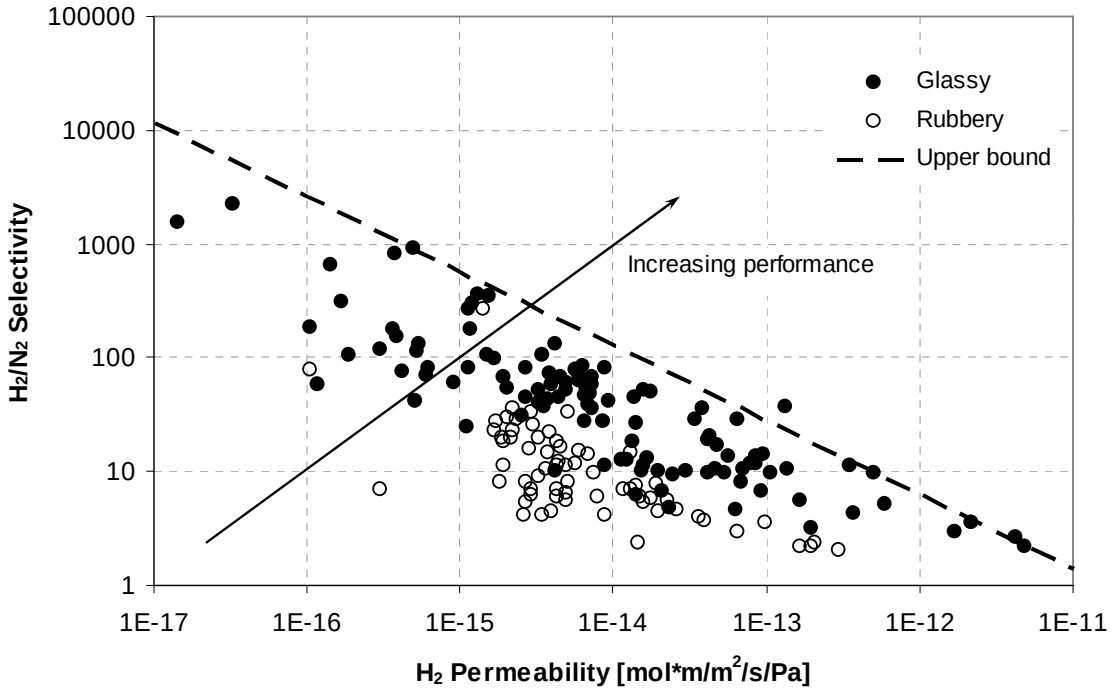

Figure 1.3: Permeability vs. selectivity trade-off for polymeric separations of H_2 and N_2 [23]

After years of steady research in the field of polymer membranes, it was observed in 1991 by Robeson that there was a consistent trade-off between polymer membrane permeability and selectivity [23]. When all available data for a given separation (H_2 from N_2, for example) is plotted with hydrogen permeability on the abscissa and selectivity on the ordinate, all of the points lie beneath a single line (on a log-log scale) as shown in Figure 1.3. The equation of this line is found from a regression to determine the two coefficients, *k* and *n*, in Eq. (1.3) relating the permeability of species A, Φ_A, to the selectivity between species A and B, α_{AB}. Upon rearranging into Eq. (1.4) it is clear that the slope of the upper bound curve is equal to 1/*n*.

$$\Phi_A = k\alpha_{AB}^n \tag{1.3}$$

$$\alpha_{AB} = k^{-1/n} \cdot \Phi_A^{1/n} \tag{1.4}$$

Robeson initially calculated the upper bound curve for nine pairs of gases and noted that there was an excellent correlation between the slope of the curve and the difference in kinetic diameter of the gas species. This correlation indicates that there is a fundamental limit to the potential of polymer membranes for gas separations due to the diffusion mechanism in these materials. Robeson revisited his previous correlations in a recent paper to catalogue the advances over the last seventeen years and noted that although the y-intercept of nearly all curves had shifted slightly upward, the slopes have remained nearly constant despite intense research efforts [24]. The newly calculated upper bound curves for hydrogen separations are shown in Figure 1.4. As the upper bound, all polymer-based separations will lie on or below these performance curves.

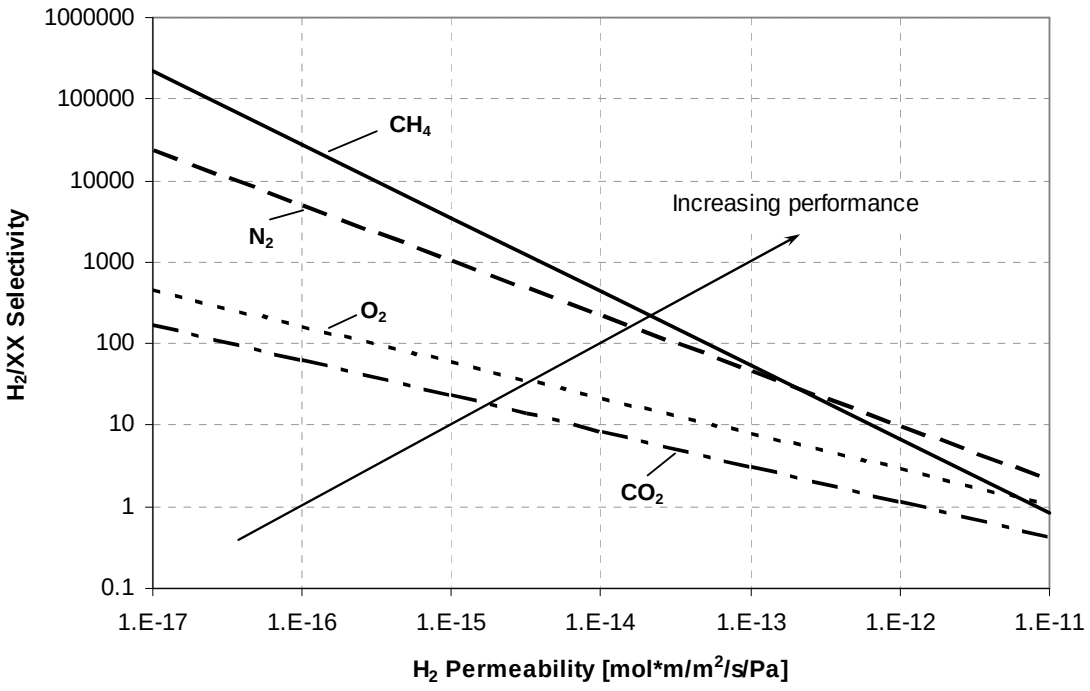

Figure 1.4: Upper bound performance curves for polymer membrane based separations of H_2 from selected gas species [24].

1.1.3.2 Ceramic Membranes

Ceramic membranes can also be subdivided into several categories: porous silica, crystalline zeolites, and dense perovskites. Porous silica is an amorphous membrane with an interconnected network of micropores of approximately 5-20Å [25, 26]. Transport through silica membranes can be classified as a combination of Knudsen diffusion, surface diffusion and molecular sieving as gas molecules traverse the tortuous, interconnected pore network. Due to high mass transfer resistance through the microporous silica, these films are kept as thin as possible and are typically deposited onto porous support layers to provide mechanical strength and minimize the overall mass transfer resistance. The International Union of Pure and Applied Chemistry (IUPAC) has classified porous materials according to pore diameter into the following categories: microporous - less than 2 nanometers (nm), mesoporous - 2 to 50 nm, and macroporous - greater than 50 nm. As shown in Figure 1.5, microporous silica is deposited onto a mesoporous transition layer and this structure is supported by increasingly porous and thick layers. The mesoporous and macroporous layers are composed of alumina, zirconia, titania, or silica [4, 27].

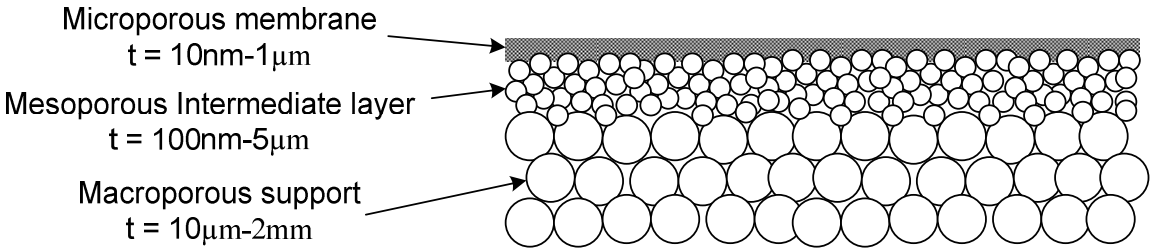

Figure 1.5: Graded porous support structure for ceramic membranes. Ranges given are typical layer thickness [25].

Zeolites are crystalline inorganic materials which are very similar to silica with respect to operating conditions, performance and implementation. The main distinction

is that the pore structure of a zeolite is defined by the geometry of the crystalline framework from which it is made. Zeolite pores are highly uniform and have diameters of 4-10Å depending on the particular zeolite material. Although the pore structure is highly uniform, it is virtually impossible to grow a single zeolite crystal across the entire surface of a membrane. Therefore, there is always the potential for gas transport through the inter-granular domains detracting from the ideal molecular sieving behavior of the zeolite.

Due to the inert nature of the materials used in silica and zeolite membranes, they are ideal for hydrogen separation from harsh gas streams at elevated temperatures of 200-600 °C. They exhibit good hydrogen permeability and selectivity but more work is needed to reproducibly manufacture defect-free films over large surface areas. Operational stability over extended periods, especially for silica in the presence of steam, has been shown to be problematic [25, 27-29]. The performance of silica and zeolite materials is superimposed on the polymer performance curves in Figure 1.6 for comparison. It can be seen that they have superior performance, but current issues with fabrication, cost, and stability must be overcome before large-scale implementation is practical.

The other class of ceramic hydrogen membrane is the dense ceramic, typically perovskites. These materials are well known for their mixed ionic-electronic conductivites and have been thoroughly studied as oxygen transport membranes [30]. They have received less attention as protonic-electronic conductors although they show promise for this application [31, 32]. Transport is through the solution-diffusion mechanism with the addition of an electrochemical surface reaction providing excellent

selectivity. Although protonic conductivity can be high, on the order of the hydrogen transport rates through the other ceramic materials, there are several issues which must be resolved before these materials can be utilized. Since the protons are ionized on the surface and transported independently of the electrons, both protonic and electronic conductivity must be high otherwise electron transport may limit hydrogen permeation rates. Additionally, proton transport needs to dominate ion transport rather than oxygen ions which may become problematic in oxygen or water vapor containing environments. The last issue which must be overcome for these materials is the kinetics of the electrochemical surface reaction. Hydrogen dissociation on the surface can be sluggish and the rate of this process must be increased to make these materials viable gas separation media [31].

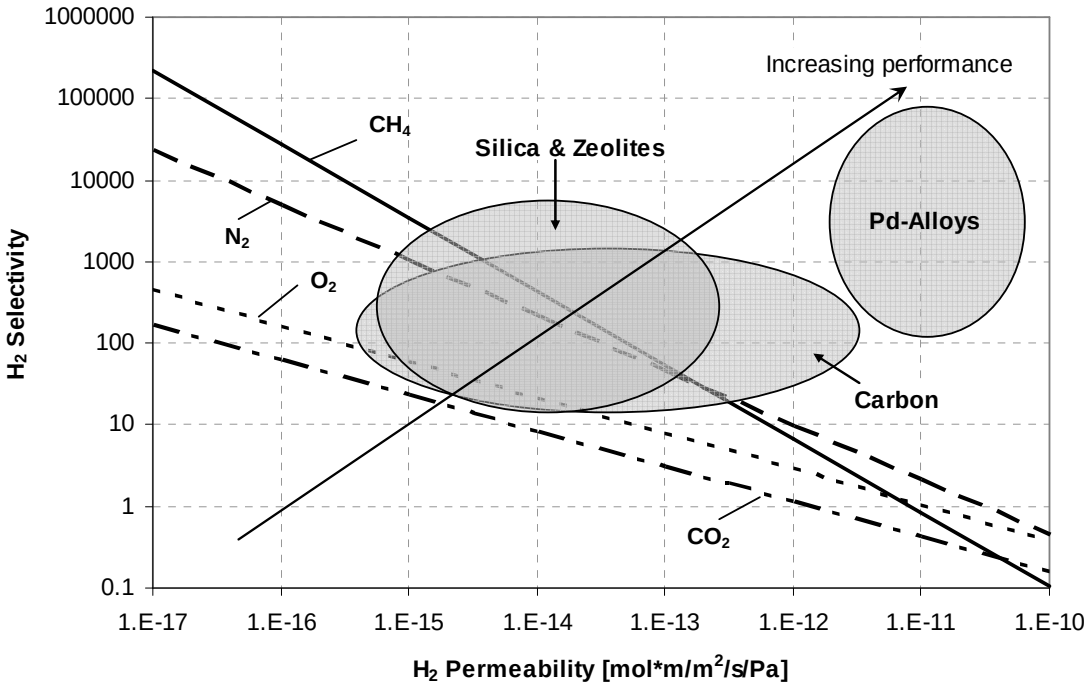

Figure 1.6: Relative performance of the various H_2 membrane materials. Curves are the upper bounds for polymer membrane performance from [24]. Silica and zeolite membrane data from [25] converted to permeability assuming membrane thickness of 100 nm. Carbon membrane data from [33]. Pd-alloy membrane data from [34-38].

1.1.3.3 Carbon Membranes

Carbon membranes for hydrogen separation are generally microporous amorphous carbon films. Amorphous carbon membranes are made starting with a polymer precursor deposition, often on a meso/macroporous graphite support. The polymer is heated in an inert environment to undergo a pyrolysis/carbonization reaction. During this process the channeling of small volatile molecules out of the polymer produces the microporous structure. After this step the final pore size can either be increased with an oxidation step or decreased by depositing additional material using chemical vapor deposition [39]. Porous carbon membranes utilize either a molecular sieving mechanism to selectively permeate hydrogen or they can utilize selective surface diffusion to permeate larger molecules and exclude hydrogen. The latter mechanism was successfully demonstrated by Rao and Sircar in 1993 [40-42]. The permeability of pure hydrogen through their carbon surface selective flow (SSF) membranes was reduced by several orders of magnitude when hydrogen was mixed with hydrocarbons, indicating that adsorption and surface diffusion were inhibiting gas-phase transport of hydrogen. This mechanism is attractive for hydrogen separation as the purified hydrogen remains in the high pressure retentate stream and recompression is not necessary.

Carbon membranes exhibit high permeability and are stable at temperatures up to 900 °C [28]. Their permeability and selectivity behavior is compared with the other materials in Figure 1.6. Current issues with carbon membranes include reduced performance in the presence of strongly adsorbing vapors, brittleness, cost, and the inability to operate in an oxidizing environment [28, 33, 39, 43].

1.1.3.4 Metallic Membranes

In 1962 the National Cylinder Gas division of the Chemetron Co. constructed a commercial-scale plant capable of producing 115,000 ft^3/day of hydrogen with less than 0.1 parts per million (PPM) of impurities [15]. This plant utilized thin Pd-alloy tubes and was the first commercial implementation of a hydrogen membrane. Interestingly, it had been almost 100 years since the original discovery in 1866 that certain metals were highly permeable to hydrogen [44]. The long delay was primarily due to the fact that most metals that are permeable to hydrogen also form a metal hydride with different physical characteristics than the metal. Transition into a metal hydride causes membrane failure and is typically labeled hydrogen embrittlement. Metal membranes were able to be utilized commercially after the discovery by Hunter in 1960 that alloying palladium with silver eliminated the embrittlement and failure issues that plagued pure Pd and other metals [45]. The low hydrogen flux achievable with these relatively thick-walled early Pd-alloy tubes, coupled with the high cost of Pd, made this approach to hydrogen purification uneconomical and these plants were not widely adopted. However, small-scale hydrogen purification systems based on this technology where ultra-high purity is required, such as laboratory research and semiconductor manufacture, are in use and commercially available today [27].

Hydrogen permeation through metals occurs via the solution-diffusion mechanism. Due to the fact that hydrogen adsorption onto the metal surface is dissociative, this process is sometimes called reactive or catalytic solution-diffusion [46]. Palladium-alloys, especially with copper and silver, are the primary metals utilized due to their high surface reactivity for hydrogen dissociation, resistance to embrittlement, and

high hydrogen permeability. The permeability of Pd-alloys by hydrogen is the highest of all membrane materials as shown in Figure 1.6 and they also exhibit virtually infinite selectivity. Pd-alloys are typically operated at temperatures from 300-600 °C and exhibit good mechanical properties. Although Pd-alloys have higher permeability than other membrane materials the achievable flux is often limited by the thickness of the metal films. While other materials are consistently fabricated with a thickness less than 100nm, defect-free metal membranes with a thickness of less than a few microns have been elusive [38]. In addition, metal membranes are susceptible to fouling/poisoning of the surface from gases such as H_2S and HCl and the high cost of Pd makes these membranes expensive.

Table 2: Properties of Selected Hydrogen Separation Membranes [27, 28]

	Membrane Type			
	Dense Polymer	Porous Ceramic	Metallic	Porous Carbon
Temperature	< 100°C	200-600 °C	200-600 °C	500-900 °C
H_2 Selectivity	5-500	10-5000	>1000	10-1000
H_2 Flux[a]	0.1-1	60-300	100-1000	10-200
Stability Issues	swelling, compaction	water vapor	embrittlement	brittle, oxidizing environments
Poisoning Issues	HCl, SO_x	none	H_2S, HCl, CO	strongly adsorbing vapors
Materials	polymers	silica, zeolites	Pd alloys	carbon
Transport Mechanism	solution-diffusion	molecular sieving	solution-diffusion	molecular sieving

[a] *units are 10^{-3} mol/m^2/s at a pressure difference of 101kPa*

1.2 Research Scope

Due to their superior permeability and selectivity over other membrane materials, metal membranes have been the subject of extensive research [36]. One of the primary technological challenges with metal membranes is the ability to manufacture extremely thin membranes without defects. For metal membranes, the desire to minimize thickness is compounded by the solution-diffusion transport mechanism. When diffusion limits the overall hydrogen transport, the hydrogen flux is inversely proportional to the membrane thickness: cutting the membrane thickness in half will double the hydrogen flux. For a given application where hydrogen flow rate is fixed, doubling the flux reduces the required membrane area by a factor of two. Therefore, rather than simply reducing the amount of membrane material by a factor of two, halving the membrane thickness reduces material requirements by a factor of four. When membrane cost is largely determined by the cost of materials, as for Pd-based membranes, the dependence of cost on the square of the thickness ($\propto t^2$) provides significant incentive to find novel methods of minimizing thickness.

The concept of using a thin, selective membrane layer coupled with a porous support layer for mechanical strength (Figure 1.5) is not a new idea. In fact, it was this approach which brought membrane separation into the mainstream in the early 1960's in the form of the Loeb-Sourirajan process for making high-flux, anisotropic, reverse-osmosis membranes for water purification [47]. This concept was first applied to metal membranes in 1984 with flash evaporation of $LaNi_5$ onto a porous stainless-steel substrate [48, 49]. Through the late 1980's and early 1990's Uemiya and Kikuchi pushed the frontiers of dense metal membranes for hydrogen purification with thin Pd and Pd-

alloy films on a variety of porous substrates [50-53]. Since that time, dozens of papers have been catalogued on this subject covering nearly every combination of porous substrate and thin-film deposition method [36, 38]. The most common substrates utilized are porous Vycor glass (silica glass), alumina, and stainless steel.

While this approach does allow the thickness of the metal film to be reduced substantially, there are several drawbacks. In order to maintain high selectivity and create a film which is free from defects, the metal layer must be significantly thicker than the largest pores on the substrate surface (typically by a factor of 2-4). This ensures that all pores are filled and the metal layer is continuous across the entire surface. By itself this is not a major problem as both Vycor and γ-alumina can be produced with a pore size down to 4-5 nanometers. Unfortunately as pore size is reduced, film adhesion becomes problematic as the metal layer can no longer penetrate the substrate to create an 'anchor effect' [38]. The adhesion problem is compounded by the large difference in coefficient of thermal expansion between the ceramic substrates and the metal film. Porous stainless steel (PSS) substrates are attractive from this standpoint as they have a similar coefficient of thermal expansion to Pd. However, PSS substrates are problematic as the diffusion and alloy formation between the substrate and Pd layer reduces the hydrogen permeability. This problem can be avoided to a large extent by deposition of a diffusion barrier between the substrate and Pd film, often a thin TiN coating [54]. In addition to the adhesion issue with a microporous support, there is also a more fundamental problem. As the substrate porosity is reduced the substrate itself starts to inhibit the hydrogen transport rate and offset the benefit of reducing membrane thickness.

Reducing membrane thickness will increase hydrogen flux only if hydrogen permeation is controlled by the diffusion process through the membrane. As the membrane thickness is continually decreased it becomes increasingly likely that a different process, namely a surface process such as adsorption, absorption, or desorption, will limit the hydrogen flux through the metal. Once this occurs, further reducing membrane thickness will not result in flux increase. In an effort to predict this transition detailed modeling of the permeation process has been performed [55]. This modeling has predicted that the hydrogen permeation rate will be limited by desorption from the downstream surface for thin Pd membranes under certain operating conditions. Unfortunately, due to additional transport resistance imposed by the porous substrate it is unlikely that this transition in permeation regime will be encountered using a thin, supported Pd membrane. In the literature there are a few reports of relatively thick (>100μm), free-standing Pd-Ag alloy membranes at low temperatures with behavior which appears to be consistent with the modeling predictions for a transition into desorption limited behavior. Due to the large thickness of these membranes it is unlikely that any process other than diffusion is limiting the hydrogen permeation rate. Before any critical evaluation of the performance of thin membranes can be completed this apparent discrepancy must be resolved.

Several recent studies have utilized microfabrication techniques developed in the microelectromechanical systems (MEMS) and integrated circuit (IC) industries to fabricate free-standing metal membranes with a thickness on the order of one micrometer or less [56-61]. This approach represents an ideal platform to probe the fundamental limitations of hydrogen permeation through metal membranes due to the removal of the

porous support. Although this approach has already been utilized to produce sub-micrometer, free-standing membranes, the major question which previous investigators have sought to answer was the feasibility of manufacturing using microfabrication techniques. There has been no systematic characterization of the performance of these membranes to determine whether any fundamental performance limitation has been reached.

In this work the current models for predicting hydrogen permeation behavior will be critically evaluated. Recognizing that the non-ideal solution behavior of hydrogen is a key area where the existing models are inadequate, a new model is developed to more accurately represent the behavior of hydrogen in Pd-alloy membranes. The new model is utilized to demonstrate that the existing permeation results for thick membranes are indicative of true diffusion limited permeation rather than a transition into desorption limited behavior. Armed with the improved model, the hydrogen permeation behavior through thin, free-standing membranes, is studied both theoretically and experimentally to determine whether or not any fundamental limitations have been reached.

In order to further validate the model predictions and determine whether a fundamental shift in permeation regime has been reached, a novel method is developed to fabricate free-standing metal membranes with a thickness of less than 1μm. The hydrogen permeation behavior of these membranes is measured and interpreted within the context of the modified permeation model. In every membrane tested, unexpected transient results were encountered during the first few hours of experiments. These results are attributed to the complex microstructure of the thin metal films and the

evolution of this microstructure as the membranes are effectively annealed during high temperature testing.

CHAPTER 2
METAL MEMBRANES FOR HYDROGEN SEPARATION

Interest in the interaction of hydrogen with transition metals began in the early 1860's with the work of Deville and Troost who measured the permeability of hydrogen through heated iron and platinum [62]. Building on their work, in 1866 Thomas Graham was the first to measure the permeability of palladium by hydrogen and he also noted that the metal "occluded" an enormous volume of hydrogen upon cooling which could be subsequently released by reheating. More importantly, Graham noted that while palladium was highly permeable to hydrogen it was virtually impermeable by all other gases tested, laying the groundwork for the future use of palladium in a hydrogen purification membrane [44]. Since that time, arguably there have been more studies on the Pd-H system than any other gas-metal system.

Due to the enormous body of knowledge pertaining to the interaction of hydrogen with metals, and in particular to the Pd-H system, it would be impossible to present a complete literature survey on the subject in the present document. However, several texts on the topic have already been published to which the interested reader is directed for further information [63-70]. The purpose of this chapter is rather to present the relevant fundamental aspects of the interaction of hydrogen with metals in the context of membrane transport. The springboard for this discussion will be Fick's Law for steady-state flux which provides several necessary criteria for a material to be useful as a purification membrane. These criteria form a logical framework for the presentation of hydrogen-metal interactions and particularly how the properties of these interactions make certain metals highly useful as hydrogen purification membranes.

2.1 Diffusion Equation in Membranes

As a starting point for the discussion of membrane separation, consider Fick's Law for steady-state diffusion, Eq. (2.1).

$$\bar{J}_i = -\frac{D \cdot C_i}{RT} \cdot \nabla \mu_i \tag{2.1}$$

Fick's Law states that the diffusional flux of species i (J_i) is proportional to the diffusion coefficient (D) and the gradient of chemical potential of species i (μ_i). In the absence of significant gradients other than concentration (strain, temperature, etc.), using the dilute solution approximation, and applied to a one dimensional membrane, Fick's Law can be reduced to Eq. (2.2) where t is the membrane thickness and C is the concentration near the membrane surface. The subscripts H and L denote the surface of the membrane in contact with the high and low hydrogen pressure respectively.

$$J = -D\frac{(C_H - C_L)}{t} \tag{2.2}$$

Going one step further and assuming that the process of hydrogen diffusion through the membrane is much slower than the processes occurring on the membrane surface permits a useful modification to Eq. (2.2). Under this assumption each surface is in a quasi-equilibrium state with the surrounding gas environment and therefore the concentration of hydrogen near the surface can be described by the equilibrium solubility of hydrogen in the membrane material at the prescribed temperature and pressure. In general the solubility is proportional to the gas pressure raised to any one of a number of exponents depending on the mechanism of gas absorption. For example, in Henry's Law the pressure exponent has a value of unity while in Sieverts' Law the exponent takes a value of one-half. A generic form for the equilibrium concentration of absorbed gas can

therefore be formulated as Eq. (2.3) where S is the solubility coefficient and n is the appropriate pressure exponent. Combining this relation with Fick's Law leads to Eq. (2.4).

$$C = S \cdot P^n \tag{2.3}$$

$$J = -\frac{DS}{t}\left((P_H)^n - (P_L)^n\right) \tag{2.4}$$

Based on Eq. (2.4), several assertions can be made regarding the desired properties of a membrane for the purpose of separating a given species from a mixture:

1. The product of diffusion coefficient and solubility coefficient, also known as permeability, should be large for the species of interest and small for all other species.
2. The membrane should be structurally robust in order to withstand a moderate pressure difference to drive permeation.
3. The membrane should be made as thin as possible

The remainder of this chapter is dedicated to exploring the first of these criteria and how this requirement naturally leads to selection of Pd-alloy membranes for hydrogen purification.

2.2 The Nature and Location of Hydrogen in Metals

Much of the early work on hydrogen absorption by transition metals was performed by Sieverts in the 1910's [71-73]. Sieverts observed that over a wide range of temperature and pressure the concentration of absorbed hydrogen in many metals (C_H) was proportional to the square root of the gas-phase hydrogen pressure (P_{H2}). This is

expressed by what is now known as Sieverts' law, Eq. (2.5), where the coefficient of proportionality, K_S, is known as Sieverts' coefficient.

$$C_H = K_S P_{H2}^{1/2} \tag{2.5}$$

If it is assumed that hydrogen is dissolved into the metal in the form of a dissociated hydrogen atom (H_{ab}) then Eq. (2.6) will describe the chemical reaction.

$$\frac{1}{2} H_{2(g)} \rightleftarrows H_{ab} \tag{2.6}$$

At equilibrium, the chemical potentials of each state will be equal and the equilibrium constant (K_{eq}) for reaction (2.6) will be described by Eq. (2.7) where a_H is the thermodynamic activity of the dissolved hydrogen and f_{H2} is the fugacity of the gaseous hydrogen.

$$K_{eq} = \frac{a_H}{f_{H2}^{1/2}} \tag{2.7}$$

At low concentrations of dissolved hydrogen the thermodynamic activity is proportional to the concentration, $a_H = c_1 C_H$ (with c_1 an arbitrary constant). Since the critical temperature and pressure for hydrogen are, respectively, 33 K and 1.3 MPa, it is safe to assume that under all conditions of interest in this study hydrogen will behave as an ideal gas and therefore the fugacity is simply proportional to pressure, $f_{H2} = c_2 P_{H2}$ (with c_2 an arbitrary constant). Incorporating these modifications into Eq. (2.7) leads to Eq. (2.8) and rearranging terms results in Eq. (2.9).

$$K_{eq} = \frac{c_1 C_H}{\left(c_2 P_{H2}\right)^{1/2}} \tag{2.8}$$

$$C_H = \left(\frac{K_{eq} c_2^{1/2}}{c_1} \right) P_{H2}^{1/2} \tag{2.9}$$

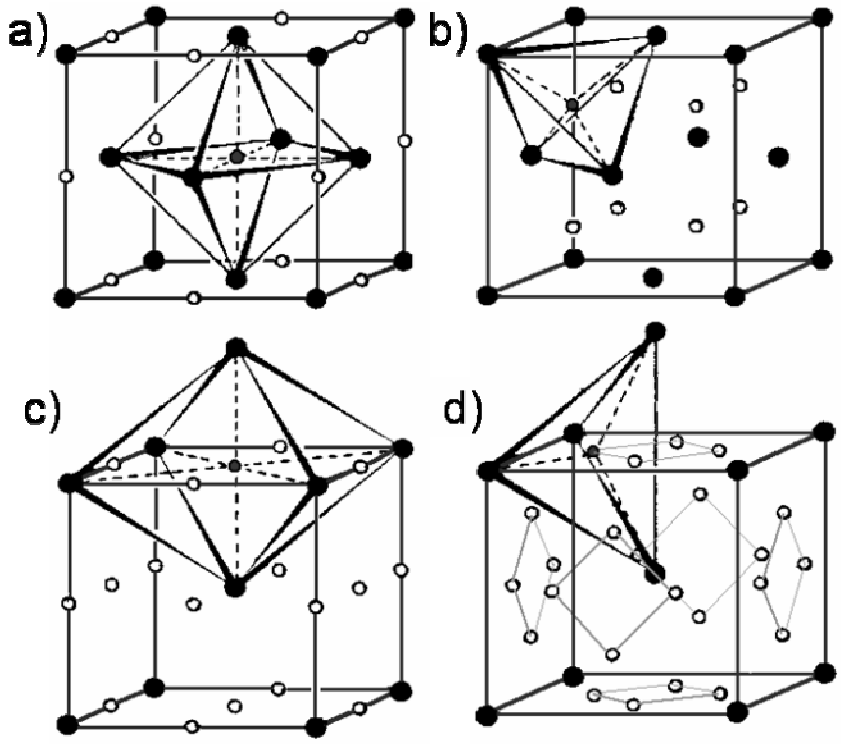

Figure 2.1: a) octahedral and b) tetrahedral interstitial locations in the FCC lattice and c) octahedral and d) tetrahedral interstitial locations in the BCC lattice. Dark circles are lattice locations, white circles are interstitial locations.

The equivalence of Sieverts' Law [Eq. (2.5)] with Eq. (2.9) confirms the assumption that hydrogen absorption by metals which obey Sieverts' Law is dissociative. The use of the simple chemical reaction of Eq. (2.6) to describe hydrogen absorption also implies that there is no interaction between the absorbed hydrogen atoms, i.e. absorbed hydrogen behaves as an ideal solution. Therefore Sieverts' Law is only applicable when hydrogen is a dilute solute in the metal.

The observed expansion of metal samples upon absorption of hydrogen gives further information about the state of the dissolved gas. The volume occupied by a hydrogen atom is substantially smaller than the volume occupied by the host metal atom. Therefore, the expansion of the metal indicates that the hydrogen must occupy interstitial sites within the lattice. This conclusion has been confirmed by x-ray and neutron

diffraction studies [64, 74]. In the face-centered cubic (FCC) and hexagonal close packed (HCP) structures there are two tetrahedral interstitial sites and one octahedral site per host atom (Figure 2.1a,b). In the body-centered cubic (BCC) structure there are three octahedral and six tetrahedral interstitial sites per host atom (Figure 2.1c,d). The distinction between sites is that the tetrahedral location is centered between four neighboring atoms, the vertices of a four-sided tetrahedron, while the octahedral location is centered between six neighboring atoms, the vertices of an eight-sided octahedron. This geometry is elucidated in Figure 2.1. The question as to whether the hydrogen interstitials occupy the tetrahedral or octahedral sites can be answered simply by noting the relative sizes of these locations for a given lattice structure. Hydrogen will preferentially occupy the sites with a larger free volume as these are the locations of local minima of potential energy. The size of the interstitial hole can be estimated by calculating the length of the vector from a nearest neighbor atom to the interstitial location. The length of this vector minus the radius of the host atom (R_{latt}) gives the approximate radius of the interstitial hole. In the FCC and HCP structures the octahedral interstitial radius is ~$0.41R_{latt}$ while the tetrahedral interstitial radius is ~$0.22R_{latt}$. In the BCC structure the tetrahedral interstitial radius is ~$0.29R_{latt}$ while the octahedral interstitial radius is ~$0.15R_{latt}$. From these numbers we can conclude that the absorbed hydrogen will occupy the octahedral sites in FCC and HCP metals while it will occupy the tetrahedral sites in BCC metals.

2.3 Solubility of Hydrogen in Metals

Figure 2.2 shows the hydrogen solubility in several transition metals. From this data it would seem that Pd is not the best choice for membrane materials due to the relatively

small hydrogen solubility. However, the ordinate on Figure 2.2 is the atomic ratio of hydrogen to metal, meaning that the majority of these 'solutions' are predominantly composed of hydrogen. While this is clearly a violation of the dilute solution condition necessary for the validity of Sieverts' Law, it is more importantly an indication of a change in the fundamental nature of the hydrogen-metal compound. The formation of a metal hydride invariably involves a substantial volumetric increase which is typically accompanied by a change in the structure of the metal sublattice. For example vanadium has a BCC structure but the monohydride VH has a body-centered tetragonal structure. Under appropriate conditions vanadium will also form a dihydride, VH_2, and the metal sublattice in this structure is FCC [75]. One of the few exceptions to this hydride structural change is Pd which forms a non-stoichiometric hydride, $PdH_{0.6}$, and maintains the FCC structure of the pure metal. However, even for this low-order hydride which does not undergo a structural change there is a discontinuous increase of lattice parameter from 3.89Å to 4.03Å resulting in a roughly 11% volumetric increase upon formation of the hydride. In addition to the structural and volumetric changes which occur upon formation of a metal hydride there is also typically a substantial increase in brittleness of the material due to the induced strain from the interstitial hydrogen.

In applications of membrane separation where hydrogen loading may be cyclical and concentrations will vary drastically across the thickness of the membrane, the large volumetric and structural changes associated with hydride formation inevitably lead to membrane failure. This mode of failure is commonly called hydrogen embrittlement, a generic term for several different phenomena caused by absorption of hydrogen by metals. In order to avoid this problem the membrane must either be composed of a

material which does not form a hydride or the membrane must be operated in a temperature/pressure regime where hydride formation is suppressed. Some information about this operation regime can be deduced from Figure 2.2. Each of the curves in Figure 2.2 exhibit a decreasing hydrogen concentration as the temperature is increased. Several of the curves exhibit an abrupt drop in hydrogen concentration at a specific temperature: Ti ~650° C, Th ~950° C and Ce ~1200° C. This abrupt decrease in hydrogen concentration indicates that above this temperature the hydride is unstable and this temperature is therefore called the hydride decomposition temperature. The decomposition temperature is pressure dependent: the lower the hydrogen pressure the lower the decomposition temperature. Theoretically a membrane can be operated above the hydride decomposition temperature without suffering from hydrogen embrittlement but extreme caution must be exercised to ensure that the entire membrane is always maintained above the decomposition temperature for any pressure the membrane may encounter. Figure 2.2 shows that at a gas-phase hydrogen pressure of 1 atmosphere an operation temperature in excess of 1000° C is necessary to avoid hydride formation in Th, Ce, and Zr while a temperature in excess of 700° C is necessary for Ti. As in these metals, the high temperatures necessary to avoid hydride formation in most transition metals makes their use as hydrogen separation media impractical. The Pd hydride formation is evident as the temperature drops below ~150° C while Ta and Va transition more gradually between 200° C and 600° C. Due to the relatively low hydride decomposition temperature for these materials they remain possible options for hydrogen membranes with the caveat that they must be operated above this transition temperature.

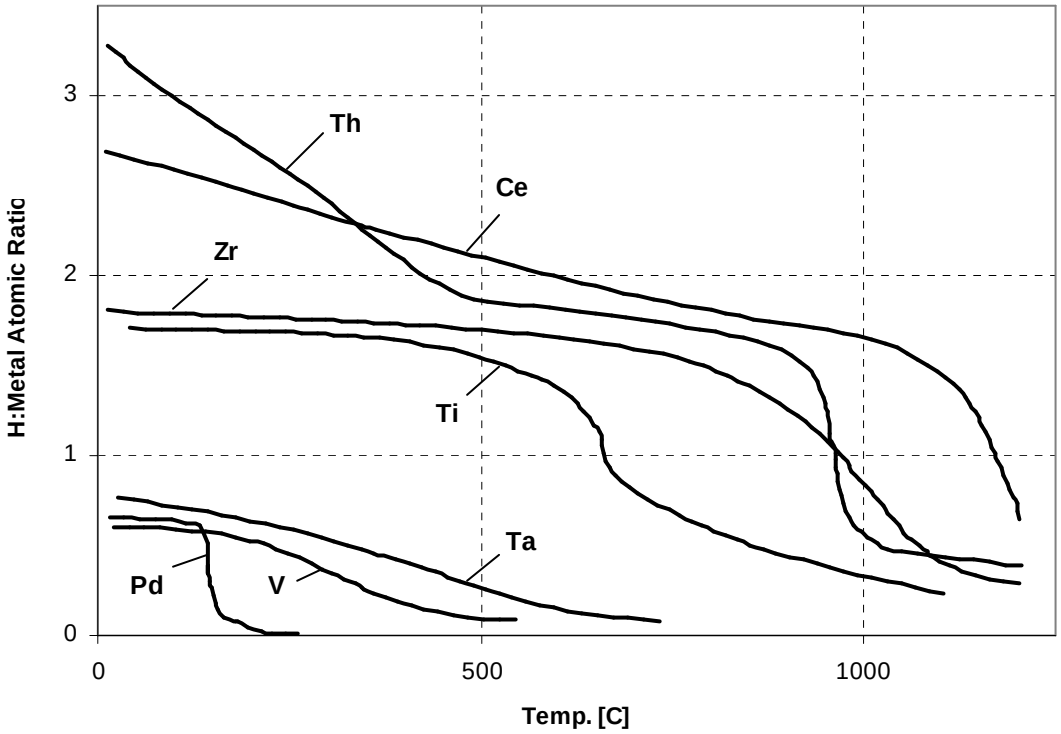

Figure 2.2: Comparison of hydrogen solubility in several transition elements at a gas-phase hydrogen pressure of 1 atm. Sieverts (1929) and Smith (1948) [76-78].

With the exception of Pd, the metals of group VIII in the periodic table do not form hydrides at the elevated temperatures (above ambient) and moderate pressures (up to tens of atmospheres) encountered during typical membrane purification. The solubility of hydrogen in several of these elements is compared in Figure 2.3. As in Figure 2.2, the sharp solubility increase in Pd at lower temperatures is indication of hydride formation and therefore the membrane cannot be operated in this regime. However, even at higher temperatures where hydride formation is suppressed, Pd has larger hydrogen solubility than these materials by a factor of 10-1000. This magnitude of potential performance enhancement over the non-hydride forming elements is sufficient motivation to pursue Pd as a hydrogen separation material despite the possibility of embrittlement and failure at low temperature due to hydride formation.

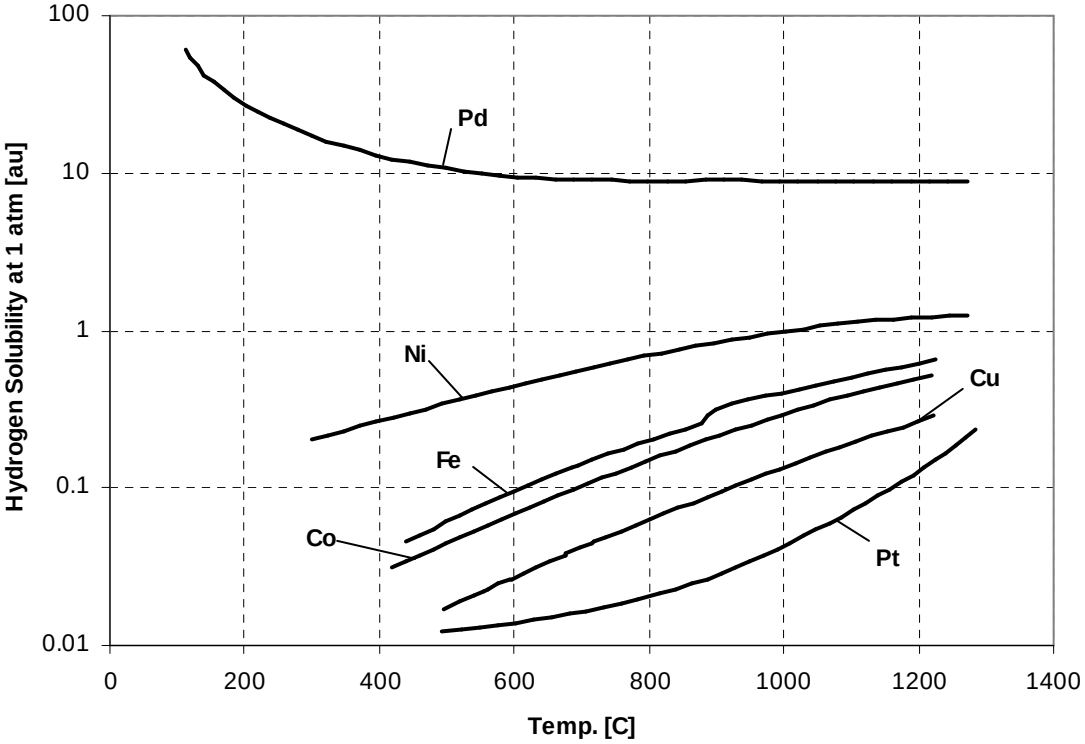

Figure 2.3: Comparison of hydrogen solubility in several group VIII metals at a gas-phase hydrogen pressure of 1 atm. Data from Sieverts (1914) as compiled by Borelius (1927) [71, 72, 79].

2.4 Diffusion of Hydrogen in Metals

Permeability of a material by a given gas species is defined as the product of the gas solubility and diffusion coefficient. It is therefore desirable to have a large diffusion coefficient as well as high solubility to maximize permeability. The diffusion coefficient of atomic hydrogen in several metals is presented in Figure 2.4. The general trend is an exponentially increasing diffusion coefficient with increasing temperature, reflecting the activated nature of the diffusion process. Diffusion is well represented by an exponential equation such as Eq. (2.10) with a pre-exponential factor D_o and activation energy E_{diff}.

$$D = D_o \exp\left(\frac{-E_{diff}}{\Re T}\right) \tag{2.10}$$

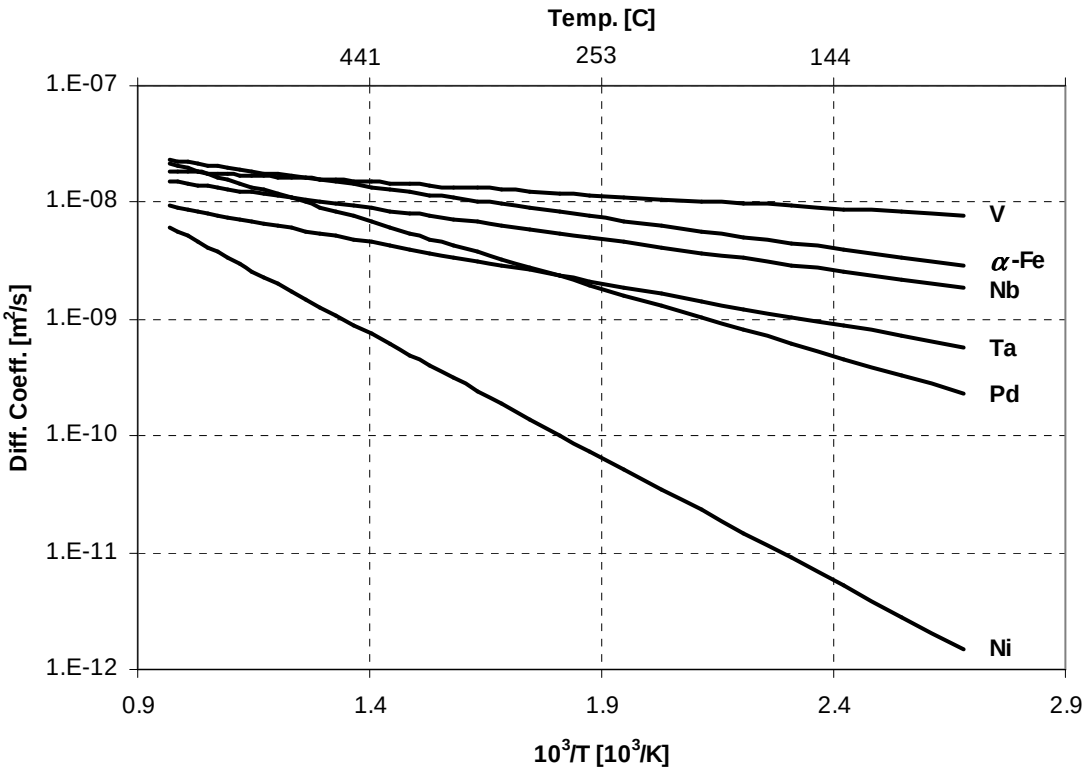

Figure 2.4: Diffusion coefficient of hydrogen in several transition metals. Data compiled in Hydrogen in Metals I (1978) [64].

For Pd, the magnitude of the diffusion coefficient varies between roughly 10^{-10}-10^{-8} m^2/s. As a comparison, the liquid diffusion coefficient of methanol dissolved as a dilute methanol-water mixture is ~10^{-9} m^2/s at 25 ^oC: this is a good approximation of most diffusion in liquids. On the other hand the self-diffusion of Pd atoms is ~10^{-30} m^2/s at 300 ^oC [80] and a general observation is that diffusion of substitutional impurities lies within plus or minus a factor of 100 of self-diffusion in a metal [81]. Being extremely small in both mass and size, the diffusion of hydrogen atoms in metals drastically exceeds nearly all other solid solution diffusion. The diffusion coefficient is more closely matched by diffusion in liquids, and even exceeds these values at elevated temperatures. The anomalously high mobility of hydrogen in metals is one of the primary reasons these materials make attractive separation membranes.

There is also a noticeable variation in the slope of the diffusion curves between the first four elements (V, α-Fe, Nb, and Ta) and the last two (Pd and Ni). This slope is proportional to the activation energy of the diffusion process and this variation is attributed to the difference in atomic structure between the two groups. All of the metals in the first group with a smaller slope than Pd are BCC metals as opposed to the FCC structure of Pd and Ni. The smaller activation energy for diffusion in BCC metals is due to the smaller atomic packing factor of 0.68 in BCC materials versus 0.74 in FCC materials. The less tightly packed BCC structure has larger gaps for hydrogen to penetrate in the diffusion process resulting in lower activation energy.

2.5 Permeability of Hydrogen through Metals

The last two sections have dealt with the specifics of the two components of permeability, namely solubility and diffusion. The aim of this section is to combine the results from those sections and present permeability information for a variety of pure metals. From this data an accurate comparison of the ideal performance of several contending membrane materials can be made.

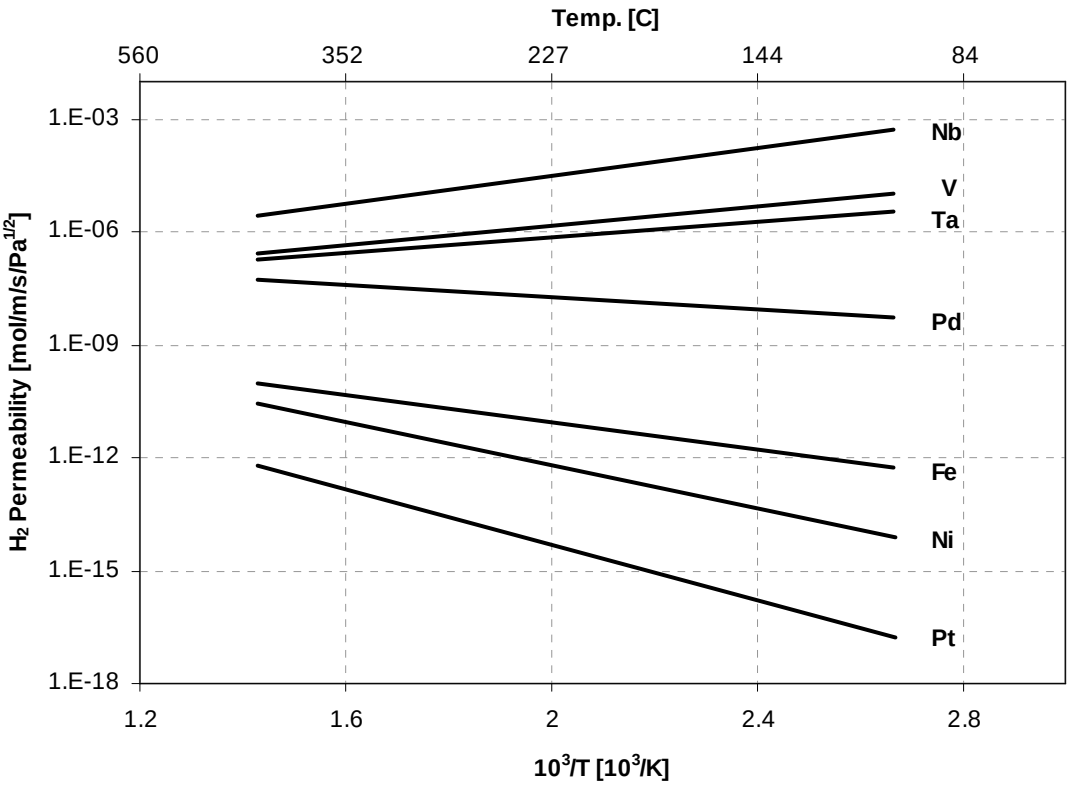

Figure 2.5: Hydrogen permeabilities of selected pure metals, extrapolated from ideal solution behavior (Sieverts' Law) [28, 38, 82].

The permeabilities of several metals to hydrogen are presented in Figure 2.5. These values are not measured across the entire temperature range but instead are extrapolated from the temperature dependence of the diffusion coefficient and solubility of each material from measurements made in a region where Sieverts' Law is obeyed (hydrogen behaves as an ideal solution in the metal) [83]. It is observed that in going from the material with the lowest permeability, Pt, to the material with the highest permeability, Nb, there is a transition in activation energy, being proportional to the negative of the slope of each curve, from positive to negative values. Referring back to Figure 2.4, the diffusion coefficient of each of these materials has a negative slope, which equates to positive activation energy. Therefore, this shift in the temperature dependence of the permeability for some of these materials indicates that the permeability behavior is

largely controlled by the hydrogen solubility. The temperature dependence of Sieverts' Law is given by Eq. (2.11) where $\Delta H°$ and $\Delta S°$ are the molar enthalpy (heat) of solution and standard molar entropy of solution, respectively, both in the limit of infinite dilution.

$$\ln K_s = -\frac{\Delta H^o}{\Re T} + \frac{\Delta S^o}{\Re} \tag{2.11}$$

$$\Phi = D_o \exp\left(\frac{\Delta S^o}{\Re}\right) \cdot \exp\left(\frac{-(E_{diff} + \Delta H^o)}{\Re T}\right) \tag{2.12}$$

Since the permeability is the product of diffusion coefficient and solubility, the apparent activation energy will be the sum of the heat of solution and activation energy of diffusion as shown in Eq. (2.12). For strong exothermic absorbers of hydrogen (Ta, V, Nb) the large negative heat of absorption outweighs the activation energy for diffusion resulting in a negative activation energy for permeation (decreasing values with increasing temperature). For moderately exothermic and endothermic absorbers, the diffusion term dominates and the apparent activation energy for permeation remains positive.

Comparing the overall magnitudes of permeability in Figure 2.5, it is observed that the Group VB metals Ta, Nb, and V substantially outperform Pd over the entire temperature range. This observation, coupled with the favorable difference in cost and relative abundance between these materials and Pd make them appear to be ideal hydrogen separation materials. Unfortunately, unfavorable surface reactions make these materials uncompetitive with Pd-based materials as discussed in the following section.

2.6 Surface Interactions of Hydrogen with Metals

Up to this point it has been assumed that diffusion through the bulk material is much slower than any processes which occur on the surface. This assumption has allowed us to utilize easily measured bulk and thermodynamic properties to predict hydrogen permeability for comparison between different materials. It has also been stated that hydrogen adsorption/absorption is a dissociative process. From a solubility and diffusion standpoint this dissociation is ideal as the resulting species of relevance is now the miniscule hydrogen atom which has little difficulty fitting within, and moving between, the interstices of the metal lattice. However, the necessity of the dissociation process has important ramifications for the interaction of molecular hydrogen with metal surfaces.

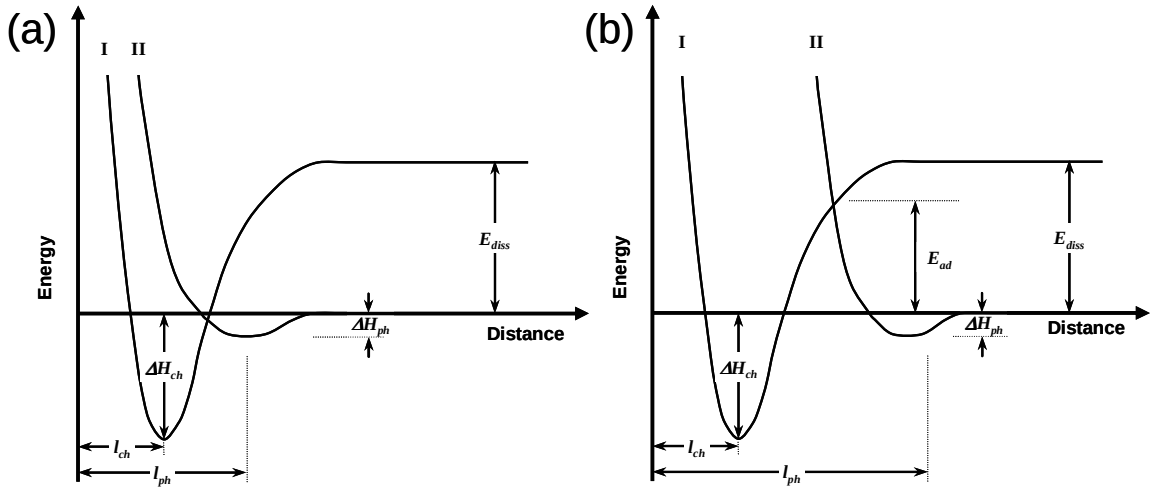

Figure 2.6: One dimensional potential energy diagram for a hydrogen atom (I) and a hydrogen molecule (II) approaching a metal surface. In (a) intimate contact with the surface is attained while in (b) this contact is impeded.

The dissociation energy for molecular hydrogen is 432 kJ/mole [67] as compared to the activation energy for hydrogen diffusion in Pd which is roughly 22 kJ/mole. The magnitude of energy required to dissociate hydrogen suggests that the likelihood of encountering atomic hydrogen in the gas phase at ordinary temperatures is vanishingly

small, as is indeed the case, and that pre-dissociation of the hydrogen molecules prior to reaching the metal surface is not an energetically favorable path. In 1932, Lennard-Jones proposed a simple one dimensional potential energy model to explain the seemingly anomalous result that dissociative adsorption of hydrogen onto clean transition metal surfaces is not an activated process [84]. This model is reproduced in Figure 2.6(a). The curve labeled **II** represents the potential energy of molecular hydrogen as a function of distance from the metal surface. The zero-energy reference point is taken as the energy of the molecule at infinite distance from the surface and therefore curve **II** falls directly on the x-axis at large distances. Following this curve toward the metal surface (decreasing x values) shows that close to the surface there is a small potential well representing physical adsorption, or physisorption, of the molecule to the surface. Physisorption is caused by van der Waals forces between the molecule and surface and is characterized by a low heat of adsorption (ΔH_{ph}), as indicated by the shallowness of the potential well. For molecular hydrogen, the equilibrium distance for this interaction (l_{ph}) is 2 to 3Å and the heat of adsorption is less than 8 kJ/mole [68]. The curve labeled **I** represents chemical adsorption, or chemisorption, of atomic hydrogen onto the surface. Chemisorption is defined as the binding of molecules or atoms to the surface through the exchange or sharing of electrons and is therefore chemical in nature. The heat of chemisorption (ΔH_{ch}) is much larger than physisorption and can range from 25-50 kJ/mole for hydrogen on transition metals and the distance of the hydrogen atom from the surface (l_{ch}) corresponds to that of a chemical bond – between 0.5 and 1.0 Å.

A molecule will approach the surface along curve **II** and initially enter the physisorption well. If the molecule has sufficient energy it can climb the back of the

potential well getting closer to the metal surface and arrive at the intersection of curves **I** and **II**. At this distance the valence electrons of the molecule can interact with the conduction electrons in the metal and allow dissociation of the hydrogen molecule by forming a more energetically favorable atom/metal bond rather than overcoming the energy stored within the H-H bond. The result as shown in Figure 2.6(a) is non-activated, dissociative adsorption which has been shown to be the situation for hydrogen adsorption on nearly all *clean* transition metal surfaces [85].

Figure 2.6(b) illustrates the effects of surface contamination on the adsorption process. Curves **I** and **II** are both the same as in Figure 2.6(a) with the slight change that curve **II**, physisorption, has been shifted slightly to the right, representing the presence of some barrier between the hydrogen molecule and the metal surface. This barrier could be anything from an already adsorbed atom (O, N, C, H) to a stable chemical barrier such as a surface oxide. The result is that although the molecule can be physisorbed onto the surface of the contaminant, the physisorption process does not bring the molecule sufficiently close to the metal surface to allow electronic interaction. Now there is a substantial energy barrier (E_{ad}) which must be overcome for the molecule to dissociate and chemisorb onto the surface.

This process represents a significant problem for refractory metals (Group VB) and iron due to their tendency to form a stable oxide layer [83, 86, 87]. Unfortunately, the tendency for these materials to oxidize, combined with the necessity for high temperature operation to avoid hydride formation in the Group VB metals, makes their use as hydrogen separation media impractical. Due to the favorable permeability of these materials over Pd-based materials, much effort has been expended in an attempt to

overcome this problem. Typically the surface is coated with a thin layer of Pd to protect from oxidation and catalyze the surface hydrogen dissociation. Again, the high temperature necessary to avoid hydride formation interferes as inter-diffusion of the metal species occurs and, over time, the surface loses reactivity [83, 87-92].

2.7 Hydrogen Selectivity of Metal Membranes

It was stated in Chapter 1 that one of the major advantages of metal membranes is their extremely high selectivity for hydrogen over all other species. This is particularly relevant in the context of a hydrogen economy where, presumably, the hydrogen is utilized through a polymer electrolyte membrane (PEM) fuel cell for maximum efficiency. The low-temperature PEM fuel cell electrodes are plagued by their vulnerability to fouling from gas contamination and therefore require extremely high purity hydrogen for extended operation [93].

Figure 2.7 contains diffusion data for atomic carbon, oxygen and nitrogen in both niobium and palladium. The hydrogen diffusion coefficient is also included for reference. At low temperatures the hydrogen diffusion coefficient exceeds the others by 10^{12} while at elevated temperatures it is still at least a factor of 1000 higher. Phenomenologically, this difference is due to the much smaller activation energy for hydrogen diffusion: 22 kJ/mole for hydrogen and 98-117 kJ/mole for the other species. Figure 2.8 presents solubility data for carbon, oxygen and hydrogen in Pd. Again, the values for hydrogen drastically exceed those for the other species, especially at lower temperatures. The solubility values converge at high temperatures due to the fact that hydrogen absorption is exothermic, and therefore favored at lower temperatures, while absorption of carbon and oxygen are endothermic and favored at high temperature.

Combining the information in these figures provides an estimate of the selectivity of metal membranes to hydrogen over other gas species. At low temperatures the selectivity should be greater than 10^{20} while at high temperatures the selectivity may be on the order of 10^4 or more. These numbers also only reflect the selectivity to the atomic species with no reference to how rapidly the surface reactions take place. While transition metals easily allow dissociation/recombination of hydrogen it is unclear how, for example, carbon monoxide, would dissociate onto the surface, diffuse through the membrane, and recombine on the other side. It is likely that these surface processes provide further hindrance to the permeation of other gas species and therefore the selectivity can exceed the values mentioned above.

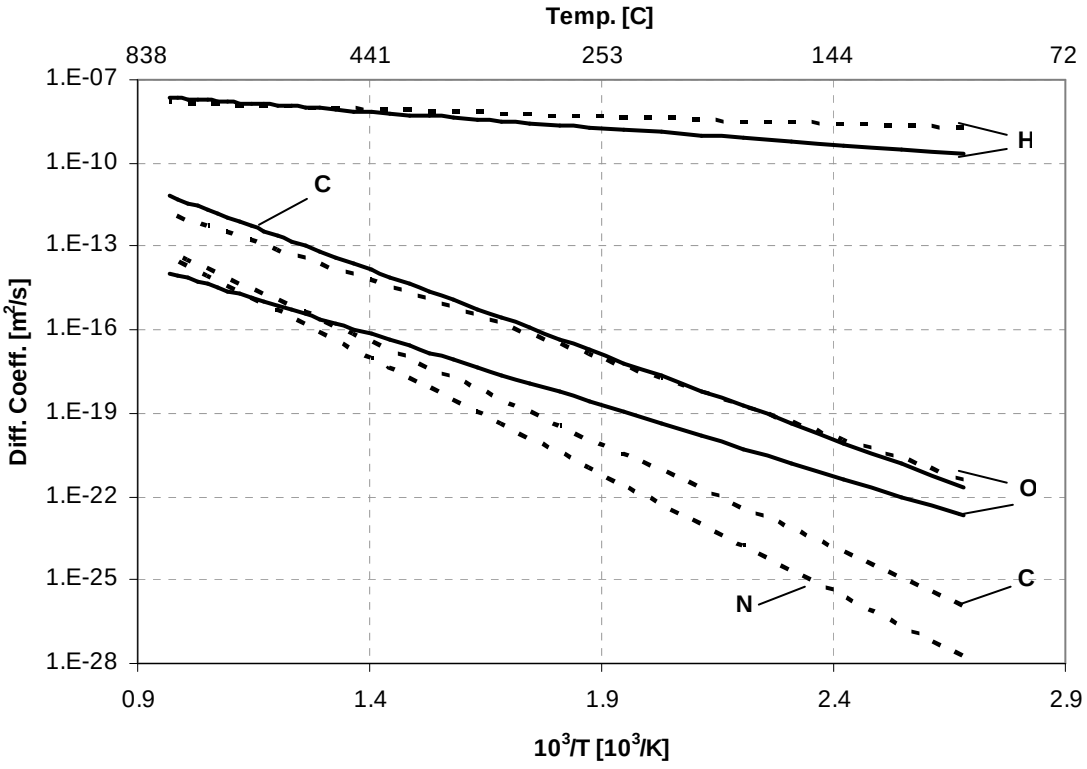

Figure 2.7: Diffusion coefficients of other interstitial species in metals as compared to hydrogen. Dotted curves are diffusion in Nb, solid curves are diffusion in Pd [64, 81, 94-96].

For all practical purposes, the selectivity of metal membranes can be considered infinite. The upper limit on hydrogen purity achieved by permeation through metallic membranes is dictated either by packaging limitations or by the extent to which a thin membrane can be fabricated without through-thickness defects such as pin-holes or cracks. These defects can be particularly problematic for thin metal films.

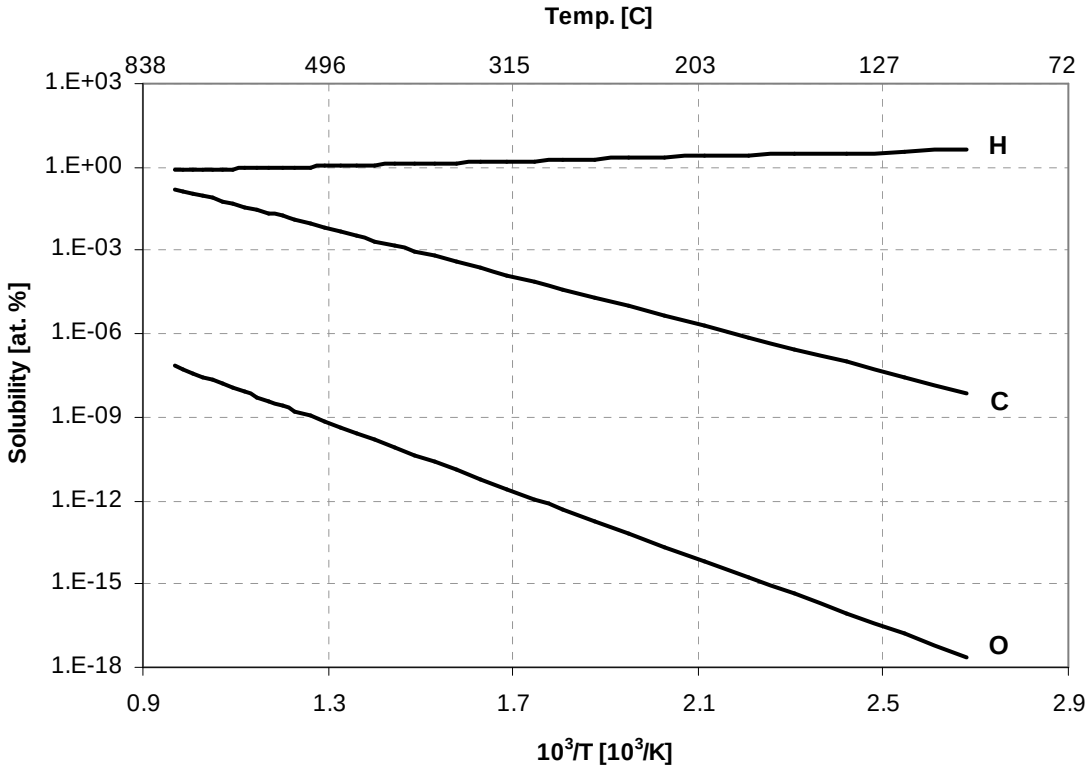

Figure 2.8: Solubility of hydrogen, carbon and oxygen in Pd. C and O values are terminal solubilities, H is calculated for a gas pressure of 1atm [37, 94, 95].

2.8 Palladium-based Membranes

Based on the information presented thus far, it is reasonable to say that Pd is an ideal material for hydrogen purification membranes based on surface reactivity, solubility and diffusion. The major performance issue with Pd membranes is the hydrogen

embrittlement problem which plagues Pd at temperatures below 300 °C. It was discovered in 1960 that alloying palladium with 25% silver ameliorated the embrittlement issue which led to the commercialization of Pd-alloy membrane hydrogen purification systems. In order to understand the hydrogen permeation properties of Pd-alloys at low temperatures it is necessary to understand the physical mechanism responsible for hydrogen embrittlement. This leads directly to an understanding of the effects of alloying on embrittlement and why Pd-Ag is an excellent material for hydrogen separation.

2.8.1 Pd:H Non-Ideal Solution Behavior

Soon after the discovery of H_2 absorption by Pd, the work was naturally extended to quantify the amount of H_2 absorbed when a sample of the metal was allowed to equilibrate with the gas at a given temperature and pressure. By the 1930's, a fairly complete and reproducible set of thermodynamic data relating the hydrogen pressure, temperature, and hydrogen content in the metal had been established [97, 98]. A representative pressure-composition diagram from data taken by Frieske and Wicke is shown in Figure 2.9 [99]. The lines are isotherms connecting data points taken at common temperatures. As this information was gathered it became obvious that Sieverts' Law was not adequate to explain the hydrogen absorption behavior. Since Sieverts' Law is based on the assumption of ideal solution behavior, it was recognized that deviation from this behavior must involve some form of interaction between the absorbed hydrogen.

The data in Figure 2.9 can be broken down into three separate regions as defined by the dome in the figure marked by a dotted line. The first region, labeled α, is the

region where Sieverts' law is valid and the hydrogen concentration is proportional to the hydrogen pressure to the one-half power. As expected this occurs when the hydrogen content is very low and there is not much interaction between the absorbed hydrogen.

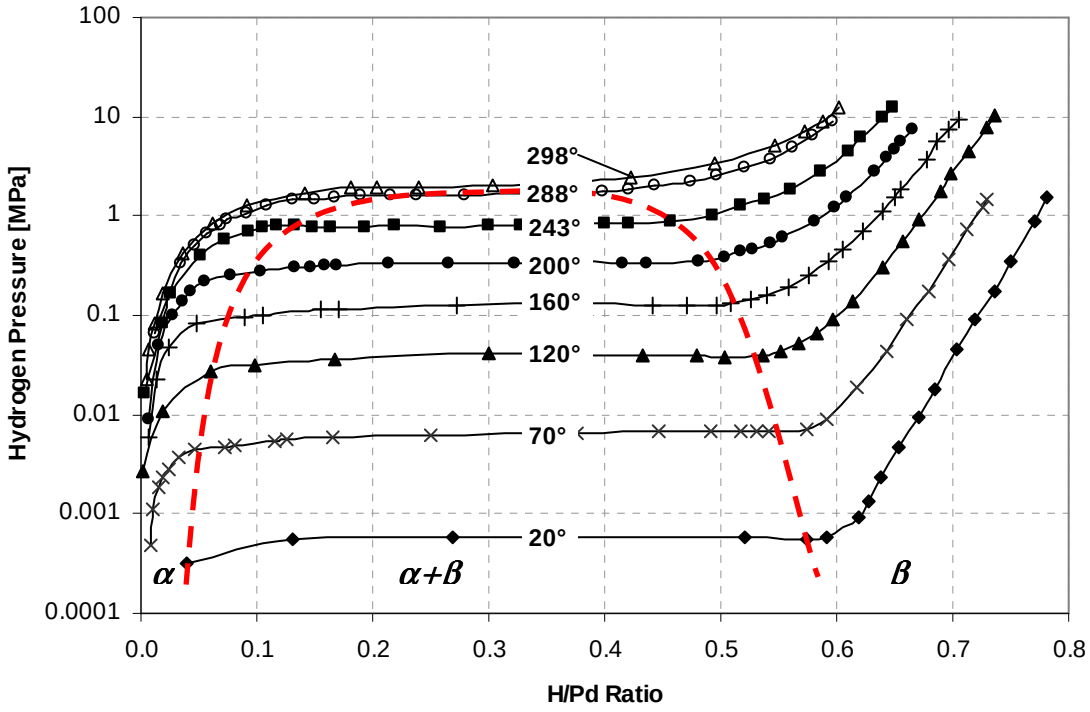

Figure 2.9: Pressure-composition data for the palladium hydrogen system [99].

The second region, labeled α+β, is characterized by a plateau in each isotherm. Across this region the hydrogen concentration increases dramatically with virtually no increase in the hydrogen pressure. Once these plateaus reach the right edge of the dome, there is once again a sharp increase in the hydrogen pressure required to further increase the concentration in the metal. This portion is labeled the β region.

The loss of one degree of freedom of the thermodynamic variables in the α+β region is indicative of the appearance of an additional phase. According to the Gibbs' phase rule, F = C + 2 – Π, the number of degrees of freedom (F) is related to the number

of components (C) and the number of phases present (Π). For the entire diagram there are two components, hydrogen and palladium. In the α region there are two phases, the gaseous hydrogen and the α-phase Pd hydride, and thus two degrees of freedom. Having two degrees of freedom indicates that two thermodynamic variables, such as temperature and pressure, can be changed independently without leaving the two-phase region. In the $\alpha+\beta$ region the fact that pressure and temperature can no longer be varied independently indicates that a degree of freedom has been lost and thus an additional phase has appeared.

With this information the phase diagram may be interpreted in the following way. Following an isotherm from left to right, at low pressure hydrogen is absorbed and forms an ideal solution in the metal. As pressure is increased, hydrogen content increases monotonically and is uniform throughout the sample. At some point when pressure is increased, rather than uniformly increasing the hydrogen content of the entire sample, small regions of high hydrogen content nucleate within the sample. This is the nucleation of the β-phase Pd hydride within the α-phase. From this point, as more hydrogen is absorbed the hydrogen content of both phases remains constant but the average content of the sample increases as the volume percentage of the β-phase increases relative to the α-phase. This process continues until the entire sample has been converted to the β-phase at the right edge of the dome. From this point the hydrogen content once again increases monotonically as the hydrogen pressure is increased. Therefore, the left edge of the dome follows the locus of points that define the maximum hydrogen content for the α-phase while the right edge of the dome defines the minimum hydrogen content for the β-phase. These lines are also known as the solvus lines for the α and β phases,

respectively. As temperature is increased the hydrogen mobility in the sample increases and the random thermal motion of hydrogen makes agglomeration into local hydrogen-rich regions less favorable. This corresponds to an increase in the stability of the α-phase, increasing its maximum hydrogen content, and a simultaneous decrease in the stability of the β-phase and a reduction of its hydrogen content. The result is that as temperature is increased the difference in hydrogen content of the two phases is reduced, shrinking the miscibility gap. Above the critical temperature, ~300 °C for Pd, the two phases are no longer distinguishable and there is a smooth transition from low hydrogen content to high hydrogen content as pressure is increased.

As mentioned in Section 2.3, the formation of the high-hydrogen-content β-phase results in an increase in the lattice parameter from 3.89Å to 4.03Å with a corresponding11% volumetric increase. Nucleation and growth of these regions as Pd is cycled across the miscibility gap produces significant strain within a sample resulting in plastic deformation. This strain and resulting plastic deformation is the source of the previously mentioned hydrogen embrittlement and invariably results in failure if Pd is used as a hydrogen separation membrane. This limits the permissible operation regime for pure Pd to values above the critical temperature.

Suspecting that the origin of the non-ideal behavior was the interaction between the absorbed hydrogen, Lacher was able to utilize a statistical thermodynamics approach to reproduce the measured isotherms [100, 101]. Lacher started with Eq. (2.13) as the functional form of the chemical potential for the absorbed hydrogen.

$$\mu_{H}^{s} = \mu_{H}^{0} + \Re T \ln\left(\frac{\chi}{1-\chi}\right) + \Delta\mu_{H} \tag{2.13}$$

In Eq. (2.13) the first term, μ_H^0, is the standard potential. The second term represents the statistical distribution of the absorbed hydrogen among a discrete number of interstitial sites. The symbol χ is the atomic ratio of hydrogen to palladium (H/Pd) and therefore this term causes a dramatic increase in the chemical potential as available lattice sites are filled and χ approaches unity. The last term is the excess potential added by Lacher to account for an attractive pairwise H-H interaction. The magnitude of the excess potential is proportional to the value of χ with an increasing negative contribution to the chemical potential as the amount of absorbed hydrogen increases. Using this model Lacher was able to reproduce the isotherms through the two-phase region, however, the sharp increase in the chemical potential of absorbed hydrogen above an H/Pd ratio of ~0.6 was still problematic. Since there is one octahedral interstitial site per host atom in the FCC structure this increase in chemical potential should occur as the lattice approaches saturation, i.e. when H/Pd approaches unity. Lacher was forced to assume that there were two types of interstitial sites: one that was accessible to hydrogen and represented 60% of the total sites and the other that was inaccessible to hydrogen and accounted for the remaining 40% of octahedral sites. A few years later, Wagner assumed equivalence between all octahedral sites and correctly attributed the increase in chemical potential of the absorbed hydrogen to an electronic contribution [102].

While these early models could capture the behavior quite accurately, it wasn't until much later that the nature of the hydrogen-metal interactions was fully understood. In 1972 Alefeld recognized that the average elastic interaction between the absorbed hydrogen and the metal lattice should contribute to the enthalpy of solution [103]. It was shown by Eshelby that the presence of point defects in a bounded elastic medium should

induce an average volumetric increase of the lattice in order to keep the external surface free from stress [104]. Thus, interstitial hydrogen atoms produce a lattice dilation causing a reduction in the enthalpy of solution which is proportional to the local hydrogen concentration. This elastic effect, also known as the mean-field theory, causes a positive feedback at a certain critical value of hydrogen concentration. The enthalpy of solution is lower in a region of high hydrogen concentration causing diffusion of hydrogen to that region (against the concentration gradient) and resulting in further decrease of the enthalpy of solution as the lattice expands. The result is hydrogen agglomeration in certain regions of the lattice: β-phase hydride formation. The extent to which the positive feedback proceeds depends upon the other contribution the chemical potential, namely the electronic contribution. As hydrogen is absorbed, its electrons join the existing electron structure and cause an increase in the Fermi level of the system. In Pd, the electrons initially go into the 4*d* band which has a high density of states so the electronic contribution to the excess potential is very small. Above χ~0.6, only the low-density of states in 5*s* band are available causing a more pronounced increase in the electronic contribution which dominates the total chemical potential of the absorbed hydrogen [67, 105-107]. The chemical potential of the absorbed hydrogen can now be written with the excess potential divided into the elastic ($\Delta\mu_{elast.}$) and electronic contribution ($\Delta\mu_{elect.}$):

$$\mu_H^s = \mu_H^0 + \Re T \ln\left(\frac{\chi}{1-\chi}\right) + \Delta\mu_{elast.} + \Delta\mu_{elect.} \qquad (2.14)$$

This knowledge of the behavior of hydrogen solution in Pd explains the problem of hydrogen embrittlement and suggests a method for improving mechanical stability by alloying Pd with other metals.

2.8.2 Effects of Alloying Palladium on Hydrogen Solubility

Based on the previous observation that the lattice expansion caused by hydrogen absorption leads to a decrease in the enthalpy of solution, it might be expected that this effect could also be achieved by alloying Pd with other metals which increase the lattice parameter. It has been shown that the difference in lattice parameter between the alloy and pure palladium is proportional to the negative change in enthalpy of solution at infinite dilution, $\Delta H°$ [108]. In other words, if alloying increases the lattice parameter then the enthalpy of solution decreases while if the alloy has a smaller lattice parameter the enthalpy of solution increases. Simultaneously, there is a decrease in the entropy of solution at infinite dilution, $\Delta S°$, with increasing metal solute concentration [67]. This suggests that the number of available sites for absorption decreases as alloy concentration increases, probably due to repulsive interactions between the hydrogen and metal solute atoms. This trade-off with increasing alloy concentration is expected, otherwise pure metals with a larger lattice parameter than Pd would have a higher solubility, which is not the case. A repulsive interaction between the hydrogen and alloying atoms also explains the slight decrease in diffusion coefficient observed with increasing alloy composition [37]. Referring back to the two-phase dome in Figure 2.9, the lattice expansion effect can be further clarified. For pure Pd, as the concentration of hydrogen increases it reaches a critical value where the dilation caused by absorption initiates a positive feedback response leading to nucleation of the β-phase. For an alloy with an already expanded

lattice the amount of hydrogen which will be absorbed for a given pressure is larger (due to lowering the enthalpy of solution) and the dilation caused by hydrogen absorption is reduced. Since the difference in enthalpy between the normal lattice and the expanded β-phase lattice is reduced, less thermal energy is required to destabilize the transition, thus the critical temperature is reduced. From the pressure-composition diagram, the end result is a downward vertical shift of the two-phase dome reducing the critical temperature.

In addition to changing the lattice parameter, exchanging Pd atoms for alloy atoms that have a different number of valence electrons will have an effect on the electronic structure of the metal. For Pd-alloys a simple band filling model is adequate and the effect is straightforward: if the alloy element is an electron donor it will partially fill the 4*d* band and reduce the hydrogen solubility of the β-phase. The right edge of the two-phase dome will be shifted towards lower hydrogen concentration reducing the size of the miscibility gap.

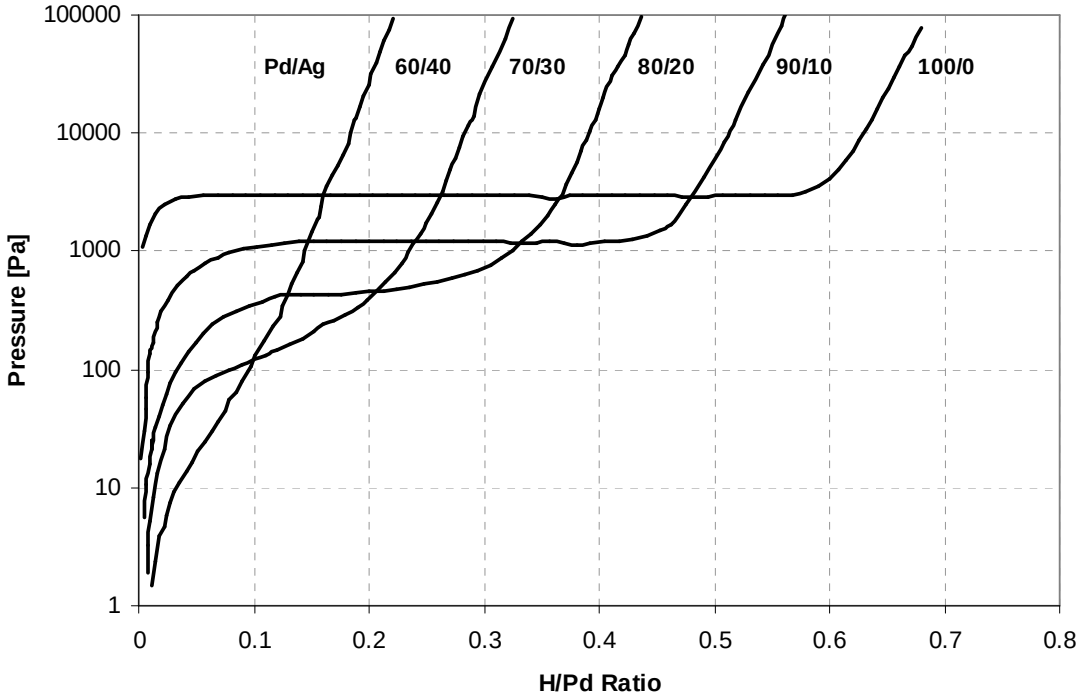

Figure 2.10: Hydrogen pressure-composition isotherms in Pd-Ag alloys of increasing silver content at 50 °C [67, 107].

Both of these effects can be seen in Figure 2.10 where an isotherm at 50 °C has been plotted for several palladium-silver alloy compositions. Silver is a larger atom than Pd and will therefore expand the lattice. Silver also has an additional valence electron and should therefore partially fill the 4*d* band. Initially, as silver is added, the width of the pressure plateau is reduced, indicating increased solubility in the α-phase and reduced solubility in the β-phase. The plateau disappears altogether at 20% Ag. This does not mean that the two-phase region is gone; the critical temperature has just decreased to such an extent that now the 50 °C isotherm is supercritical. After leveling off, each isotherm exhibits the sharp increase in pressure required to increase the hydrogen content that is associated with the rise in the Fermi level of the 5*s* band. As predicted, the

concentration at which this transition occurs is reduced as Ag content is increased and space in the 4*d* band becomes limited.

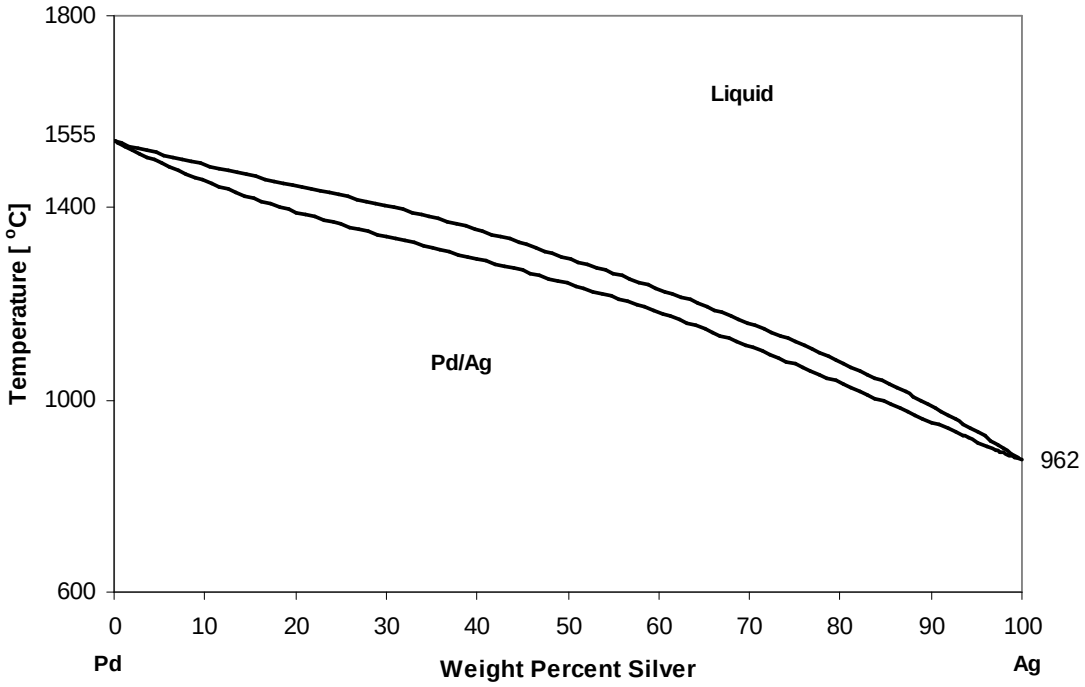

Figure 2.11: Palladium-Silver phase diagram [109].

In addition to the impact on hydrogen solubility, the possibility of phase separation when alloying Pd must be considered. If the alloying metal is not completely miscible with Pd there is the possibility of phase change in the metal at certain compositions or in certain temperature ranges. Needless to say, this substantially complicates the interpretation of hydrogen permeation behavior and it is likely that any phase change will cause unacceptable structural instability for membrane use. From this standpoint, silver is an ideal alloying component for Pd membranes. As shown in the Pd-Ag phase diagram in Figure 2.11, these two materials form a perfectly miscible, ideal solution. The discovery by Hunter that a 75-25% Pd-Ag alloy is an excellent hydrogen permeation material is no coincidence. It has since been shown that an alloy with 23%

Ag is precisely the amount necessary to reduce the critical temperature for the two-phase dome down to below atmospheric temperature. As long as the membrane is not cooled below ~25 °C, hydrogen embrittlement will be avoided. In addition to avoiding hydrogen embrittlement, the lattice expansion caused by alloying increases hydrogen solubility in the α-phase and results in an overall permeability enhancement over pure Pd.

Due to the advantages of the 77-23% Pd-Ag system it is the alloy used in the current study. This alloy also has the additional benefit that there have already been numerous investigations into its permeation properties using thick samples for comparison to the current results with extremely thin membranes.

CHAPTER 3
HYDROGEN PERMEATION MODELING

An early attempt to model the hydrogen permeation behavior of hydrogen through metals was the work of Richardson and co-workers in 1904 [110]. Based on extensive experimental work, Richardson developed a semi-empirical equation to predict the hydrogen flux through a metal for a given operating temperature (T), pressure difference (P_H-P_L), and thickness of the sample (t). The result, often referred to as the Richardson equation, is shown in Eq. (3.1).

$$\dot{m}'' = \frac{k \exp(-b/T)(P_H^{0.5} - P_L^{0.5})T^{0.5}}{t} \tag{3.1}$$

While this equation was largely empirical it is remarkably accurate over a wide range of operating conditions and is still used today. Typically, the exponential temperature dependence far outweighs the $T^{0.5}$ term and the remaining equation is exactly Eq. (2.4), a combination of Sieverts' Law and steady-state Fickian diffusion.

By 1935 the gas permeation properties for several gas-metal systems had been experimentally studied and found to largely obey the Richardson equation. It was observed by Smithells and Ransley that when the hydrogen permeation rate was plotted versus the square-root of gas pressure difference, the extrapolated line would always intersect the x-axis at a small positive value as shown schematically in Figure 3.1 [111]. This implied the existence of a threshold pressure difference below which no hydrogen would permeate the metal. Smithells examined the experimental data and concluded that no such pressure existed and reasoned that diffusion can only proceed if hydrogen is first adsorbed onto the metal surface. The expression for the hydrogen flux should therefore

be the product of the Richardson equation and the equilibrium surface coverage, θ_{eq}. This modification, using the Langmuir isotherm for dissociative adsorption, is shown in Eq. (3.2) with k_{ads} and k_{des} the adsorption and desorption rate constants, respectively. As the pressure is reduced towards zero the predicted flux now approaches zero as shown by the dashed curve in Figure 3.1.

$$\dot{m}'' = \frac{k \exp(-b/T)(P_H^{0.5} - P_L^{0.5})}{t} \cdot \theta_{eq}$$
$$\theta_{eq} = \frac{\sqrt{\frac{k_{ads}}{k_{des}}} P^{0.5}}{1 + \sqrt{\frac{k_{ads}}{k_{des}}} P^{0.5}} \tag{3.2}$$

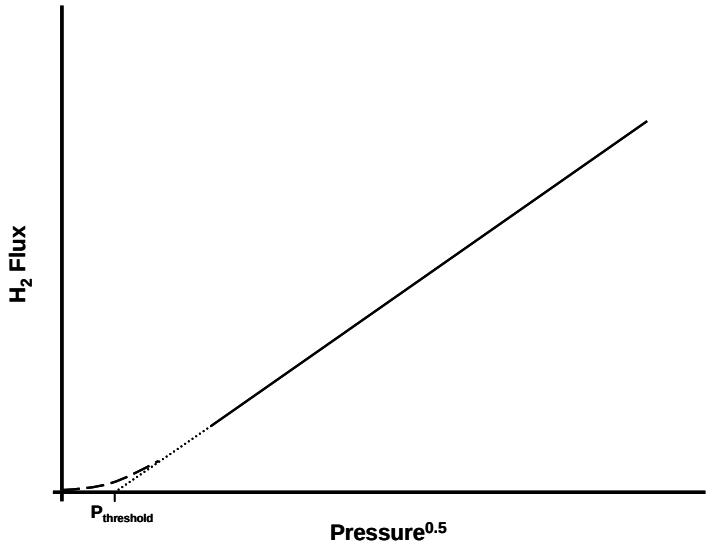

Figure 3.1: Schematic trend in hydrogen flux as a function of the square root of pressure difference. The dotted line extrapolates experimental data to the x-axis according to the Richardson equation and predicts a 'threshold pressure' below which permeation does not occur. The dashed line shows the modification to the model made by Smithells et. al. that predicts no threshold pressure [112].

This combined model represents the first time that surface processes were considered as a controlling influence on the hydrogen permeation rate. The next year, Wang developed a theoretical model considering hydrogen permeation as a sequence of

several steps that must occur in series and this is essentially the model in use today [113]. The following seven steps are considered in the permeation process:

1. Gas-phase transport to the membrane surface
2. Dissociative adsorption onto the surface
3. Transition from a surface site to an interstitial bulk site
4. Diffusion through the bulk lattice
5. Transition from the bulk onto the downstream surface
6. Recombinative desorption from the surface
7. Gas-phase transport away from the membrane surface

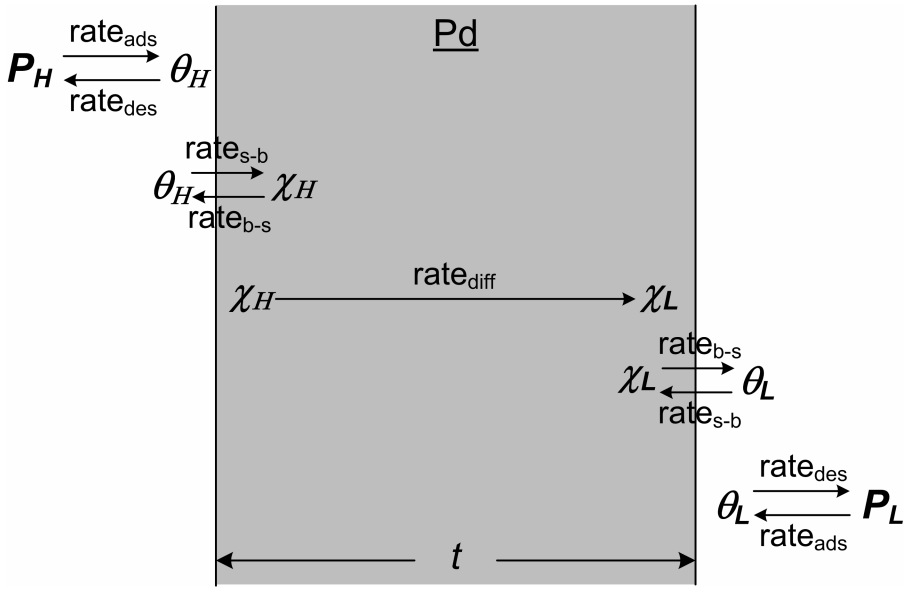

Figure 3.2: Sequential mechanism for hydrogen permeation through a metal membrane. Gas phase transport steps not shown.

Neglecting gas-phase transport, the rate equations can be written as shown in Eq. (3.3).

$$\begin{aligned} rate_{ads} &= k_{ads} P_H (1-\theta_H)^2 \\ rate_{s-b} &= k_{s-b} \theta_H (1-\chi_H) \\ rate_{diff} &= k_{diff} (\chi_H - \chi_L) \\ rate_{b-s} &= k_{b-s} \chi_L (1-\theta_L) \\ rate_{des} &= k_{des} \theta_L^2 \end{aligned} \tag{3.3}$$

As in a typical chemical reaction, the rate of each process can be described by an appropriate rate constant multiplied by the amount of reactant present at a given time. Due to the discrete nature of the available locations for the adsorption, surface-bulk, and bulk-surface processes, each of these rates must also be multiplied by a term to reflect the probability that there will be an available site for the process to occur. For example, the adsorption rate is the product of the rate constant, k_{ads}, the hydrogen gas-phase pressure, P, and the likelihood of encountering two vacant surface sites onto which adsorption can take place. The probability of encountering a single vacant surface site is equivalent to the fraction of available sites ($1-\theta$), and if the coverage is low, the likelihood of finding two vacant sites adjacent to each other is simply the square of this quantity. Similarly, the rate of transport from the surface into the bulk is controlled by both the surface coverage (θ) and the fraction of vacant sub-surface sites ($1-\chi$).

In 1959, Ash and Barrer recognized that the hydrogen flux could be cast as the difference between the forward and reverse rates of any of these processes across the control surface where the process occurs [114]. For example, the net flux can be written as the difference between the adsorption rate onto the upstream surface and the desorption rate from that surface back into the gas phase. The net flux can also be written as the difference between the rate of surface-bulk transition and bulk-surface transition across one membrane surface. At steady-state, the mass flux across each interface must be equal and therefore a system of equations can be constructed to relate the rate equations and the net flux. This system is shown in Eq. (3.4).

$$
\begin{aligned}
\dot{m}'' &= k_{ads} P_H (1-\theta_H)^2 - k_{des}\theta_H^2 \\
\dot{m}'' &= k_{s-b}\theta_H (1-\chi_H) - k_{b-s}\chi_H (1-\theta_H) \\
\dot{m}'' &= k_{diff} (\chi_H - \chi_L) \\
\dot{m}'' &= k_{b-s}\chi_L (1-\theta_L) - k_{s-b}\theta_L (1-\chi_L) \\
\dot{m}'' &= k_{des}\theta_L^2 - k_{ads} P_L (1-\theta_L)^2
\end{aligned}
\tag{3.4}
$$

Assuming the rate constants are known, this system has five equations and five unknowns (θ_H, χ_H, χ_L, θ_L, and $\dot{m}''$) and can be solved to predict the hydrogen flux as a function of the applied pressure difference, temperature and membrane thickness. In the limiting case that the rate of diffusion is much slower than the surface processes, and the sub-surface concentration is much less than one (equivalent to assuming that Sieverts' Law is valid) the system of equations is reduced to the Richardson equation, validating this approach.

The development of this model was a major step forward in understanding the hydrogen permeation process, but quantitative information about the rate constants in the model was still lacking. Over the next several decades this information was gathered and finally compiled in 1996 in a complete model by Ward and Dao [55]. Notably, work on hydrogen adsorption onto Pd was done by Behm and co-workers [115] and Pick and Sonnenberg [116] made a significant contribution to the current understanding by estimating the rate constants based on a 1-D potential energy diagram for hydrogen permeation shown in Figure 3.3. The model which will be described in the following section will be called the Ward and Dao model for the sake of brevity but it should be recognized that their work is a culmination of extensive efforts by many groups. The pieces of the model were developed over many years and the research necessary to make the model useful, i.e. mechanisms of physical interactions of hydrogen with metals, span

that length of time as well. The main contribution of Ward and Dao to the model was to compile the available information and apply the model to a given system, the palladium-hydrogen system. The rate constants are estimated from values available in the literature and where not available, Ward and Dao have made estimates. After compiling this information they have utilized the model to predict membrane behavior under a variety of conditions.

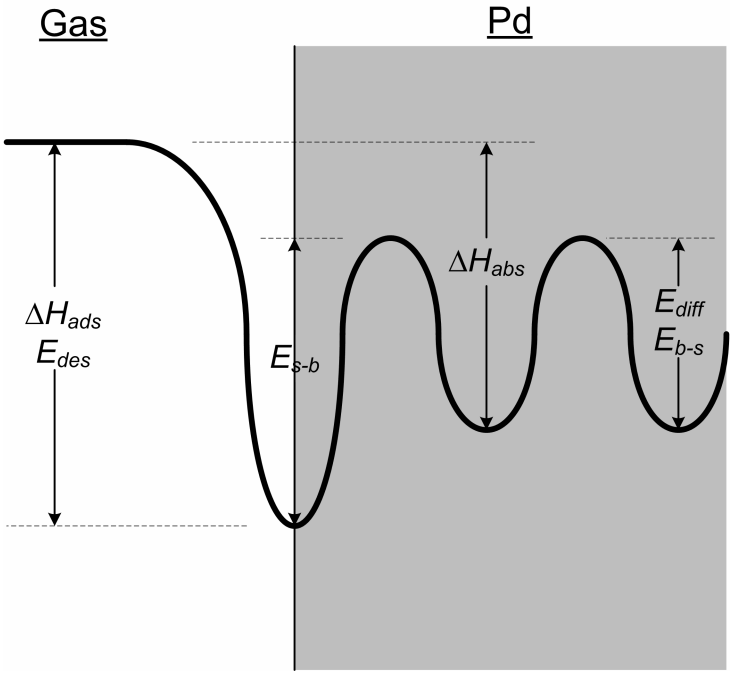

Figure 3.3: One-dimensional potential energy diagram for hydrogen permeation through Pd. ΔH_{abs} and ΔH_{ads} are the enthalpies of solution and adsorption respectively and $E_{s\text{-}b}$, $E_{b\text{-}s}$, E_{des} and E_{diff} are the activation energies for the surface-bulk, bulk-surface, desorption and diffusion processes.

3.1 The Ward and Dao Model

3.1.1 Dissociative Adsorption

The adsorption rate can be interpreted as the product of the molecular bombardment rate onto the metal surface, Γ, and the sticking coefficient, S:

$$rate_{ads} = 2\Gamma \cdot S(\theta) \tag{3.5}$$

The sticking coefficient is simply the likelihood that a given molecule will adhere to the surface. Since the chance of encountering a vacant site for adsorption depends upon the number of vacant sites, the sticking coefficient is a function of surface coverage, $S(\theta)$. In general, adsorption should be considered an activated process but numerous studies have shown that hydrogen adsorption onto a clean Pd surface is a non-activated process and it is considered as such in this model. The molecular bombardment rate is derived from kinetic theory and given by Eq. (3.6). It is a function of the hydrogen pressure in the gas phase (P), the temperature (T), and the molecular mass of the hydrogen molecule (M_{H2}). At low surface coverage the Langmuir expression for the sticking coefficient, Eq. (3.7), can be used.

$$\Gamma = \frac{P}{\left(2\pi \Re T M_{H_2}\right)^{0.5}} \tag{3.6}$$

$$\left(S(\theta)/S_0\right)_{Langmuir} = (1-\theta)^2 \tag{3.7}$$

At higher coverage, interaction between the adsorbed hydrogen atoms may impart structural order on the surface. Using statistical mechanics and invoking the quasi-chemical approximation an expression can be derived to give the fraction of nearest-neighbor occupied site pairs as a function of surface coverage and the interaction energy between the adsorbed hydrogen (w). This expression can then be converted into the fraction of empty nearest neighbor sites (θ_{oo}) which are necessary for dissociative adsorption:

$$\theta_{oo} = 1-\theta-\frac{2\theta(1-\theta)}{\left\{1-4\theta(1-\theta)\left[1-\exp\left(-w/\Re T\right)\right]\right\}^{1/2}+1} \tag{3.8}$$

Surface adsorbate interaction, along with possibility of an adsorption precursor state have been considered by Kisliuk and King and Wells and were applied to the experimental data for H-Pd by Behm et. al. [115, 117-119]. In the precursor state, a physisorbed molecule can execute a finite number of near-surface jumps and possibly locate an available adsorption site. The resulting expression for the sticking coefficient is given by Eq. (3.9).

$$S(\theta)/S_0 = \left[1+\zeta\left(1/\theta_{oo}-1\right)\right]^{-1} \tag{3.9}$$

The constant S_o is the sticking coefficient at zero coverage and is taken to be unity. The parameter ζ is a constant which depends on the probability of adsorption and desorption in empty and occupied sites. In the limit that ζ=1 and $w=0$, Eq. (3.9) reduces to the Langmuir expression in Eq. (3.7).

3.1.2 Surface to Bulk Metal Transition

The rate at which hydrogen transitions from a surface site into a bulk site can be expressed as the product of the concentration of hydrogen on the surface, the probability of successfully overcoming the activation energy barrier to reach a bulk site, and the probability that the bulk site is vacant to permit the transition to occur:

$$rate_{s-b} = N_s\theta\nu_0 \exp\left(-E_{s-b}/\Re T\right)(1-\chi) \tag{3.10}$$

The likelihood of successfully overcoming the energy barrier is represented as an activated process with a pre-exponential factor, ν_o, and a surface-to-bulk activation energy, $E_{s\text{-}b}$. This activation energy is shown in Figure 3.3 and can be calculated from the difference between the enthalpy of adsorption and the enthalpy of solution. The

likelihood of encountering a vacant site is equivalent to the quantity (1-χ), with χ the atomic ratio of hydrogen to Pd in the bulk metal just below the surface. Since there is one octahedral interstitial vacancy per Pd atom, the atomic ratio is also the fraction of the total sites which are occupied by hydrogen. The product of the concentration of surface sites (N_s) and the surface coverage gives the concentration of hydrogen atoms on the surface. The constant N_s is the area concentration (with units of mol/m^2) of interstitial sites, or equivalently Pd atoms, and is calculated from Eq. (3.11).

$$N_s = N_b^{2/3} \Big/ N_{av}^{1/3} \tag{3.11}$$

This concentration is valid for the number of sites in any two-dimensional plane within the metal lattice, whether on the surface or in the bulk. The constant N_b is the interstitial site concentration in the bulk palladium (with units of mol/m^3) and N_{av} is Avogadro's number. The unknown in Eq. (3.10) is the pre-exponential factor and the estimate of this value will be discussed in Section 3.1.6.

3.1.3 Solid-State Atomic Diffusion

Using a simple Fickian diffusion model, the diffusion rate is the product of the diffusion coefficient and the concentration gradient. Under steady-state conditions this can be simplified to Eq. (3.12). The hydrogen concentration near the surface is the product of the concentration of interstitial sites (also the concentration of Pd atoms in the lattice), N_b, and the atomic ratio of hydrogen to palladium. Diffusion is an activated process with the associated pre-exponential factor, D_o, and the activation energy for diffusion, E_{diff}.

$$rate_{diff} = D_0 \exp\left(-E_{diff}/\Re T\right)\frac{N_b(\chi_H - \chi_L)}{t} \tag{3.12}$$

The activation energy and pre-exponential factor for diffusion have been measured by numerous researchers and there is good agreement between studies [64].

3.1.4 Bulk Metal to Surface Transition

Similarly to the surface-to-bulk transition, the bulk-to-surface transition is the product of the area concentration of hydrogen in the bulk near the surface (in units of mol/m^2), the probability that a given atom will overcome the activation energy between the bulk and surface, and the likelihood of encountering a vacant site on the surface. The area concentration of hydrogen in the bulk is calculated from the product $N_s\chi$ and the likelihood of encountering a vacant surface site is (1-θ) resulting in the expression for the bulk-to-surface rate:

$$rate_{b-s} = N_s\chi\beta_0 \exp\left(-E_{b-s}/\Re T\right)(1-\theta) \tag{3.13}$$

It is reasonable to assume that the physical process of jumping from a bulk site to a surface site is similar to a jump from one bulk site to another since the starting point is a bulk site in both cases. Therefore, as can be seen in Figure 3.3, the activation energy for a jump from a bulk site to the surface is the same as the activation energy for diffusion. Also, the attempt frequency (pre-exponential factor) for a bulk-to-surface jump can be estimated from the diffusion pre-exponential factor using solid-state diffusion theory. The diffusion coefficient is a function of the lattice parameter (a), jump frequency (υ_j), and the number of possible jump locations:

$$D = \frac{a^2\upsilon_j}{12} \tag{3.14}$$

For octahedral interstitial sites there are twelve nearest neighbor sites, hence a factor of twelve in Eq. (3.14). Approximately one-third of the successful atomic jumps are into the next lattice plane (with one-third staying in the current plane and one-third going in the reverse direction) therefore the bulk to surface rate can also be described by

$$rate_{b-s} = \frac{1}{3}\upsilon_j N_s \chi \tag{3.15}$$

where the product $N_s\chi$ is the area concentration of hydrogen atoms near the surface. Solving Eq. (3.14) for the jump frequency, substituting into Eq. (3.15), and equating the pre-exponential factors between Eq. (3.13) and Eq. (3.15) leads to the expression in Eq. (3.16) for the bulk-surface pre-exponential factor. The Pd lattice parameter (a) has a value of 3.89Å at room temperature.

$$\beta_0 = \frac{4D_0}{a^2} \tag{3.16}$$

3.1.5 Recombinative Desorption

The desorption rate is the likelihood of overcoming the activation energy for desorption multiplied by the probability of having two adjacent, occupied surface sites from which two atoms can combine and desorb as a hydrogen molecule. At low surface coverage this results in second order kinetics (analogous to using the Langmuir expression as in Eq. (3.7)), represented by Eq. (3.17).

$$rate_{des} = 2k_0 \exp\left(-E_{des}/\Re T\right) N_s \theta^2 \tag{3.17}$$

Once again, a more general expression may be derived from the quasi-chemical approximation for the interactions between adsorbed surface atoms to account for the desorption behavior at high coverage:

$$rate_{des} = 2k_0 \exp\left(-E_{des}/\Re T\right) N_s \theta \cdot F(\theta)$$
$$F(\theta) = \left(1 - \frac{2-2\theta}{\left\{1-4\theta(1-\theta)\left[1-\exp\left(-w/RT\right)\right]\right\}^{0.5}+1}\right) \quad (3.18)$$

In the limit that θ goes to zero or the interaction energy (w) is zero, Eq. (3.18) reduces to Eq. (3.17). The activation energy for desorption is approximately equal to the heat of adsorption and has been measured experimentally [115, 120-122]. The pre-exponential factor can be estimated from thermal desorption data [115].

3.1.6 Estimate of Surface-to-Bulk Pre-exponential Factor

Every constant in the model can be estimated from values found in the literature except the pre-exponential factor for the surface-to-bulk transition. Due to the additional freedom for motion of the surface state, the vibrational frequency of the adsorbed atom cannot be directly linked to an attempt frequency to enter the bulk. To overcome this difficulty, Ward and Dao utilize a thermodynamic reciprocity relationship to estimate the rate of this transition. When the hydrogen in the gas phase and in the bulk are in equilibrium the rates of adsorption and desorption are equivalent, as are the rates of transition from surface to bulk and bulk to surface. Setting Eq. (3.5) equal to Eq. (3.18) and Eq. (3.10) equal to Eq. (3.13) allows derivation of Eq. (3.19).

$$\frac{1-\chi}{\chi} P^{0.5} = \frac{\beta_0 (k_0 N_s)^{0.5} (2\pi \Re T M_{H_2})^{0.25}}{\nu_0 S_0^{0.5}} \left(\frac{F(\theta)(1-\theta)^2}{S(\theta)\theta}\right)^{0.5} \exp\left(\frac{E_{s-b} - E_{b-s} - E_{des}}{\Re T}\right) \quad (3.19)$$

Assuming ideal behavior, Sieverts' Law also describes the equilibrium relationship between pressure and hydrogen concentration and can be written as Eq. (3.20).

$$K_s^{-1} = \frac{P^{0.5}}{\chi} = \exp\left(-\frac{\Delta S^o}{\Re}\right)\exp\left(\frac{\Delta H^o}{\Re T}\right) \tag{3.20}$$

When Sieverts' Law is valid, χ <<1 and therefore the right-hand side of Eq. (3.19) can be set equal to the right hand side of Eq. (3.20). Using only the pre-exponential factor for each equation an expression can be found which relates the value of ν_o to the value of β_o:

$$\frac{\beta_0}{\nu_0} = \frac{S_0^{0.5}}{(k_0 N_s)^{0.5}(2\pi\Re T M_{H_2})^{0.25}}\left(\frac{S(\theta)\theta}{F(\theta)(1-\theta)^2}\right)^{0.5}\exp\left(-\frac{\Delta S^0}{\Re}\right) \tag{3.21}$$

This expression allows calculation of the pre-exponential factor for the surface-bulk transition as a function of the surface coverage. By assuming equilibrium and using Sieverts' Law to arrive at this equation the membrane behavior has effectively been forced to follow Sieverts' Law in the diffusion limited regime.

Table 3: Summary of variables used in the model calculations.

Variable	Class	Value	Units	Reference
E_{des}	constant	85	kJ/mol	[115]
$E_{s\text{-}b}$	constant	59.8	kJ/mol	[115, 122]
$E_{b\text{-}s}$	constant	22.15	kJ/mol	[37]
E_{diff}	constant	22.15	kJ/mol	[37]
k_o	constant	1.34e13	1/s	[115]
β_o	constant	7.68e12	1/s	Eq. (3.16)
D_o	constant	2.9e-7	M^2/s	[37]
N_b	constant	1.13e5	mol/m^3	[55]
N_s	constant	2.8e-5	mol/m^2	Eq. (3.11)
M_{H2}	constant	0.002	kg/mol H_2	-
ζ	constant	0.05	-	[115]
w	constant	2.1	kJ/mol	[115]
P_H	parameter	-	Pa	-
P_L	parameter	-	Pa	-
t	parameter	-	m	-
T	parameter	-	K	-
ν_o	unknown	-	1/s	-
θ_H	unknown	-	-	-
θ_L	unknown	-	-	-
χ_H	unknown	-	-	-
χ_H	unknown	-	-	-
$\dot{m}''$	unknown	-	mol $H_2/m^2/s$	-

3.1.7 Model Predictions

Although the complete model is slightly more involved than the one presented in Eq. (3.4), the same approach is still valid. The difference between the forward and reverse rates at the gas-metal and surface-bulk interfaces on both the upstream and downstream surfaces, along with the diffusion equation produces a system of five equations. Each of these equations is equal to the mass flux across the applicable interface and at steady-state they must all be equal. With the addition of Eq. (3.21) to calculate the surface-bulk pre-exponential factor, this becomes a system of six equations, six unknowns, and four parameters (see Table 3). For given parameter values (temperature, membrane thickness, upstream hydrogen pressure, and downstream

hydrogen pressure) the solution to the system of equations will yield the surface coverage (θ) and the near-surface atomic H:Pd ratio (χ) for both the upstream and downstream surface along with the overall hydrogen flux ($\dot{m}''$). If the desired outcome is the membrane performance under a given set of conditions this approach will suffice. However, additional information can be extracted from the model by assuming that each process is dominantly limiting the overall hydrogen permeation rate. In this case, each flux equation can be solved individually by assuming the others are quasi-equilibrium. This is done by setting the flux for the quasi-equilibrium equations to zero and solving for the equilibrium values of the unknown variables then substituting the equilibrium values into the remaining equation to calculate the hydrogen flux. This approach essentially imposes the entire pressure difference on each step to determine its contribution to the total mass transport resistance. Since these transport steps occur in series, the process which permits the smallest hydrogen flux will determine the flux for the entire system. Under these circumstances this step in the sequence is said to be the rate-limiting process.

The latter technique has been used to calculate the representative model predictions for a 100μm thick membrane exposed to a hydrogen pressure of 50 kPa on the upsteam surface and 0.5 kPa on the downstream surface. Due to the Arrhenius nature of the rate equations it is useful to plot them on an Arrhenius-type plot: a logarithmic scale for the hydrogen flux on the y-axis and inverse temperature on the x-axis. When plotted this way it can be seen that each process is characterized by a different slope, the activation energy for that process. Using this plot the rate-limiting mechanism should be distinguishable from experimental results by comparing the slope of the measured

permeation values to those predicted by the model. The results for a range of temperatures are shown in Figure 3.4. It is predicted that the rate-limiting transport mechanism under these conditions over the majority of the temperature range is the diffusion process. At lower temperatures the diffusion-limited curve intersects the desorption-limited curve. Below this temperature the hydrogen permeation rate becomes limited by the desorption process rather than the diffusion process. Experimentally, this transition would manifest itself as a change in the activation energy of the permeation process when the membrane operating temperature is reduced below the critical value indicated by the intersection. Under the conditions of Figure 3.4 the transition temperature is ~125 °C. As Pd-alloy membranes are typically operated at elevated temperatures to increase hydrogen flux it is likely that this transition would not be encountered during normal operation.

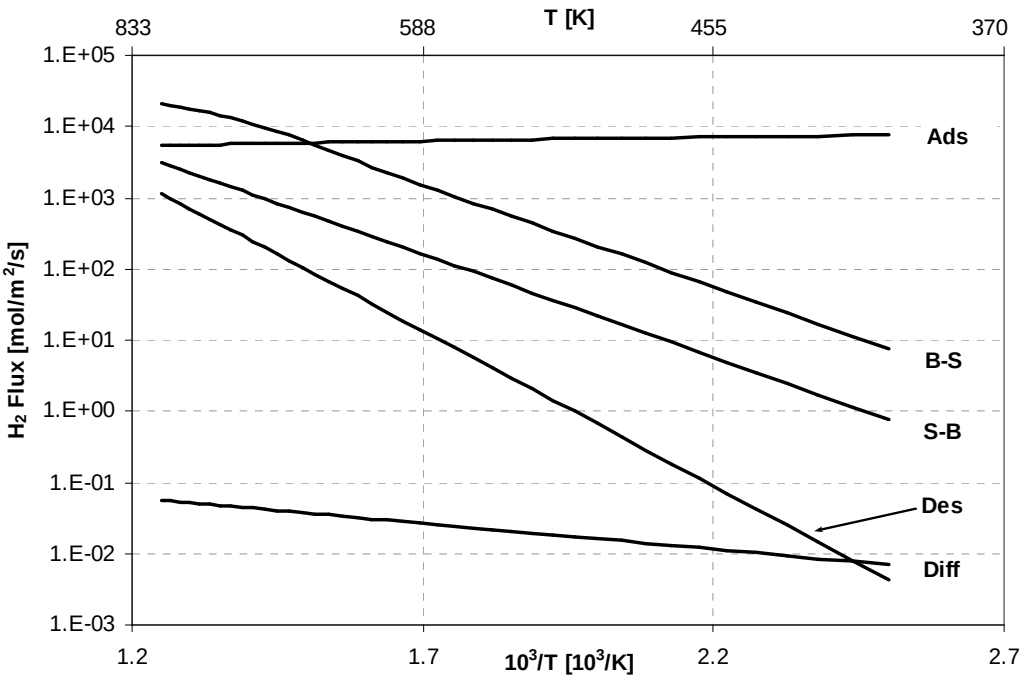

Figure 3.4: Hydrogen flux predictions using the Ward and Dao model for a 100μm thick membrane exposed to an upstream H_2 pressure of 50 kPa and a downstream H_2 pressure of 0.5 kPa.

The effect of membrane thickness on transition temperature is shown in Figure 3.5. In the model, membrane thickness only impacts the predicted diffusional flux; therefore all other curves are unchanged between Figure 3.4 and Figure 3.5. Since all other processes are much faster than diffusion and desorption they will not impact membrane performance and are not included in Figure 3.5. As membrane thickness is reduced, the transition temperature increases. This result is the major prediction of the Ward and Dao model which has a direct impact on the use of thin Pd-alloy membranes. As membrane thickness is reduced the transition temperature may shift to such an extent that even at high temperatures the membrane permeation is desorption-limited. In the desorption-limited regime, membrane performance is highly dependent on operating temperature, as indicated by the large activation energy for desorption. More importantly, for a given temperature, the desorption-limited permeation is unaffected by increasing the upstream pressure or decreasing the membrane thickness. Short of modifying the downstream surface to reduce the energy barrier for desorption, nothing can be done to increase the hydrogen flux above the desorption-limited curve. Thus, desorption-limited permeation represents a fundamental upper limit to the hydrogen permeation rate through Pd-alloy membranes.

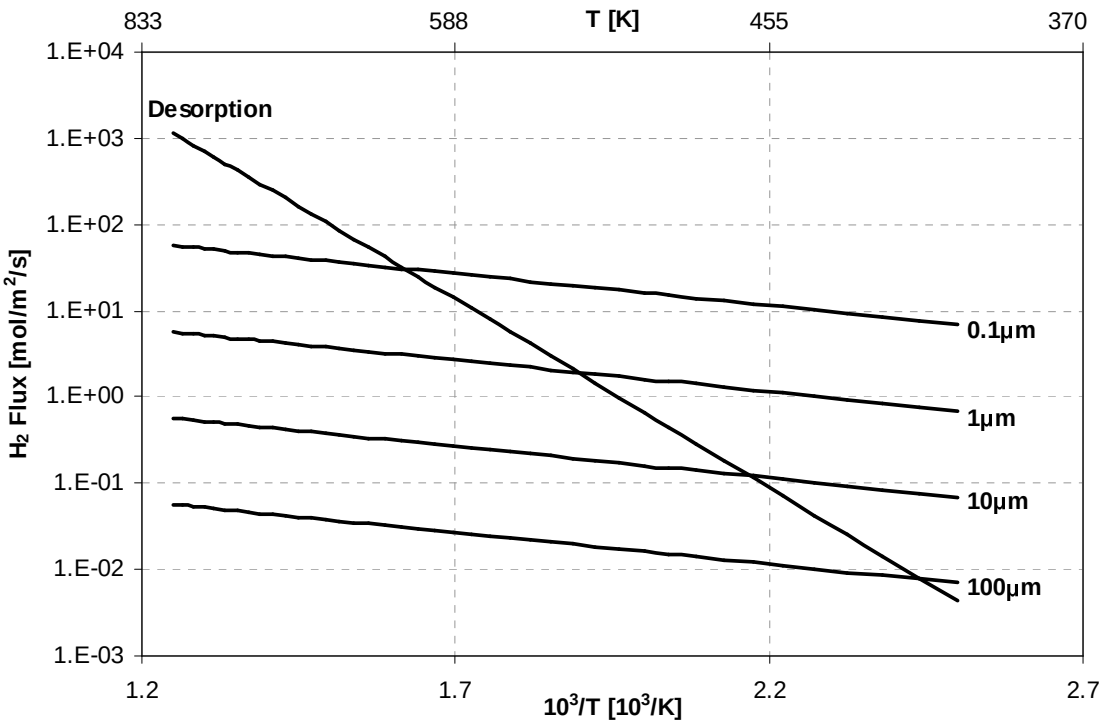

Figure 3.5: Desorption limited flux and diffusion limited flux prediction using the Ward and Dao model for membranes of varying thickness. Upstream H_2 partial pressure: 50 kPa, downstream partial pressure: 0.5 kPa.

In the predictions of the model presented above, the effects of gas-phase transport have been neglected. From a fundamental standpoint, these effects are unimportant as they are external to the limitations of membrane performance. However, in any real system gas-phase transport is a major concern and can contribute substantially to the overall mass transport resistance. When included in the model, transport of hydrogen to the membrane on the upstream surface and away from the surface on the permeate side simply add two additional series resistances. Thus far these resistances have been assumed negligible and have no impact on the predicted permeation rate. If included, they will not impact the location of the diffusion or desorption limited curves as these are calculated assuming all other resistances are zero, but they can add a significant contribution to the overall resistance and potentially become rate-limiting. Since the

fundamental performance limit dictated by the desorption rate is an upper limit on the hydrogen flux, any other significant transport resistance will inhibit reaching this curve. It is likely that the transport resistance through a commonly-used porous support layer would cause sufficient resistance to mask the effects of a transition into desorption-limited behavior.

3.1.8 Model Validation

The Ward and Dao model was developed specifically for the Pd-H system due to the availability of experimental data for nearly every aspect of the interaction of hydrogen and Pd. The abundant research conducted on this system made gathering accurate rate constants for the model possible. Unfortunately, as discussed in Chapter 2, Pd membranes suffer from hydrogen embrittlement when operated below the critical temperature of ~300 °C. The critical pressure is ~20 bar so the temperature can be lowered slightly by measuring permeation at lower pressures, but data for Pd membranes below ~200 °C at near-ambient pressure is virtually nonexistent. Since low temperature measurements are necessary to validate the Ward and Dao model, the lack of data at low temperatures due to failure of Pd membranes is indicative of a serious problem with this model which will be addressed in the forthcoming section along with the development of an improved permeation model.

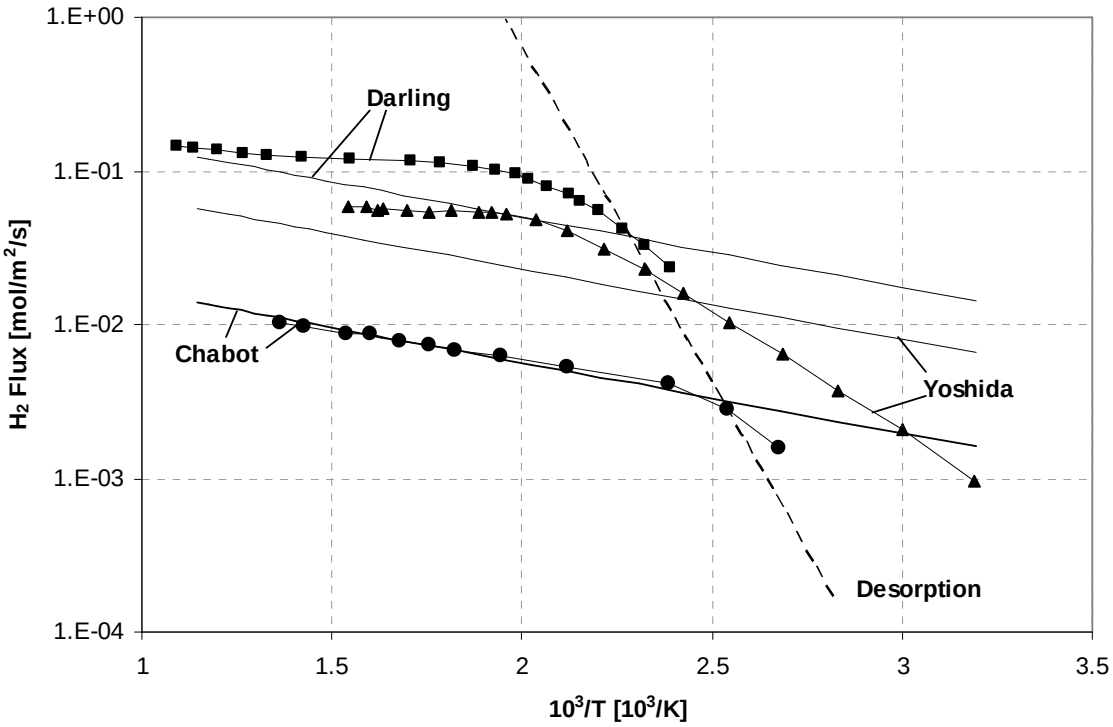

Figure 3.6: Hydrogen permeation measurements through thick $PdAg_{25}$ (75/25%) membranes from Darling , Yoshida , and Chabot [34, 123, 124]. The solid lines are the predicted diffusion limited permeation curves based on the operating conditions of each study (Table 4) using the Ward and Dao model. The dashed line is the desorption limited curve predicted by the Ward and Dao model.

One solution to the hydrogen embrittlement problem is to alloy Pd with ~25% Ag ($PdAg_{25}$). Since the critical temperature for this alloy is below 20 °C hydrogen embrittlement is no longer a problem for this material and experimental results for $PdAg_{25}$ membranes at low temperature are available. In addition, the diffusion coefficient and thermodynamic data for the interaction of this system with hydrogen have been well-characterized and can be substituted into the Ward and Dao model for the pure Pd values [35, 37]. Despite the fact that the surface interactions in the Ward and Dao model have been estimated for the Pd-H system it is assumed that the addition of 25% Ag has little impact on these values and they will be utilized without modification. The

predictions of the Ward and Dao model, incorporating the changes where data is available for the $PdAg_{25}$ alloy, are compared to experimental results in Figure 3.6.

Table 4: Experimental conditions for literature data used to validate permeation models.

Author	Membrane Thickness (μm)	Upstream H_2 Pressure (kPa)	Downstream H_2 Pressure (kPa)	Reference
Chabot	250	14	0	[34]
Darling	127	724	101	[124]
Yoshida	160	393	101	[123, 125]

In each of the data sets in Figure 3.6, there is a transition in the activation energy of permeation as the temperature is decreased. Above this transition the activation energy and the overall permeation rates are in reasonable agreement with the model predictions for diffusion-limited behavior. Below this transition the agreement between the data and the model prediction is quite poor. The transition occurs at roughly the correct temperature, but the predicted and measured activation energies are inconsistent. In the model, the desorption-limited regime is characterized by an activation energy of ~85 kJ/mol. Estimating the activation energy using the experimental data from Yoshida produces a value of 29.8 kJ/mol. Ward and Dao mentioned that within the literature there was some discrepancy between the measured values of heat of adsorption (equivalent to activation energy for desorption, see Figure 3.3) which range from 83 to 113 kJ/mol. Such a large spread for this value is not uncommon for studies of surface interactions. The properties of a gas-metal surface interaction are dependent on the crystallographic surface under investigation and can be highly affected by surface contamination. Due to this difficulty, surface analysis is typically conducted either by placing a sample in ultra-high vacuum then cleaving to expose a fresh crystal surface for study or a sample is repeatedly annealed under vacuum to segregate impurities to the surface and the

impurities are then removed *in situ*, often using an argon plasma to sputter the contamination from the surface. Despite careful sample preparation, substantial variation in reported results remains a problem.

Considering how surface properties are measured, it is not surprising that there is not perfect agreement between the experimental results and the model predictions for the desorption activation energy in Figure 3.6. The applicability of measurements made on an atomically clean surface to a real system is questionable. Further error is introduced since the data in Figure 3.6 is taken using a different material ($PdAg_{25}$ as opposed to Pd) and the real samples are undoubtedly polycrystalline without a well-defined crystallographic orientation.

Due to the assumptions in the model, it is tempting to overlook the disagreement between the activation energies in the desorption-limited regime and conclude that these results confirm the model predictions. However, additional analysis indicates that this conclusion might be premature. One of the implications of a transition into a desorption limited regime is that thickness and applied hydrogen pressure difference no longer have an impact on the hydrogen flux. Therefore, in Figure 3.6, all of the data should collapse onto a single curve in the desorption-limited regime. Clearly this is not the case, but the variation could also be attributed to subtle differences in the surface state between different studies so no definitive conclusions can be drawn. Alternatively, when permeation is limited by diffusion, all flux measurements for a given material can be normalized by dividing by the applied pressure difference and multiplying by the membrane thickness. The resulting quantity is the membrane permeability which is a bulk material property and should produce an equivalent value for all membranes at a

given temperature. If permeation results are measured in a desorption-limited regime permeability has no meaning and calculating this value from the measured flux should actually produce a larger spread in the data. The $PdAg_{25}$ permeability values calculated from the literature data are shown Figure 3.7. All of the data collapses fairly consistently onto a single curve indicating that diffusion is limiting the permeation over the entire temperature range. At elevated temperatures, the experimental results agree with the modeling.

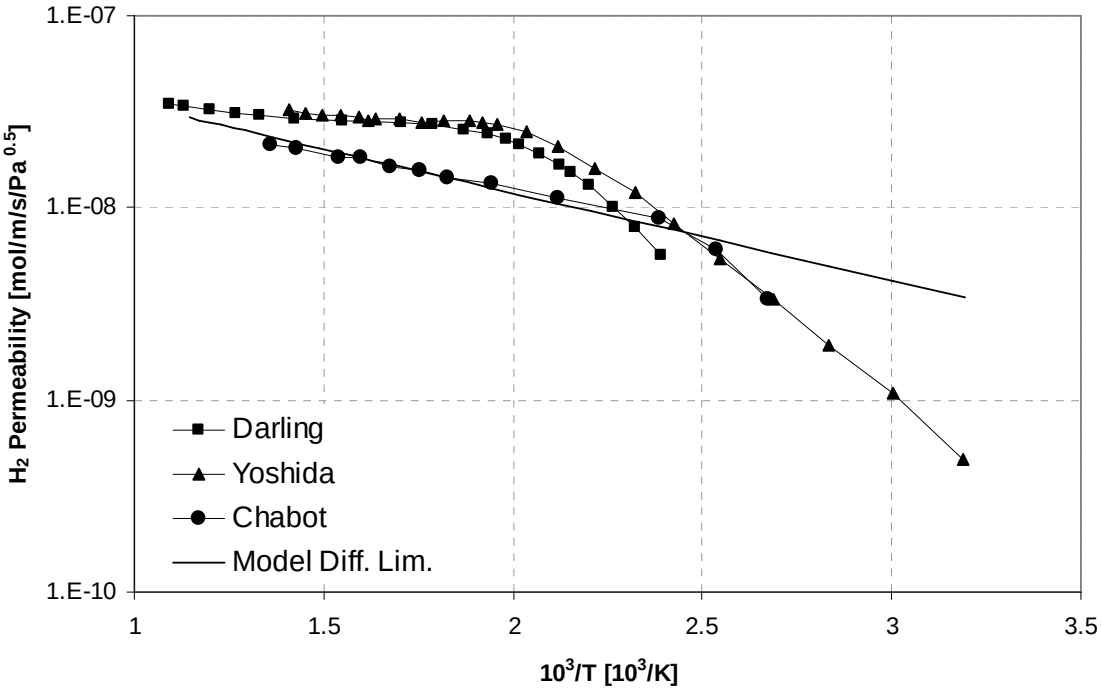

Figure 3.7: Permeability measurements for thick $PdAg_{25}$ membranes from the literature [34, 124, 125] and comparison based on diffusion-limited permeation from the Ward and Dao model.

Based on this analysis, it seems likely that some other phenomenon is causing the shift in activation energy rather than a transition into a desorption-limited regime. In order to uncover the cause of this behavior the model assumptions have been critically evaluated to identify the most likely area where the model is lacking.

3.2 The Improved Permeation Model

There are two key areas where the model of Ward and Dao is found to be inadequate. The first involves expressing the adsorption rate as a non-activated process. While this has been shown to be true on a clean metal surface, introduction of even small amounts of contamination can severely reduce the sticking coefficient [126-129]. This is an important consideration for practical membrane implementation, but the effects of contamination are not considered as fundamental transport limitations. Furthermore, the fact that the experimental data collapses onto a single permeability curve as shown in Figure 3.7 indicates that the behavior is due to a bulk phenomenon and cannot be explained by a surface process. The second area where the Ward and Dao model needs improvement is the estimate of the pre-exponential factor for the surface-to-bulk transition. Ward and Dao have invoked a thermodynamic relationship which forces the diffusion rate prediction to follow Sieverts' Law behavior. Chapter 2 discussed the sources of deviation from Sieverts' Law and demonstrated that these deviations can be quite large, especially at low temperature when absorption of large amounts of hydrogen by a metal leads to non-ideal thermodynamic behavior.

Since it is suspected that the behavior shown in Figure 3.6 is attributed to a bulk phenomenon, it is plausible that this behavior is a result of non-ideal hydrogen interactions. Although the $PdAg_{25}$ alloy does not enter the two-phase region at the experimental temperatures, the supercritical isotherms still exhibit non-ideal behavior. The improved model assumes that permeation is diffusion-limited, but seeks to accurately account for the non-ideal solution behavior of hydrogen in the $PdAg_{25}$ alloy. Surface effects are neglected although the modified model results could easily be superimposed

onto the Ward and Dao model results to generate a complete description of the permeation process.

3.2.1 Model Development

The utility of Sieverts' Law lies in the fact that it defines a simple and concise relationship between the hydrogen pressure, temperature and equilibrium concentration of absorbed hydrogen. The absorption isotherms using Sieverts' Law are simply of the form $P \propto \chi^2$. Unfortunately, Sieverts' Law is only valid over a fairly narrow range of temperature and pressure, while the Ward and Dao model uses this expression to make predictions outside of this range.

The foundational premise for the improved model is to develop an expression of the form $\chi(P,T)$ where the equilibrium absorbed hydrogen concentration is a function of temperature and pressure which is accurate over a broader range of temperature and pressure than Sieverts' Law. Specifically, this expression should accurately predict the hydrogen absorption behavior for the $PdAg_{25}$ system in the supercritical region (>20 °C) where these membranes would be utilized in practice. A nearly complete set of solubility data has been measured by Serra for the $PdAg_{25}$ system over the pressure and temperature range of interest [35]. This data is shown in Figure 3.8.

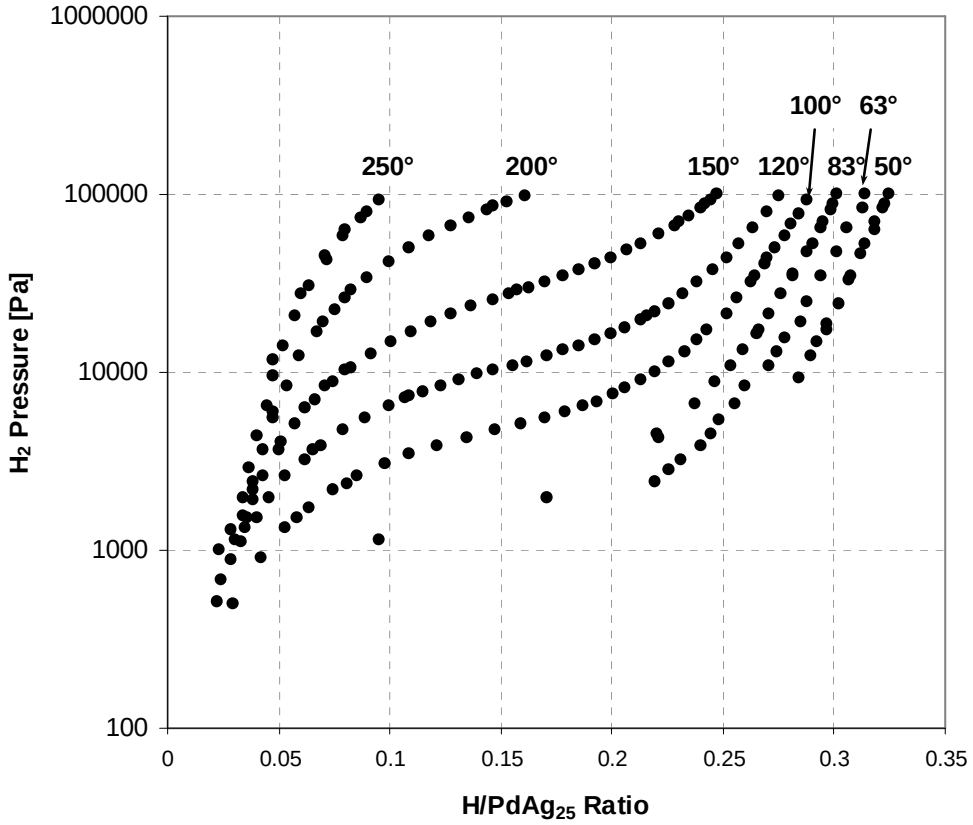

Figure 3.8: Pressure-composition data for the H:PdAg$_{25}$ system from Serra (temperature in °C) [35].

The problem is now reduced to developing an equation to accurately capture the trends exhibited in Figure 3.8. In order to retain predictive capabilities for operating conditions outside of the range of available data, the model will be based on the physics of the non-ideal behavior rather than a simple curve-fitting procedure. It was suggested in Chapter 2 that the chemical potential for an absorbed hydrogen atom in Pd can be expressed by Eq. (3.22). The standard potential term, μ_H^0, can be expanded in terms of the partial molar enthalpy (h_H^0) and partial molar entropy (s_H^0), Eq. (3.23).

$$\mu_H^s = \mu_H^0 + \Re T \ln\left(\frac{\chi}{1-\chi}\right) + \Delta\mu_{elast.} + \Delta\mu_{elect.} \tag{3.22}$$

$$\mu_H^0 = h_H^0 - Ts_H^0 \tag{3.23}$$

At equilibrium, the chemical potential of the absorbed hydrogen must be equal to the chemical potential of the hydrogen in the gas phase [Eq. (3.24)]. Setting these equations equal and solving leads to Eq. (3.25).

$$\mu_H^g = \tfrac{1}{2}\mu_{H_2}^g = \tfrac{1}{2}\left(\mu_{H_2}^0 + \Re T \ln P_{H_2}\right) = \tfrac{1}{2}\left(h_{H_2}^0 - Ts_{H_2}^0 + \Re T \ln P_{H_2}\right) \tag{3.24}$$

$$\ln P_{H_2}^{0.5} = \left(\frac{h_H^0 - \tfrac{1}{2}h_{H_2}^0}{\Re T}\right) - \left(\frac{s_H^0 - \tfrac{1}{2}s_{H_2}^0}{\Re}\right) + \ln\left(\frac{\chi}{1-\chi}\right) + \frac{\Delta\mu_{elast.} + \Delta\mu_{elect.}}{\Re T} \tag{3.25}$$

This equation has the potential to provide a useful relationship between the gas pressure, temperature and atomic ratio of hydrogen to Pd if the values of the constants are known and, more importantly, if the functional form of the excess potential term ($\Delta\mu_{elast.} + \Delta\mu_{elect.}$) is known. According to Wicke and Blaurock the excess potential in the supercritical region for Pd can be represented by a second order polynomial as in Eq. (3.26) with constants A and B [130, 131].

$$\Delta\mu_{elast.} + \Delta\mu_{elect.} = A\chi + B\chi^2 \tag{3.26}$$

It is logical to assume that the shape of the supercritical isotherms for the $PdAg_{25}$ system will be similar to those of Pd. Substituting Eq. (3.26) into Eq. (3.25) and grouping constants produces Eq. (3.27).

$$\ln P_{H_2}^{0.5} = C_1 + \frac{C_2}{T} + C_3 \ln\left(\frac{\chi}{1-\chi}\right) + \frac{C_4\chi}{T} + \frac{C_5\chi^2}{T} \tag{3.27}$$

Based on the derivation, Eq. (3.27) should be a physically accurate representation of the functional form of the relationship between pressure, temperature and hydrogen concentration for $PdAg_{25}$ alloys since their behavior is predominantly supercritical above atmospheric temperature. While this model is not an explicit equation of the form $\chi(P,T)$

is does permit an implicit calculation of χ for a given temperature and pressure. Using the data from Serra [35], the values of the coefficients in Eq. (3.27) can be found using a multivariable linear regression.

Although the solubility data from Serra is rather complete across the region where non-ideal behavior is observed, the data set is lacking information in the region where Sieverts' Law is valid. Taking solubility measurements in this region is typically not necessary as Sieverts' Law can be reliably used to calculate the hydrogen concentration. Also, taking solubility measurements in this region is difficult since the concentration of absorbed hydrogen is low. However, the modified model should predict ideal behavior in the limit of high temperature and low pressure and therefore some data in this region needs to be incorporated into the regression in order to capture these trends. Serra also reports a Sieverts' expression based on his experimental data and this expression is used to supplement the solubility data set with an additional three isotherms with ideal behavior. The complete set of data, including the supplemented data, is shown in Figure 3.9 alongside the model-based predictions for this data using Eq. (3.27). The model predictions match the experimental values quite well.

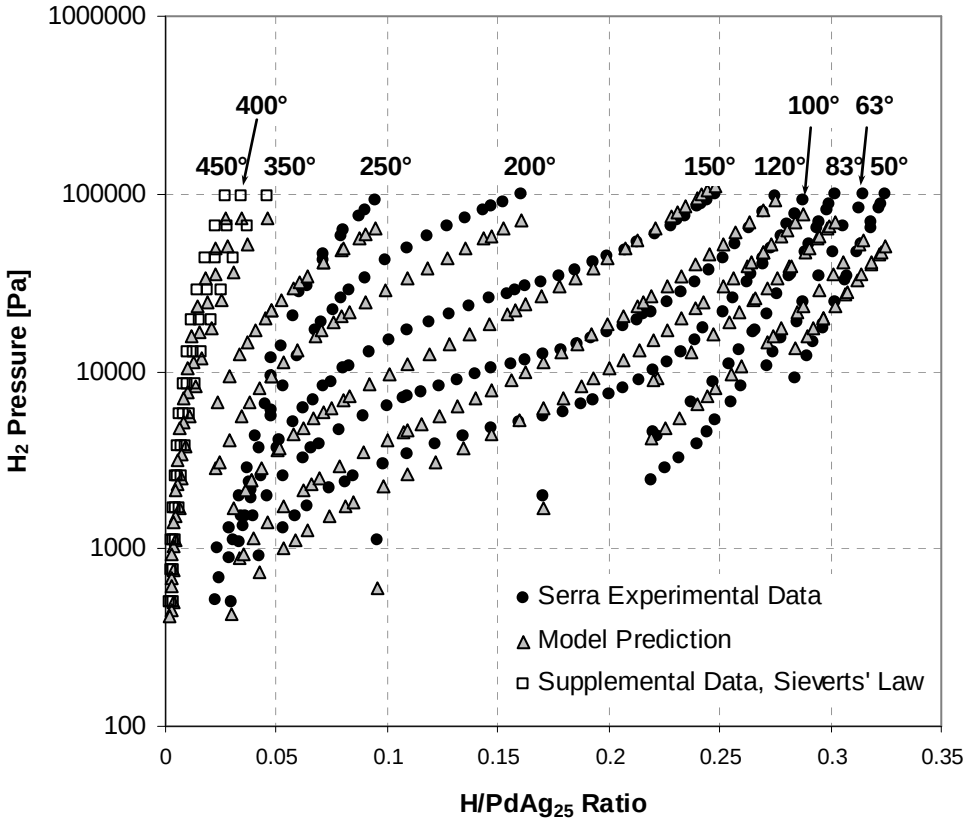

Figure 3.9: Experimental solubility data from Serra [35] used in the model regression along with the model predicted solubility data (temperature in degrees C).

Table 5: Regression results to determine the coefficient values in the improved permeation model, Eq. (3.27).

Coefficient	Value	Standard Error	t Stat	P-value	Lower 95%	Upper 95%
C_1	12.04	0.196	61.4	1.97E-152	11.65	12.42
C_2	-1915.5	62.01	-30.9	3.79E-87	-2037.6	-1793
C_3	1.022	0.0332	30.8	6.5E-87	0.957	1.088
C_4	-4217.6	464.5	-9.08	3.44E-17	-5132.4	-3303
C_5	13093	1130.5	11.6	4.25E-25	10866	15319

The numerical results of the regression are given in Table 5. The t-stat tests the null hypothesis that the actual value of each coefficient should be zero (the independent variable has no influence on the dependent variable) based on the Student's t-test. The P-value gives the probability that the given coefficient value might be found due to random

variation in the sample data even if the null hypothesis were true. The P-value can be loosely interpreted as the probability that a given coefficient is merely a product of noise in the data and therefore meaningless. The fact that the P-values in this regression are extremely small is an indication that each of the independent variables in the regression is significant and captures the trends exhibited in the data. The correlation coefficient (R^2) for the regression as a whole is 0.90, further indicating the validity of the model results.

An expression has now been developed which defines the thermodynamic relationship between pressure, temperature, and absorbed hydrogen concentration. This expression can be utilized to predict the hydrogen permeation behavior of a $PdAg_{25}$ membrane in a diffusion-limited operation regime by substituting the H:$PdAg_{25}$ atomic ratio values (χ_H and χ_L) calculated using the model, Eq. (3.27), into Eq. (3.28).

$$\dot{m}'' = D_0 \exp\left(-E_{diff} \big/ \Re T\right) \frac{N_b(\chi_H - \chi_L)}{2t} \tag{3.28}$$

The factor of two accounts for the fact that the flux of interest is of diatomic hydrogen.

3.2.2 Model Validation

As for the Ward and Dao model, the improved model predictions are compared to the experimental results of Chabot, Darling and Yoshida [34, 123-125]. This comparison is shown in Figure 3.10. The agreement between the model and the permeation results at elevated temperature is nearly perfect. At lower temperatures, the model captures the transition in activation energy quite well. The model predicts an increase in activation energy to a value of 30.6 kJ/mol compared to the value estimated from Yoshida of 29.8 kJ/mol. The model does a poor job of predicting the temperature at which this transition occurs. This is not surprising as the location of this transition is entirely dependent on the

shape of the predicted absorption isobars. This is shown in Figure 3.11 where the values of χ for the upstream and downstream surface are plotted in inverse temperature space. The Sieverts' Law predicted values are also shown. Plotting the values of χ as a function of inverse temperature allows the distinction between the Ward and Dao model and the proposed model to be clearly seen. At every temperature, the difference between the upper curve and lower curve in Figure 3.11 is linearly related to the predicted hydrogen flux since this is the concentration difference across the membrane driving the permeation process. The Ward and Dao model predicts that this difference is a constant value (in log space) as indicated by the fact that the Sieverts' Law prediction produces parallel lines for high and low pressure cases. The improved model captures some of the complexity of the actual experimental isobars. At high temperature the improved model and Sieverts' Law predict similar hydrogen concentration at both high and low pressure. As the temperature is reduced the differences between the models become apparent: first, the improved model predicts that the membrane surface in contact with the high pressure hydrogen gas will experience increased hydrogen absorption. This corresponds to the attractive H-H interactions manifested by the supercritical isobar passing over the two-phase dome (Figure 3.9). The slope of this isobar then drops dramatically and the predicted values of hydrogen absorption (and resulting hydrogen flux) fall below those of Sieverts' Law. At this point, the electronic contribution to the excess potential has slowed hydrogen absorption. The low-pressure isobar follows a similar path, although at different temperatures, and the interplay between these two curves dictates the membrane permeation behavior as a function of temperature.

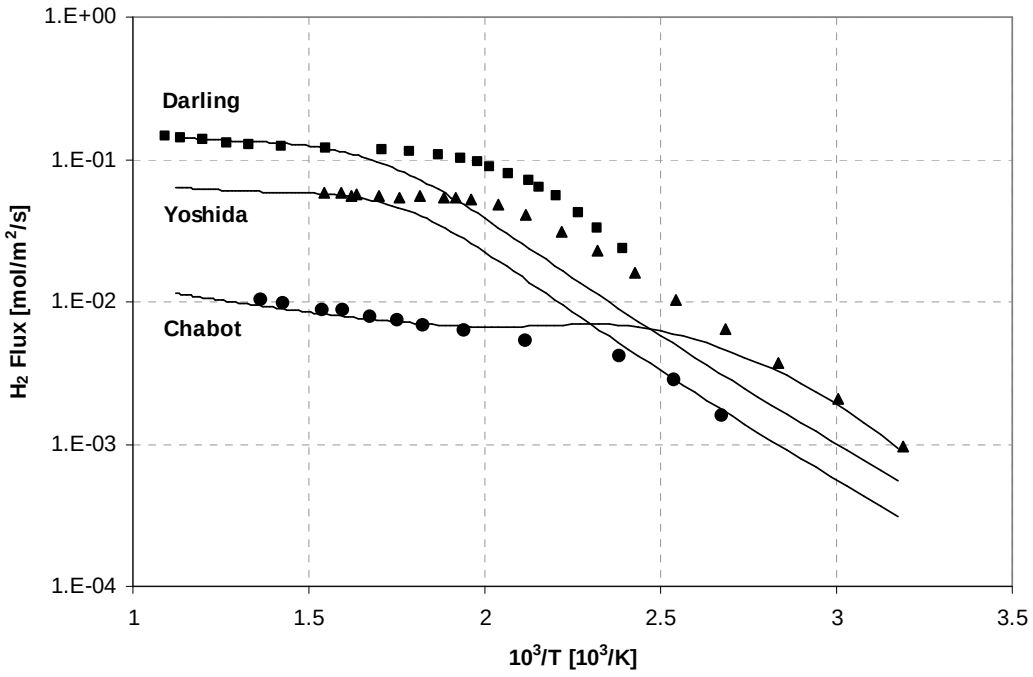

Figure 3.10: Hydrogen permeation measurements through thick $PdAg_{25}$ membranes from Darling , Yoshida , and Chabot [34, 124, 125]. The solid lines are the predicted diffusion limited permeation curves based on the operating conditions of each study using the improved model developed in this work.

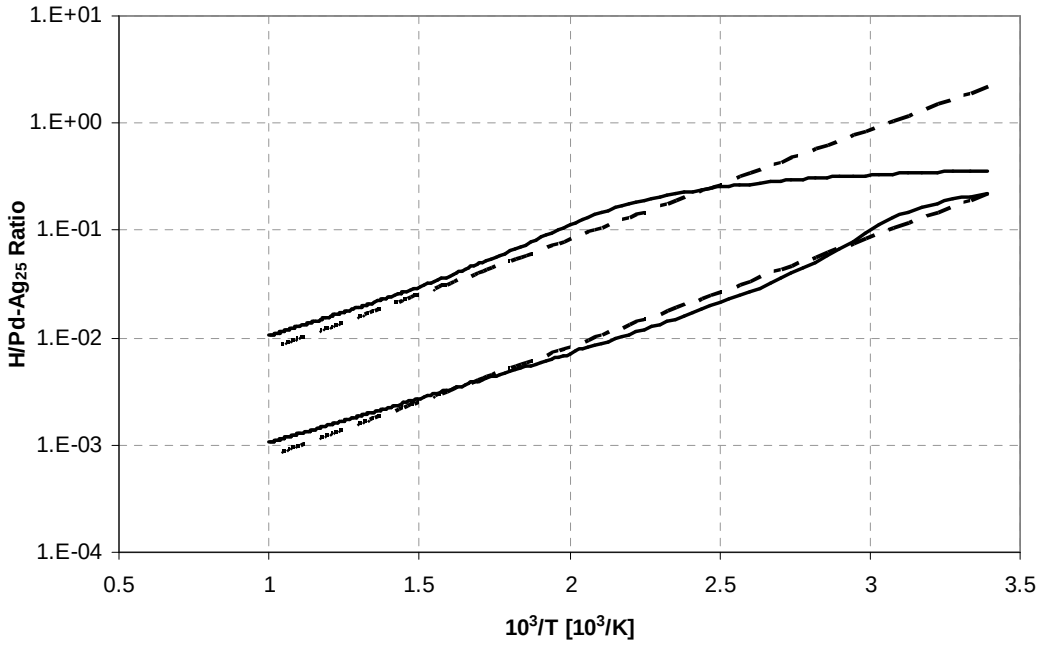

Figure 3.11: Atomic H:$PdAg_{25}$ ratio as a function of inverse temperature for a hydrogen pressure of 50 kPa (top curves) and 0.5 kPa (bottom curves). Dashed lines calculated using Sieverts' Law, solid curves as predicted from the improved model of this work.

3.3 Conclusions

The model developed by Ward and Dao has been shown to be inadequate to predict the behavior of relatively thick (125-250μm) $PdAg_{25}$ alloy membranes at temperatures below ~200 °C. Below this temperature, the hydrogen permeation behavior of these membranes exhibits an increase in the activation energy of permeation from a value of ~5-8 kJ/mol to a value of ~29.8 kJ/mol. The Ward and Dao model predicts there should be a transition into a desorption-limited permeation regime which is characterized by an increase in the activation energy, but to a much greater value of ~80-100 kJ/mol. This magnitude of increase in the activation energy is not observed experimentally.

An improved model is proposed which assumes that the behavior of these relatively thick membranes is diffusion-limited. Accounting for non-ideal solution behavior using first principles, the modified model accurately predicts the increase in activation energy to a value of ~30.6 kJ/mol as the temperature is decreased below 200 °C. Based on this model, the sharp decrease in hydrogen permeation rate at low temperatures can be attributed to the electronic contribution to the excess potential which limits the hydrogen solubility. This model is further verified, albeit indirectly, by the fact that experimental results for pure Pd membranes are not available in this temperature range. For pure Pd, the non-ideal hydrogen interactions cause embrittlement and failure and the lack of data for Pd under these conditions verifies the importance of the non-ideal contributions to hydrogen absorption behavior.

It is clear that simply searching for a transition in permeation activation energy is not an effective approach to determine whether a transition into desorption limited behavior has been reached. The fact that a transition does occur which is similar to the

predictions of the Ward and Dao model is potentially misleading without the development of the modified model to explain these results in the context of diffusion-limited permeation.

CHAPTER 4
EXPERIMENTAL METHODS

Having developed a permeation model that is capable of accurately predicting membrane behavior, it is now possible to correctly interpret experimental results for thin membranes in order to determine whether or not any fundamental limitations have been reached. On one hand, this requires careful experimental design in order to ensure that all external transport resistances are minimized and the permeation measurements can be attributed to the membrane intrinsic properties. On the other hand, in order to be able reach the desorption-controlled limit on permeation, the fabrication of extremely thin, free-standing membranes is needed to minimize the diffusional transport resistance. This section outlines the design of the experimental apparatus, the experimental procedures, and the details of the fabrication procedure used to fabricate free-standing Pd-Ag alloy membranes with a thickness on the order of 1 μm.

4.1 Membrane Fabrication

A microfabrication process has been designed using standard MEMS techniques which results in repeatable and robust fabrication of free-standing, sub-1μm thick Pd-Ag alloy membranes. A schematic of the multilayer structure comprising of the support, adhesion, and Pd-Ag alloy permeation layers is shown in Figure 4.1. The process starts with a [100]-oriented silicon wafer approximately 500μm thick. A thin silicon dioxide (SiO_2) layer is deposited using plasma-enhanced chemical vapor deposition (PECVD) to act as an etch stop for the thru-wafer etch performed later in fabrication. Next the Pd-Ag film is sputtered onto the wafer, sandwiched by a 20 nanometer thick Ti adhesion layer

on both sides. The Pd-Ag alloy is sputtered from an alloyed Pd-Ag target, ensuring uniform alloy composition throughout the film thickness. The film is then covered with an additional 4 - 6μm of PECVD SiO_2 to act as the membrane support scaffold. The last deposition step is another 4 - 6μm of PECVD SiO_2 on the backside of the Si wafer as a hard mask for the thru-wafer etch.

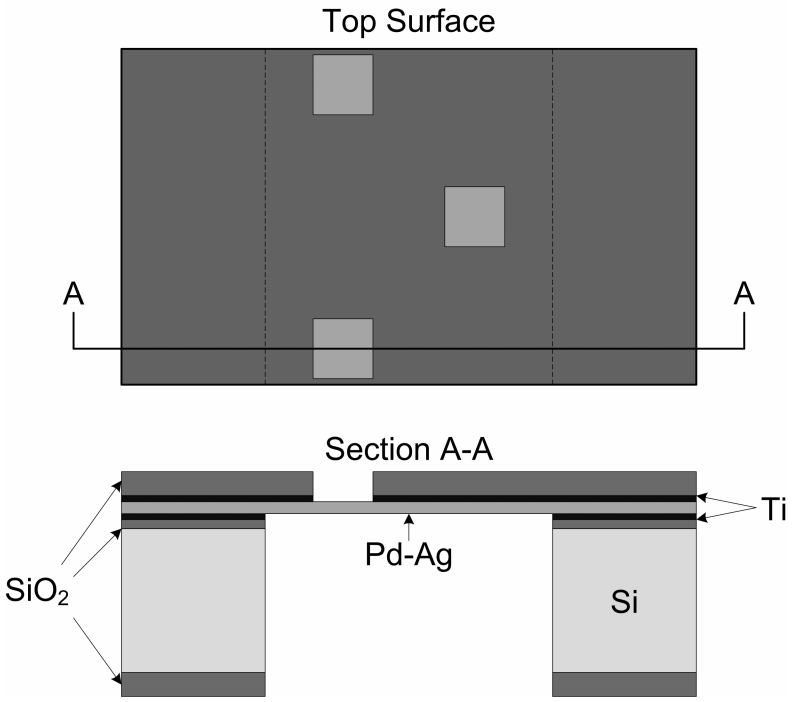

Figure 4.1: Schematic of the completed multilayer membrane structure (unit cell).

The topside of the wafer with the SiO_2-Ti-PdAg-Ti-SiO_2 structure is then patterned using standard photolithography techniques to expose an array of 25μm square features. The features are arranged such that they are only patterned directly above the areas where the Si will be removed from the wafer backside, Figure 4.3. This ensures precise control over the amount of Pd-Ag surface area which is eventually exposed from both sides. The exposed topside SiO_2 structure (within the 25μm squares) is then removed using a Reactive Ion Etch (RIE), Figure 4.2(b). The next step is patterning of the large (3.5mm x 150μm) thru-wafer features on the backside of the wafer. Standard

photolithography techniques are used and these features are aligned with the features on the topside of the wafer using a backside alignment technique. The Si substrate and SiO_2 etch stop layer are subsequently removed from the backside of the membrane using a Deep Reactive Ion Etching process (DRIE) leaving a free-standing composite Pd-Ag and SiO_2 structure, Figure 4.2(a). The last step is a wet etch of the Ti adhesion layers (Ti Etchant TFTN, Transene, inc.) leaving the final array of fully exposed Pd-Ag membranes.

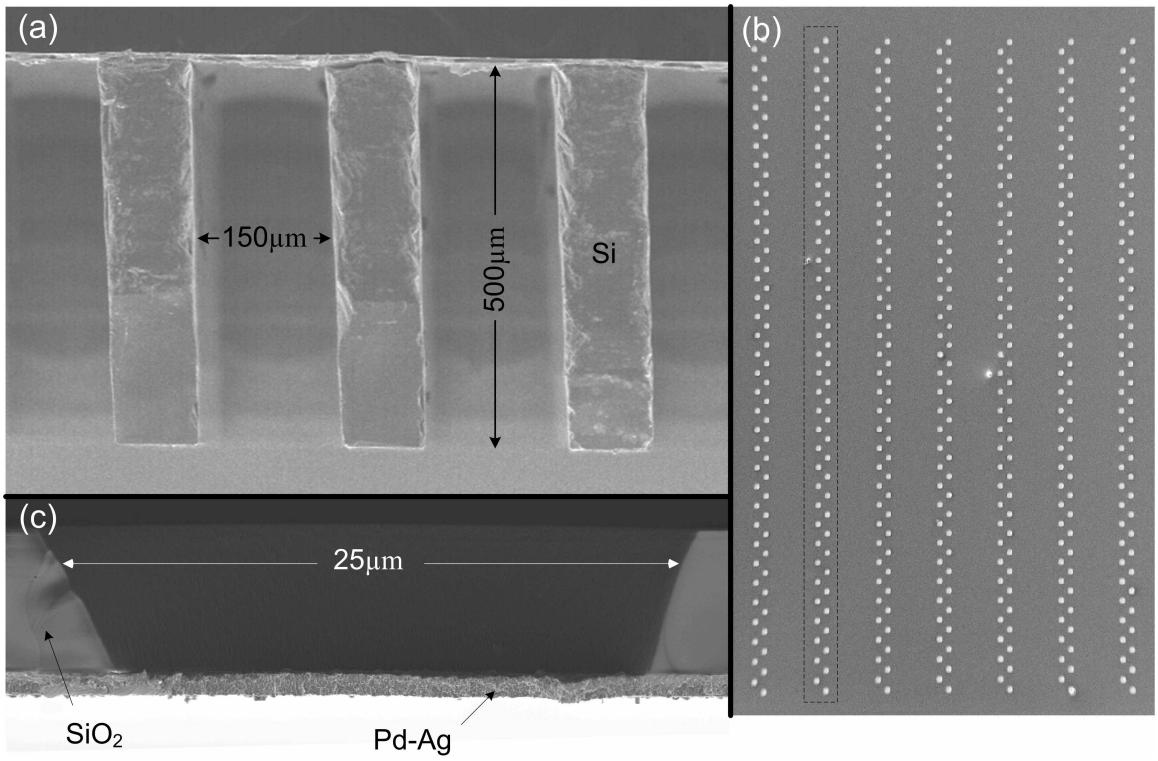

Figure 4.2: (a) Membrane cross-section showing vertical sidewalls etched through Si using DRIE. (b) Top view of pore array structure. Rectangle indicates approximate location of one backside window. (c) Pore cross-section showing Pd-Ag film and SiO_2 support layer.

The details of the two masks used to pattern these devices are shown in Figure 4.3. The backside windows are arranged in an 8 x 60 array covering $8cm^2$ on each membrane. Above each window there is an array of sixty-nine 25μm squares for a total of 33,120 individual square features exposing a combined area of $0.207cm^2$ of Pd-Ag on

each membrane. The exposed Pd-Ag is distributed over an area of 8cm^2 resulting in a fraction of active membrane area, γ, of ~0.026. In practice this value could be much larger but is deliberately set to a small value in this research to ensure accurate measurement of the intrinsic hydrogen permeation properties of the membrane by minimizing the effects of gas phase transport resistance. This will be discussed in more detail in Section 4.2. After dicing, the thickness of the Pd-Ag film was measured on the membrane edge using an SEM.

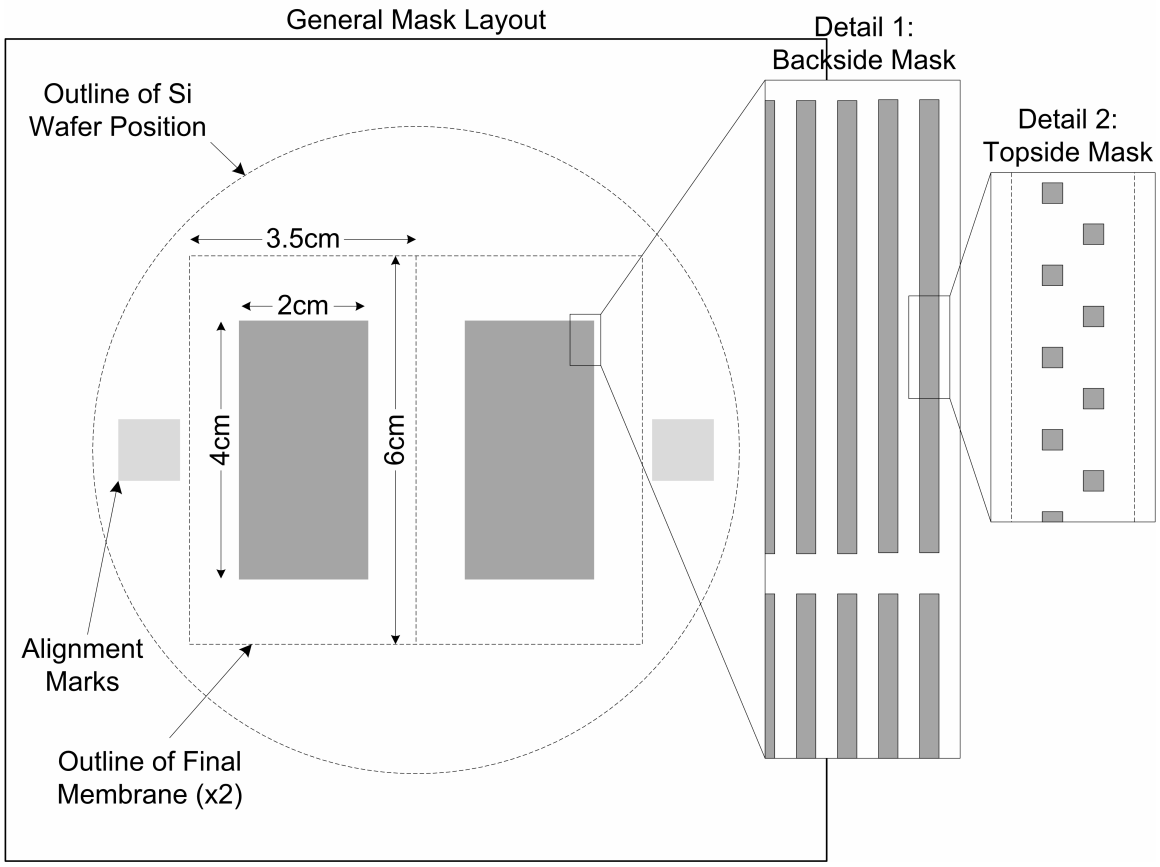

Figure 4.3: Photolithography mask layout. Only gray areas are mask features, dotted lines indicate position relative to other geometry.

4.2 Test Fixture Design

In order to realistically simulate the environment that a hydrogen diffusion membrane might encounter during operation we have chosen to utilize a standard gas

permeation fixture for testing. In such a fixture the membrane separates two gas flow channels, each with a different hydrogen pressure and this pressure difference across the membrane drives the permeation process. One main focus of this research is to study the performance of thin palladium-alloy membranes without the hindrance of a porous support layer. Since the membranes are free-standing and extremely thin, they are unable to support any appreciable absolute pressure difference across their thickness without rupturing. This presents a potential problem as there must be a difference in the hydrogen pressure across the membrane in order to drive permeation. One simple solution to this problem is to maintain an equal total pressure in each channel and vary the hydrogen partial pressure by changing the hydrogen mole fraction on each side of the membrane by mixing with another gas species. This approach has the benefit of avoiding mechanical stress on the membrane but also introduces a significant gas phase mass transfer problem. The high hydrogen flux through the membrane will rapidly deplete the gas environment of hydrogen near the high partial pressure surface and consequently enrich the gas environment near the low partial pressure surface with hydrogen. This effect, known as concentration polarization, decreases the imposed concentration gradient and results in substantially reduced hydrogen flux due to the small partial pressure difference in the gas region near the membrane surface. In order to minimize this effect, concerted effort must be made to maximize gas phase mass transport to and from the membrane surface. Gas phase mass diffusion is typically much slower than the hydrogen permeation process and therefore the mixture of gases needs to flow over the membrane surface in order to utilize the enhanced transport associated with the convection process.

In addition to local concentration polarization, the large hydrogen flux permissible through thin palladium alloy membranes can also deplete the hydrogen concentration in the bulk gas flow. By way of example, assume the hydrogen partial pressure is set to 50 kPa at the channel inlet by mixing a flow rate of 200 mol/s of hydrogen with the same flow rate of helium at a total pressure of 101 kPa (1 atm). If the hydrogen permeation rate through the membrane is 125 mol/s then the hydrogen flow rate at the channel exit has been reduced to 75 mol/s. As the helium cannot permeate the membrane the helium flow rate will remain 200 mol/s throughout the channel and at the channel exit the hydrogen partial pressure will have been reduced to 27.3 kPa. In order to obtain useful and reliable data it is vital that the operating environment of the membrane be controlled as closely as possible. This implies that for every value of measured hydrogen permeation the precise operating conditions are known. The existence of large concentration gradients, both transverse to the membrane surface (concentration polarization) and along each fixture channel, prevent precise control of the membrane operating environment and must therefore be minimized. The design of the test fixture to resolve these problems is considered in the next section.

4.2.1 Fixture Geometry and Characteristic Flow Rates

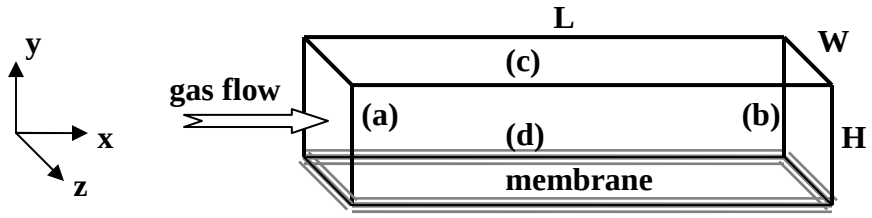

Figure 4.4: Flow channel schematic with channel dimensions and coordinate system.

Due to the fact that our fabrication procedure involves deposition onto a rigid silicon wafer, the fixture is restricted to a planar geometry. A generic flow channel is illustrated in Figure 4.4 with the letters L, W and H representing the channel length, width, and height respectively. The channel is of arbitrary dimensions but is restricted to a rectangular duct with mass transfer occurring on only one wall, the wall which will be the microfabricated membrane during testing. The boundary condition on the membrane wall is most closely represented as a constant mass flux condition as this is the ideal case. The other three walls can be treated as non-permeable from a mass transfer perspective as there will be no appreciable hydrogen permeation through the fixture walls. For clarity only half of the fixture is shown, the actual fixture will consist of another duct which is symmetrical about the membrane. This figure also sets the coordinate system for the channel. The gas flow is along the x-axis with the gas inlet at the origin. The y-axis is perpendicular to the membrane with the origin located at the membrane surface. Due to the symmetry across the width of the channel it is assumed that there is negligible variation in flow properties along the z-axis and the mass transfer problem may therefore be treated as two-dimensional in the x-y plane. Also included in Figure 4.4 are four regions within the channel designated by the letters (a)-(d). Point (a) is near $x = 0$, (b) is near $x = L$, (c) is near $y = H$, and (d) is near $y = 0$. Ideally, during testing, all four of these points will have the same hydrogen partial pressure and therefore the measured permeation rate can be attributed to that pressure, or more specifically to the difference between that pressure and the uniform pressure in the channel on the opposite side of the membrane. The permeation process itself makes this uniformity impossible. As mentioned earlier there are two effects that need to be considered to minimize these

concentration variations, concentration polarization or a gradient from points (c) to (d) and bulk flow gradients from points (a) to (b). Both of these gradients can be analyzed by comparison of three characteristic hydrogen flow rates: the molar flow rate of hydrogen into the channel ($\dot{m}_{H_2}^{in}$), the molar permeation rate of hydrogen through the membrane ($\dot{m}_{H_2}^{memb}$), and the molar flow rate of hydrogen to the membrane surface ($\dot{m}_{H_2}^{g}$). The flow of hydrogen into the channel is simply the hydrogen mole fraction (X_{H_2}) multiplied by the total gas molar flow rate ($\dot{m}_{tot}$):

$$\dot{m}_{H_2}^{in} = X_{H_2}\dot{m}_{tot} \tag{4.1}$$

The hydrogen permeation rate through the membrane is the product of the intrinsic hydrogen flux through the Pd-Ag alloy ($\dot{m}''_{\text{int}}$) and the amount of exposed, or active membrane surface area. The fabrication process allows this area to be controlled, and different than the channel footprint, by masking certain portions of the Pd-Ag film with the SiO_2 support structure. The fraction of exposed area relative to total membrane area will be denoted γ resulting in the following equation for the hydrogen flow rate through the membrane:

$$\dot{m}_{H_2}^{memb} = \dot{m}''_{\text{int}} LW\gamma \tag{4.2}$$

The molar flow rate of hydrogen to the membrane surface can be calculated using the mass transfer coefficient and driving concentration difference from the bulk fluid flow to the membrane surface, $\dot{m}_{H_2}^{gas} = h_m LW(C_B - C_S)$. The subscripts *B* and *S* denote the bulk fluid flow and the region near the membrane surface, respectively, and *C* is the hydrogen concentration (units of mol/m^3). Replacing hydrogen concentration with pressure using the ideal gas law results in

$$\dot{m}_{H_2}^{gas} = \frac{h_m LW}{\Re T}(P_B - P_S) \tag{4.3}$$

where $\Re$ is the universal gas constant, T is the absolute temperature and h_m is the convective mass transfer coefficient.

4.2.2 Design to Minimize Concentration Polarization

In practice, hydrogen transport to the membrane surface and transport through the membrane occur in series. Each of these steps can be considered as a resistance to hydrogen transport allowing an equivalent electrical circuit representation as shown in Figure 4.5. This figure includes both the permeate and retentate channels with a separate resistance for each. In this circuit the largest hydrogen pressure drop will occur across the element with the largest resistance and ideally this is the membrane itself, R_2. The mathematical representation for each resistance is included in Figure 4.5 next to the appropriate resistor. The criteria for minimizing the hydrogen pressure drop from the bulk gas flow to the membrane surface may be stated as $\{R_1, R_3\} << R_2$. Based on this relationship it is readily seen that the mass transfer coefficient needs to be maximized while the "active" membrane fraction, γ, should be minimized. The symbol R_{intr} is the intrinsic transport resistance through the membrane which relates the experimental variables such as temperature and hydrogen partial pressure difference to the intrinsic mass flux through the membrane. The intrinsic membrane resistance, and by extension the intrinsic mass flux through the membrane, are the quantities which the experiment is designed to measure and therefore cannot be altered.

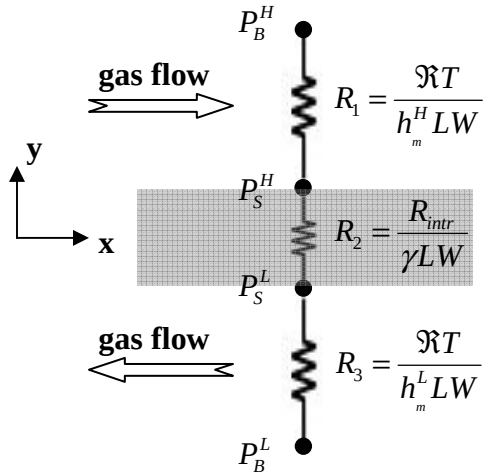

Figure 4.5: Equivalent resistance network for hydrogen transport in a gas-flow membrane test fixture. R_1 and R_3 are the gas phase transport resistances and R_2 is the membrane transport resistance.

The mass transfer coefficient is calculated from the equation

$$h_m = \frac{\mathrm{Sh} \cdot D_{ab}}{d_h} \tag{4.4}$$

where Sh is the non-dimensional Sherwood number, D_{ab} is the binary gas diffusion coefficient for species *a* and *b*, and d_h is the channel hydraulic diameter. For a rectangular duct the hydraulic diameter is defined as four times the duct cross-sectional area divided by the perimeter, or using the dimensions of Figure 4.4, $d_h = 4\mathbf{WH}/(2\mathbf{H}+2\mathbf{W})$. The diffusion coefficient is set by the operating temperature and gas species, but the Sherwood number and the hydraulic diameter are both functions of channel geometry. For fully-developed laminar flow in a rectangular duct with a constant flux boundary condition on one surface the Sherwood number is only a function of channel aspect ratio (width/height). The magnitude varies from a value of 2.712 for a square duct to a value of 4.851 for a channel with an aspect ratio of 10 [132, 133] and only further increases to 5.39 for parallel plates, or an infinite aspect ratio. Simultaneously with this increase in Sherwood number is an increase in hydraulic

diameter from a value of **H** for a square duct to a value of 2**H** for parallel plates effectively canceling the effect of aspect ratio on mass transfer coefficient. In fact, the predominant cause for the increase in Sherwood number is to account for the increase of hydraulic diameter with increasing aspect ratio as there is no fundamental reason for the mass transfer coefficient to change simply when the channel width is changed. While increasing channel width does not enhance mass transfer it will allow the active membrane fraction to be reduced for a given amount of active membrane area and channel length thereby increasing R_2. Additionally, for a given channel width decreasing the channel height will decrease the hydraulic diameter and increase the mass transfer coefficient. Based on this analysis, the gradient between points (c) and (d) from Figure 4.4 will be minimized if both the channel height and the active membrane area are made as small as possible.

4.2.3 Design to Minimize Bulk Flow Gradient from Channel Inlet to Exit

Minimizing the bulk flow gradient down the channel length is fairly straightforward. On the high partial pressure surface of the membrane the amount of hydrogen flowing into the channel needs to be large as compared to the amount of hydrogen permeating the membrane. On the low partial pressure side the amount of hydrogen permeating must be small relative to the flow rate of the sweep gas. Under these conditions the hydrogen partial pressure in the bulk flow will remain nearly constant down the length of the retentate channel and it will be nearly zero down the length of the permeate channel. Equation (4.5) is the ratio of hydrogen flow rate into the retentate channel (or flow rate of sweep gas into the permeate channel) [Eq. (4.1)] and the hydrogen flow rate through the membrane [Eq. (4.2)].

$$\frac{\dot{m}_{H_2}^{in}}{\dot{m}_{H_2}^{memb}} = \frac{X_{H_2}\dot{m}_{tot}}{\dot{m}''_{int} LW\gamma} \tag{4.5}$$

The hydrogen gradient down the length of the channel decreases as the value of this ratio increases. The hydrogen mole fraction will need to be systematically varied in order to determine the effect of varying partial pressure on the permeation rate and therefore cannot simply be increased to increase the ratio. As stated previously the intrinsic hydrogen flux through the membrane is the property which we are attempting to measure and therefore cannot be varied. The remaining variables which can be altered are the total mass flow rate into the channel, $\dot{m}_{tot}$, and the amount of exposed membrane area, $LW\gamma$. An upper limit for mass flow rate into the channel is controlled by the constraint that the gas flow into the channel needs to be heated to the fixture temperature before entering the channel. The larger the flow rate, the longer the heated length of tube upstream of the fixture must be to ensure thermal equilibrium. This flow rate is also constrained by the maximum allowable gas velocity in the fixture. If this velocity is too high the pressure drop down the length of the channel could be problematic. The other approach to increase the flow ratio is to decrease the amount of active membrane area.

4.2.4 Final Fixture Design

Based on the previous analysis the following statements can be made regarding fixture design and operation to minimize hydrogen concentration gradients in the gas flow channels:

1. The channel height should be minimized.
2. The fraction of active membrane area (γ) should be minimized.
3. The gas flow rates should be maximized.

In the test apparatus, the microfabricated membrane separates the upper half of the fixture from the lower half of the fixture and acts as a common wall between the two gas flow channels defined by each half of the fixture. The gas flow directions in the fixture are counter-current to maintain a roughly constant pressure difference over the entire channel length (as opposed to a converging pressure difference in a co-flow orientation). The membrane is sealed into the fixture using a high-temperature-compatible graphite gasket (graphitestore.com) between the membrane and each half of the fixture (Figure 4.6). In this configuration, the minimum channel height is defined by the thickness of the gasket: 1.5mm. This is the channel height for all experiments.

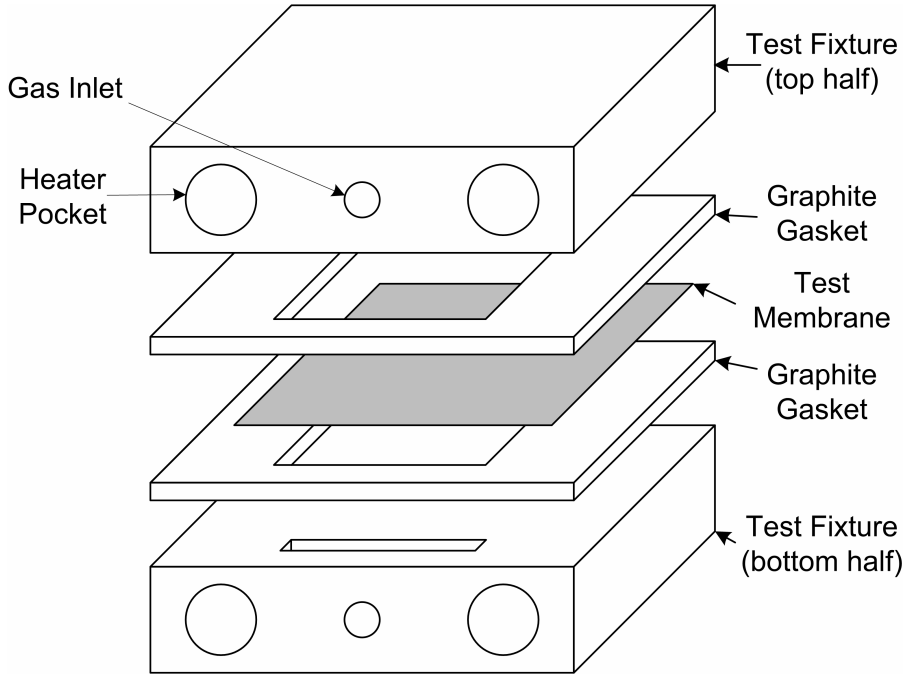

Figure 4.6: Exploded view of test apparatus assembly.

The lower limit for the fractional membrane area is set by the gas leak rate through the fixture. To carefully study membrane phenomena it is important to ensure that even at the lowest permeation rates the hydrogen signal is predominantly due to permeation through the membrane and not leaking around the membrane through the

gasket or through small porous defects in the membrane structure. As a measure of this leak rate, the hydrogen permeation rate can be compared to the helium permeation rate as helium will effectively locate any permissible path from retentate to permeate channel. For a defect-free membrane, the selectivity is virtually infinite and any detected helium will be due to leaking through the fixture. As the baseline case for the gas leak rate through the fixture the helium permeation rate was measured when the microfabricated membrane is replaced by a 54 μm thick Pd foil (Birmingham Metals). Due to the thickness and fabrication method of this foil it will be free of any thru-thickness defects and therefore the measured helium permeation rate is indicative of the leak rate through the fixture. The helium leak rate as a function of helium partial pressure at a temperature of 315 ^{o}C is shown in Figure 4.7. There is no detectable change in this leak rate as a function of temperature but it increases nearly linearly with an increase in partial pressure from roughly 0.02 up to 0.15 sccm (standard cubic centimeters per minute) as the pressure varies from 9-93 kPa. For comparison, the hydrogen permeation rate during the same experiment varied from 10 to 45 sccm for a similar range of pressures leading to a hydrogen-helium selectivity of between 300 and 500 for the thick Pd foil.

For this study, it was decided that a maximum of 1% of the H_2 detected should be attributed to leaking through the fixture. Making the conservative assumption that the H_2 leak rate is the same as the He leak rate at a given partial pressure, the amount of exposed Pd-Ag must be sufficient to ensure that the H_2 permeation rate is at least 2 sccm at 9 kPa and at least 15 sccm at 93 kPa across the entire temperature range. Utilizing H_2 permeability values available in the literature leads to a required surface area of ~0.05cm^2 for a 1μm thick membrane to achieve this goal. An active surface area of 0.21cm^2 was

chosen, ensuring that the measured H_2 permeation rates are dominated by actual membrane phenomena and not leaking through the graphite gasket.

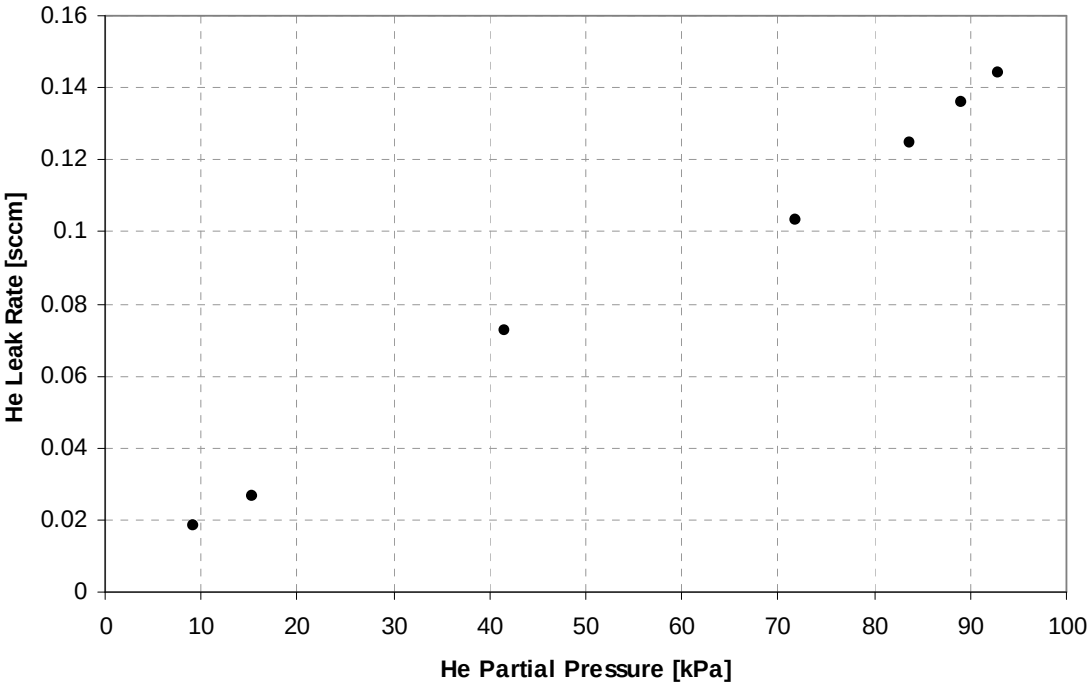

Figure 4.7: Helium leak rate as a function of helium partial pressure as measured during permeation testing on the 54μm thick Pd foil.

Having chosen the active surface area, choosing the acceptable gradient down the length of the channel determines the necessary gas flow rates into the fixture. The H_2 flow was varied from 50 to 400 sccm while the He flow was varied from 1050 to 700 sccm. These flow rates gave a variation in H_2 partial pressure from 4.6 kPa to 36.8 kPa and at 450 °C kept the hydrogen partial pressure change down the length of the retentate channel below 15%. On the permeate side, the argon sweep gas flow rate was kept at 750 sccm with a maximum of 5% H_2 in the permeate stream at the channel exit. To assign a definite pressure difference to each hydrogen permeation measurement two steps were taken. First, the average pressure in each channel was calculated based on the H_2

partial pressure at the channel inlet and exit. The value at each channel inlet is known (variable in the upstream channel and zero in the downstream channel) and the value at the exit was calculated based on the measured permeation rate. The average pressure near the membrane surface was then calculated using the average pressure for the bulk flow, the measured hydrogen flux, the mass transfer coefficient, and Eq. (4.3). The binary gas diffusion coefficients for the Ar-H_2 and He-H_2 mixtures are calculated using the theoretical expression derived by Hirschfelder et. al. (1969) and the Lennard-Jones 6-12 potential as described in the text by Hines and Maddox [80]. The binary diffusion coefficient for the He-H_2 mixture is roughly twice as large as for the Ar-H_2 mixture, therefore the microfabricated devices are oriented with the thru-wafer features facing the He-H_2 mixture. The mass transfer coefficient on this surface is calculated as the combination (in series) of the convective mass transfer in the flow channel and purely diffusive mass transfer through the 500μm deep windows.

The only remaining decision to be made regarding channel geometry is the length and width. The requirement to minimize the convective gradient has dictated that the product should be as large as possible but has put no constraints on the magnitude of each length individually. An additional constraint is found in a previous assumption about the gas flow over the membrane surface. When analyzing the effect of aspect ratio on Sherwood number it was assumed that the flow was fully developed which has the convenient result that the Sherwood number is a constant, independent of the distance x along the channel length. In reality there will be a certain distance along the x-axis, henceforth called the entrance length, where the flow is developing and the Sherwood number is not constant. For flow between parallel plates with constant flux on one

surface and an insulated boundary on the other the precise dependence of the Sherwood number on distance has previously been calculated and will give a good estimate of the entrance length [132, 133]. The results of these calculations are shown in Figure 4.8.

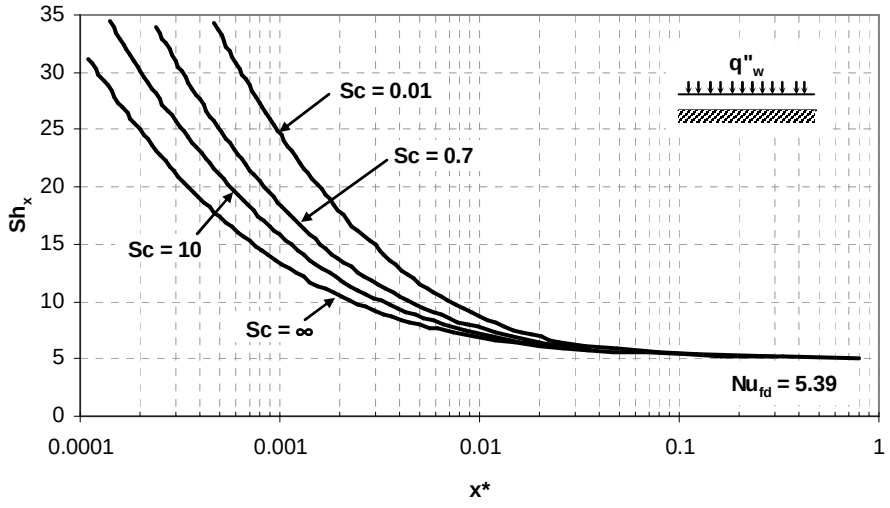

Figure 4.8: Sherwood number as a function of non-dimensional entrance length for constant flux-insulated boundary conditions on parallel plates [132, 133].

Curves are shown for several values of Sc, the non-dimensional Schmidt number, which is defined as the ratio of kinematic viscosity, ν, to diffusion coefficient, D_{ab}. Regardless of the Schmidt number the Sherwood number becomes constant, and therefore the flow is fully-developed, when x^* is roughly 0.1. The non-dimensional distance x^* is defined as $x^* = \frac{x/d_h}{\mathrm{Re}\cdot\mathrm{Sc}}$ where Re, the Reynolds number, is defined as $\mathrm{Re} = \frac{V\cdot d_h}{\nu}$ with V the fluid velocity. The equation for x^* can be rearranged to derive an explicit expression for the entrance length. For our assumption of a fully-developed flow to be reasonable it is necessary that the entrance length is a small fraction of the total channel length, or the quantity x/L is small. Dividing the entrance length equation by the channel length

produces an equation which is monotonically decreasing as the channel length increases. Therefore a long and narrow channel is preferable to a short and wide channel.

The last constraint on channel geometry comes from the fabrication process. The majority of the cleanroom equipment necessary for device fabrication is only compatible with standard four inch diameter wafers. This sets a maximum on the channel length and defines a relationship between maximum channel length and number of devices per Si wafer. A design was chosen with two membranes per wafer where the patterned area is 2cm x 4cm (Figure 4.3). The remaining border on the membrane has no features but is necessary to clamp the membrane into the test fixture. In the fixture the flow channel covers only the membrane area where features are patterned resulting in final channel dimensions (H x W x L) of 1.5mm x 2cm x 4cm.

The test fixture was machined from bulk Inconel (hightempmetals.com) and heated using four embedded cartridge heaters (Dalton Electric) that are controlled by an Automatic Temperature Controller (Harrick Scientific). The temperature controller used a thermocouple embedded in the fixture for feedback (K-type, OMEGA.com). The temperature was also monitored at each gas inlet and exit and three additional locations along the fixture centerline to ensure temperature uniformity. The inlet gas streams were heated by passing through a serpentine length of stainless steel tubing maintained at the correct temperature by intimate contact with the outer surface of the fixture. Gases were supplied from tanks (Airgas) at ultra-high purity (99.999% pure) and metered with mass flow controllers (Model 1179A and 1259C, MKS Instruments).

4.3 Mass Spectrometer Calibration

As the argon sweep gas passes through the test fixture it collects any gases permeating the membrane. This gas mixture is sampled by a quadrupole mass spectrometer (HPR-20, Hiden Analytical) upon leaving the fixture to measure the ratio of argon to helium or hydrogen. The permeation rate (or leak rate) of hydrogen and helium can be calculated by multiplying the fraction of these gases in the permeate stream by the argon flow rate into the fixture.

In order to get accurate quantitative data using a quadrupole mass spectrometer frequent calibration must be performed to calculate the relative sensitivity of the mass spectrometer to the gas species of interest [134]. This calibration involves supplying the mass spectrometer with a gas mixture of known composition and monitoring the gas composition reported by the mass spectrometer. If this is done for several different gas compositions a line can be plotted relating the reported composition to the actual composition as shown in Figure 4.9. In this case the slope of the resulting line is the relative sensitivity of H_2 to Ar.

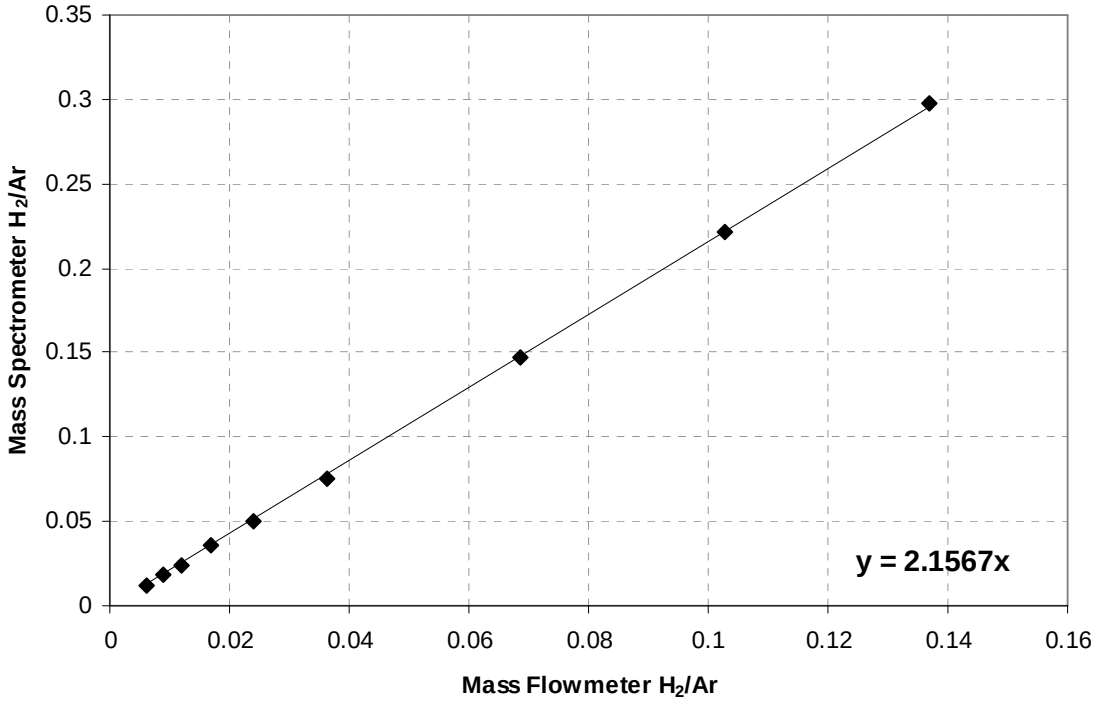

Figure 4.9: Mass spectrometer calibration curve to calculate the relative sensitivity of H_2 to Ar.

This type of calibration was performed every few days when testing was frequent to ensure accurate measurements of the hydrogen permeation rate. The relative sensitivity values for H_2 relative to Ar ranged from 1.5 to 2.5. However, the drift in relative sensitivity was gradual, never changing by more than a few percent every few days. The relative sensitivity for He was measured much less frequently and remained close to 0.5.

4.4 Uncertainty Analysis

The values of hydrogen flux, permeance, and permeability reported in this study are calculated as functions of the measured values of partial pressure, gas flow rates, membrane thickness, and the membrane surface area. This section calculates the propagation of error from these measurements to the final calculated values.

The hydrogen flux is calculated by multiplying the relative amount of H_2 detected by the mass spectrometer (PP_{MS}) by the Ar flow rate (FR_{Ar}) and dividing by the exposed Pd-Ag surface area ($A_{Pd\text{-}Ag}$), Eq. (4.6). The absolute uncertainty for the hydrogen flux, $\delta\dot{m}''$, can be calculated using Eq.(4.7). Equation (4.7) can be simplified by evaluating the partial derivatives and dividing the entire expression by the hydrogen flux. The result is the relative uncertainty, Eq. (4.8), and is a simple function of the relative uncertainties of the three components of the hydrogen flux.

$$\dot{m}'' = \frac{PP_{MS} FR_{Ar}}{A_{Pd-Ag}} \tag{4.6}$$

$$\delta\dot{m}'' = \left[\left(\frac{\partial \dot{m}''}{\partial PP_{MS}} \delta PP_{MS} \right)^2 + \left(\frac{\partial \dot{m}''}{\partial FR_{Ar}} \delta FR_{Ar} \right)^2 + \left(\frac{\partial \dot{m}''}{\partial A_{Pd-Ag}} \delta A_{Pd-Ag} \right)^2 \right]^{1/2} \tag{4.7}$$

$$\frac{\delta\dot{m}''}{\dot{m}''} = \left[\left(\frac{\delta PP_{MS}}{PP_{MS}} \right)^2 + \left(\frac{\delta FR_{Ar}}{FR_{Ar}} \right)^2 + \left(-\frac{\delta A_{Pd-Ag}}{A_{Pd-Ag}} \right)^2 \right]^{1/2} \tag{4.8}$$

The permeance is calculated by dividing the hydrogen flux by the applied hydrogen partial pressure difference to the one-half power. This leads to an additional term to calculate to relative uncertainty of the hydrogen permeance:

$$\frac{\delta Permeance}{Permeance} = \left[\left(\frac{\delta PP_{MS}}{PP_{MS}} \right)^2 + \left(\frac{\delta FR_{Ar}}{FR_{Ar}} \right)^2 + \left(-\frac{\delta A_{Pd-Ag}}{A_{Pd-Ag}} \right)^2 + \left(-\frac{1}{2}\frac{\delta P}{P} \right)^2 \right]^{1/2} \tag{4.9}$$

Finally, the permeability is calculated by multiplying the permeance by the membrane thickness, the relative uncertainty for this calculation is expressed by:

$$\frac{\delta\Phi}{\Phi} = \left[\left(\frac{\delta PP_{MS}}{PP_{MS}} \right)^2 + \left(\frac{\delta FR_{Ar}}{FR_{Ar}} \right)^2 + \left(-\frac{\delta A_{Pd-Ag}}{A_{Pd-Ag}} \right)^2 + \left(-\frac{1}{2}\frac{\delta P}{P} \right)^2 + \left(\frac{\delta t}{t} \right)^2 \right]^{1/2} \tag{4.10}$$

The thickness measurements were taken at six different locations and exhibited a maximum variation from the calculated average value of 5.6%. The area used in all calculations was the nominal value from the mask design of 0.207cm^2. It can be seen in Figure 4.2(c) that the topside SiO_2 etch does not always produce vertical walls down to the membrane surface. A maximum angle of 15 degrees was observed upon inspection leading to a reduction in the actual exposed Pd-Ag surface area from the nominal value. The maximum of value of this deviation is 12.2%. The argon flow rate is controlled by a flow meter with an accuracy of +/-1% of full scale, or +/-50sccm. This corresponds to 6.7% of the Argon flow rate used in this study. The hydrogen and helium flow rates in the upstream channel also have an accuracy of +/-1% of full scale, or a flow rate of +/-5sccm and +/-50sccm respectively. This produces a maximum relative uncertainty for the hydrogen partial pressure of 11% at low partial pressures. The last uncertainty necessary to complete the above calculations is the mass spectrometer measurements. Due to the frequency of calibration, the stability of the calculated relative sensitivity values, and the excellent fit in the slope of the relative sensitivity line to the calibration data (Figure 4.9), a conservative estimate for the relative uncertainty of the mass spectrometer measurements was made at +/-5%. Incorporating these values into the equations above yields an uncertainty of +/-14.8% for the reported H_2 flux, +/-15.8% for the reported H_2 permeance, and +/-16.7% for the reported H_2 permeability values.

CHAPTER 5
EXPERIMENTAL RESULTS

This chapter summarizes the experimental results on microfabricated $PdAg_{25}$ membranes. As an initial validation of the experimental apparatus and hydrogen permeation rate measurements a pure Pd foil with a thickness of 54μm (Birmingham Metals) was tested. The results of these experiments are presented first. In order to avoid the complications of non-ideal behavior, microfabricated membranes were initially tested at elevated temperature, from 250 to 450 °C, for comparison to literature results. The results of these experiments are presented second. Finally, each membrane was tested at low temperature to determine whether a transition into desorption-limited behavior could be detected. Throughout testing there were two failure modes encountered. The conditions of each of these failure modes will be discussed along with the implications for further research. Finally, the procedure and dynamics of membrane "activation" prior to each experiment will be presented and discussed. The long transient increase in permeation rate upon initiating hydrogen permeation testing on a given membrane is superimposed on microstructure evolution characterization to correlate the permeation measurements with the change of grain size distribution.

5.1 Thick Pd Foil Characterization

In order to ensure that the hydrogen permeation rate could be accurately measured using the designed apparatus, a 54μm thick Pd foil (Birmingham Metals) was characterized before beginning testing of the microfabricated membranes. Due to the large thickness of this foil, the behavior should be diffusion limited and the results can be

compared to values available in the literature for validation. In order to avoid non-ideal hydrogen absorption effects and hydrogen-induced embrittlement, the Pd foil was only tested in the temperature range of 315-415 °C, above the Pd critical temperature. The temperature was ramped up from 315 °C to 415 °C and back down at a one degree per minute heating rate while sampling the permeate stream every 15 seconds using the mass spectrometer. This test was performed for three different hydrogen partial pressure settings at the inlet to the upstream channel: 101 kPa, 43.2 kPa, and 16.9 kPa. The results are shown in Figure 5.1.

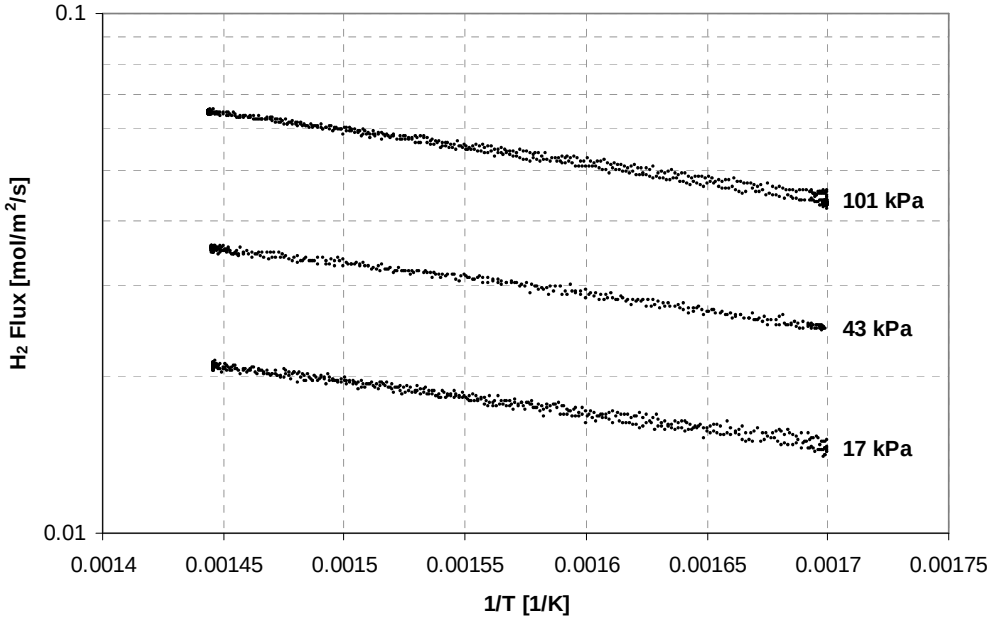

Figure 5.1: Measured hydrogen fluxes for 54μm thick Pd foil (Birmingham Metals).

Since the Pd foil is unsupported and the entire surface is available for hydrogen permeation, the total rates of hydrogen permeating through the foil are comparable to the total rates of hydrogen permeating through our ultra-thin membrane, which has much smaller exposed (available for permeation) area. This is important as the total rate of hydrogen permeation is the relevant parameter used to ensure hydrogen concentration

uniformity in the gas channels. For comparison to the literature values, the permeability was calculated for this data set by multiplying by membrane thickness and dividing by the square-root of partial pressure difference across the membrane. This permeability data is shown in Figure 5.2. The data collapses onto a single curve indicating that indeed diffusion is limiting the overall transport. The permeability is calculated by fitting this data with an exponential function to determine the pre-exponential factor and activation energy for the hydrogen permeability. The regression equation and the correlation coefficient (R^2) for the regression are shown alongside the data in Figure 5.2. The calculated permeability values are compared to values from the literature in Table 6. There is excellent agreement between the measured hydrogen permeability and the values from the literature. This provides validation for the test fixture design and experimental protocols described in Chapter 4 for the testing of ultra-thin Pd-Ag membrane that will be discussed next.

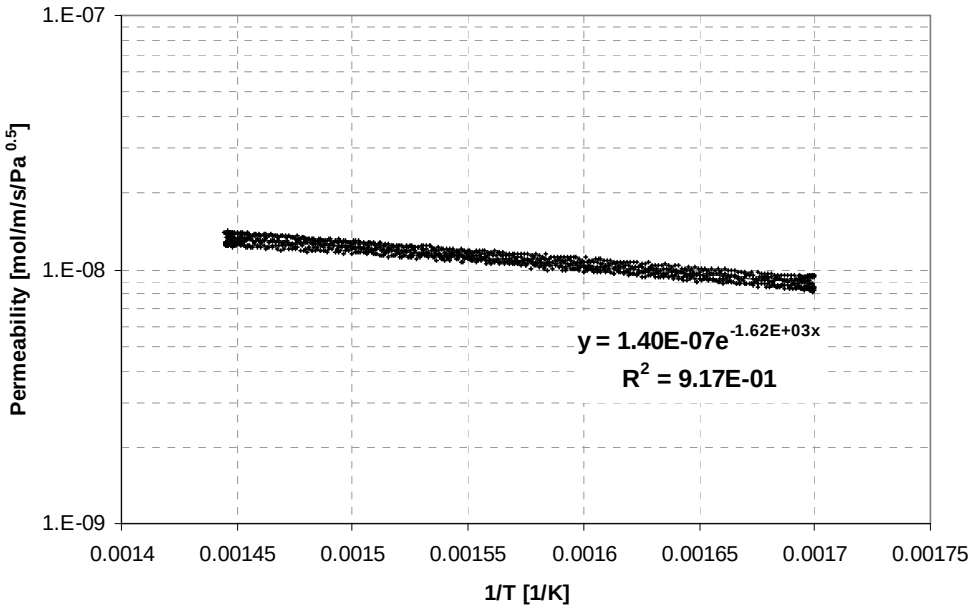

Figure 5.2: Permeability results for measurements on the 54μm thick Pd foil from Figure 5.1. Regression results are shown indicating the best-fit values for permeability pre-exponential factor and activation energy.

Table 6: Comparison of the measured hydrogen permeability through the 54μm thick Pd foil with values from the literature.

Author	Pre-exponential Factor (mol/m/s/Pa$^{0.5}$)	Activation Energy (kJ/mol)	Reference
Balovnev	2.34e-7	15.5	[135]
Holleck	1.49e-7	13.6	[37]
Howard	1.01e-7	13.0	[136]
Koffler	2.00e-7	15.7	[137]
Morreale	1.75e-7	13.8	[138]
This Work	1.40e-7	13.5	-

5.2 High Temperature Characterization of Microfabricated Membranes

Having verified the experimental approach using the bulk Pd foil, characterization of the microfabricated Pd-Ag alloy membranes could proceed. Membranes with a thickness of 0.6μm, 1.0μm, and 2.2μm have been tested. Each membrane was initially heated to 450 °C and held until the hydrogen permeation rate was stabilized. The dynamic features of the transient increase in hydrogen permeation during this holding

period (termed here as membrane “activation”) will be discussed in section 5.5. Once stabilized, the temperature was held at 450 °C while the hydrogen permeation rate was measured for five different hydrogen partial pressure set-points at the upstream channel inlet: 36.4 kPa, 27.3 kPa, 18.2 kPa, 9.1 kPa, and 4.5 kPa. At each pressure, the hydrogen permeation rate was measured for at least 15 minutes, sampling the permeate stream every 15 seconds, and these values were averaged to calculate the permeation rate. After taking measurements at all five pressures, the temperature was lowered and the experiment was repeated. The permeation measurements reported in this section have been taken between 250 °C and 450 °C. Figure 5.3 shows the permeance for each membrane thickness as a function of inverse temperature. The permeance is calculated by dividing the measured hydrogen flux by the square-root of the applied pressure difference and therefore describes the general permeation behavior for a membrane of a given thickness. Utilizing permeance values, an accurate comparison of the effects of membrane thickness on permeation behavior can be graphically visualized. For each set of data, the permeance trend line has been calculated by regression; the resulting lines from these regressions are shown in Figure 5.3. The effects of thickness on membrane performance are shown by plotting the pre-exponential factor for each of the lines in Figure 5.3 as a function of the membrane thickness for that set of data. The permeance pre-exponential factor allows all of the data for a membrane of a given thickness to be reduced to a single number for comparison with membranes of other thickness. This comparison is presented in Figure 5.4. The linearly increasing permeance with decreasing thickness confirms that hydrogen permeation is limited by the diffusion process for the entire range of temperature.

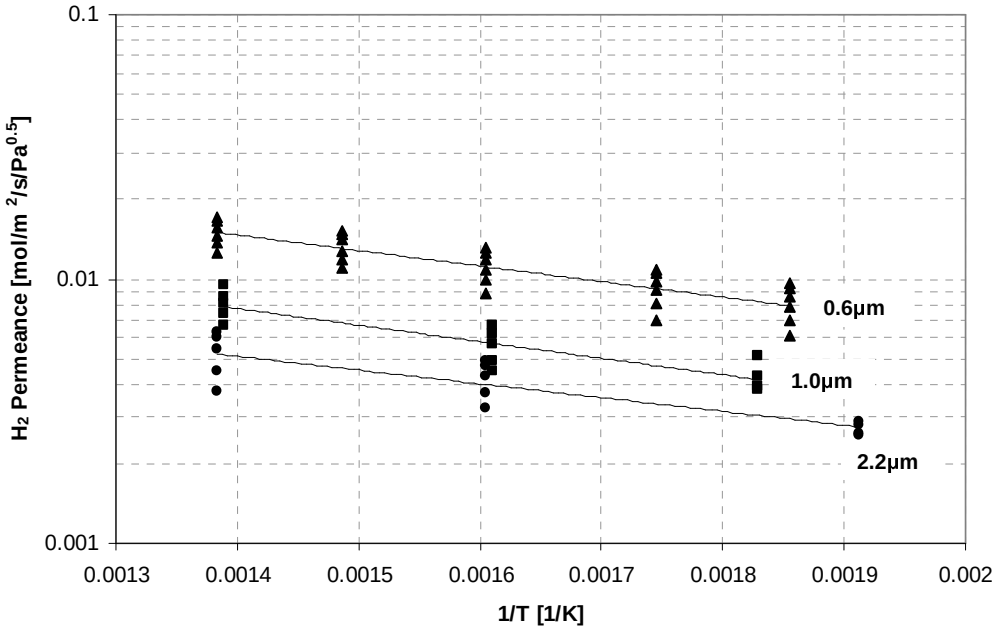

Figure 5.3: Measured hydrogen permeance values for microfabricated Pd-Ag alloy membranes of different thickness.

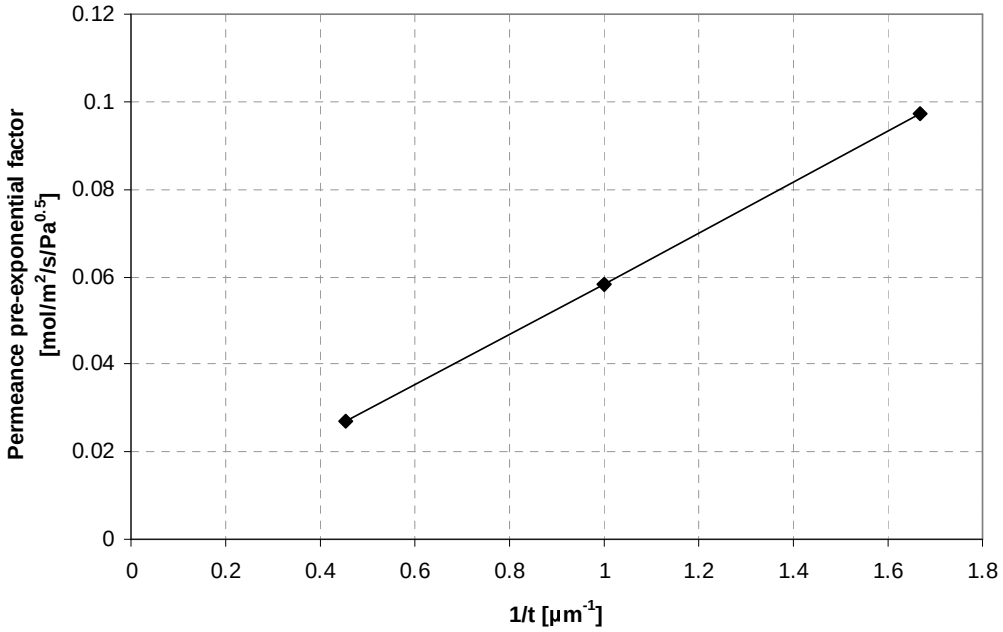

Figure 5.4: Effects of thickness on hydrogen permeation through microfabricated Pd-Ag alloy membranes.

Finally, each data point is multiplied by the membrane thickness to calculate the permeability. The averaged hydrogen permeability for the microfabricated $PdAg_{23}$ membranes in this work is then calculated by regression of these measurements as shown in Figure 5.5. The permeability coefficients based on our measurements compared to the diffusion-limited permeation parameters from the literature in Table 7. There is good agreement between these values, further confirming that the microfabricated membranes are diffusion-limited in the temperature and pressure range under investigation.

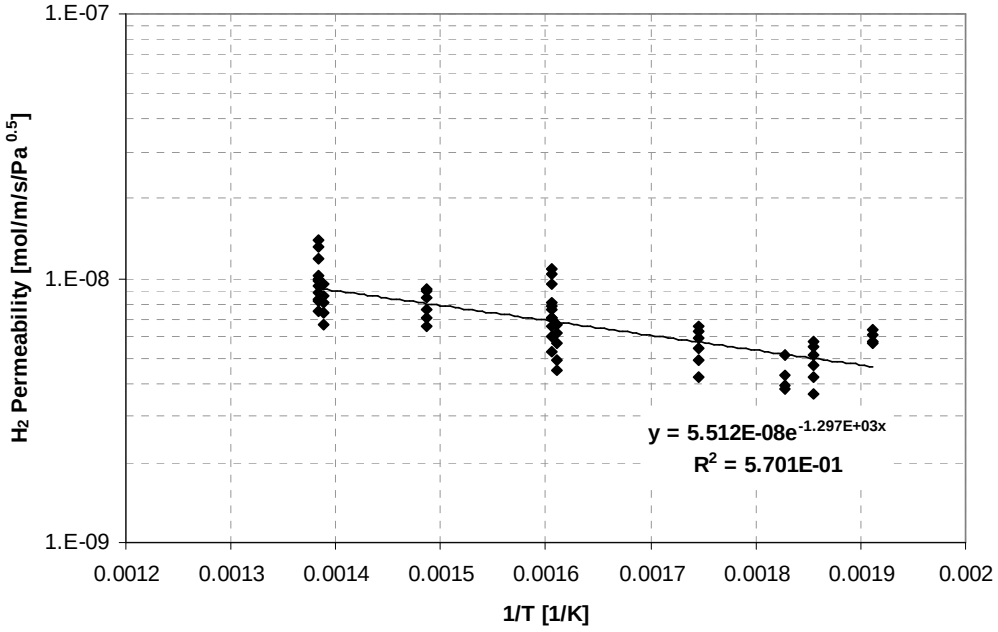

Figure 5.5: Permeability results for measurements on microfabricated membranes. Regression results are shown indicating the best-fit values for permeability equation.

Table 7: Comparison of the measured hydrogen permeability through the microfabricated $PdAg_{23}$ membranes with values for diffusion-limited, bulk $PdAg_{25}$ membranes from the literature.

Author	Pre-exponential Factor (mol/m/s/$Pa^{0.5}$)	Activation Energy (kJ/mol)	Reference
Ackerman	7.73e-8	6.60	[139, 140]
Chabot	4.95e-8	5.85	[34]
Holleck	9.90e-8	8.78	[37]
Nishikawa	16.6e-8	11.2	[141]
Serra	5.58e-8	6.30	[35]
Yoshida	3.85e-8	5.73	[123, 125]
This Work	5.51e-8	10.8	-

5.3 Low Temperature Characterization of Microfabricated Membranes

In order to search for a transition into desorption-limited behavior, the microfabricated membranes were also tested at temperatures below 250 °C. After high temperature testing (>250 °C), the membrane was held in a constant hydrogen pressure environment and the temperature was decreased at one degree per minute from 250 °C down to 150 °C. This experiment was repeated at several different pressure set-points. Representative curves, taken from the 1μm thick microfabricated membrane, are shown in Figure 5.6 alongside the literature data for thick $PdAg_{25}$ membranes. Upon cooling, the microfabricated membranes undergo a transition in activation energy which is identical to the transition reported in the literature for thick membranes, thus confirming that the microfabricated membranes are still limited by the diffusion process even at low operating temperature. For comparison of the magnitude of the measured H_2 flux, the values of Chabot should be used as the pressure difference in their study (14 kPa) is similar to the values used in our experiments. Our measured flux values at a hydrogen inlet pressure of 18.4 kPa are roughly 100 times larger than those of Chabot,

corresponding to a decrease in thickness by about two orders of magnitude between the two studies.

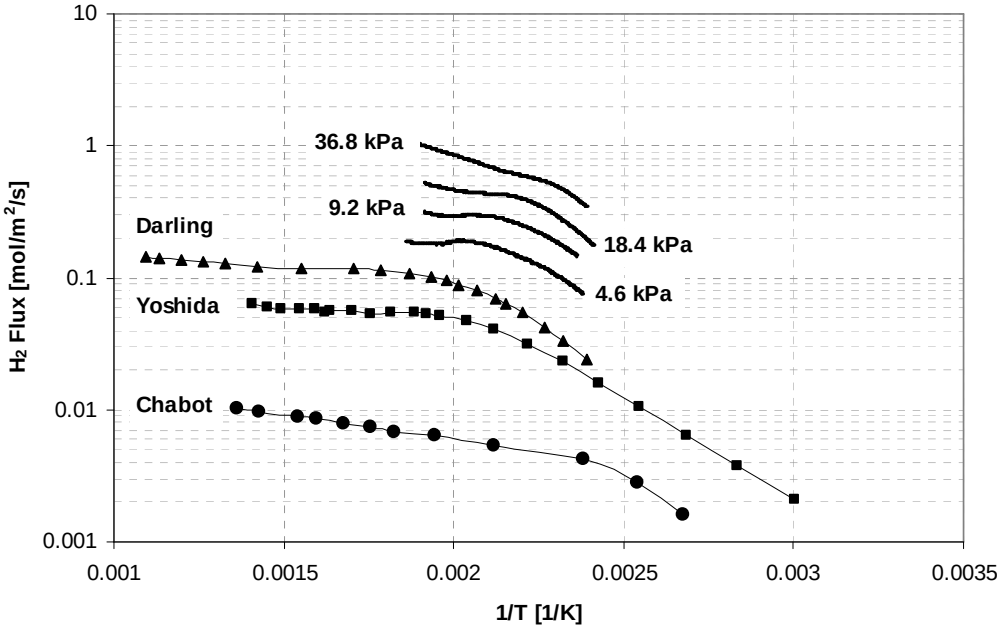

Figure 5.6: Low temperature hydrogen flux measurements taken on a microfabricated Pd-Ag alloy membrane of 1μm thickness. The literature data for thick $PdAg_{25}$ membranes is also shown for comparison [34, 124, 125].

5.4 Low Temperature Membrane Failure

Ideally, the low temperature measurements presented in section 5.3 would extend to even lower temperatures to search for the second activation energy transition indicating that the true desorption limit had been reached. Our early efforts to capture this behavior consistently resulted in membrane failure as the temperature was further reduced. Membrane failure was detected by seeing a sharp increase in the helium leak rate indicating that the membrane had ruptured. The measurements taken during one of these experiments are shown in Figure 5.7. After visual inspection of the ruptured membrane, the failure was attributed to brittle fracture of the topside SiO_2 support structure. An SEM image of the ruptured membrane is shown in Figure 5.8. The SiO_2

has cracked down the center of the area where the Si has been removed from the backside.

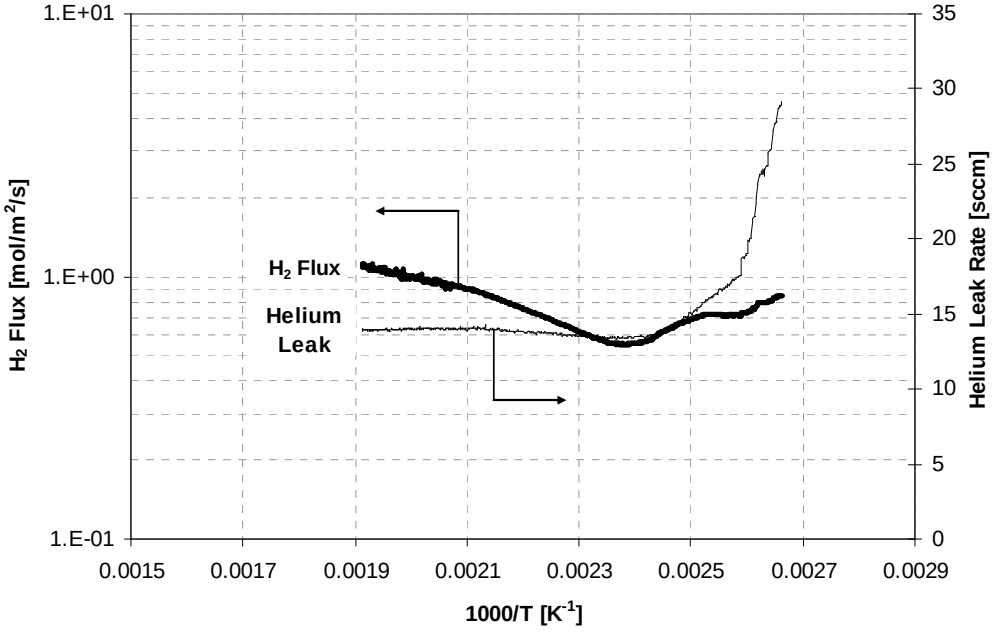

Figure 5.7: Low temperature permeation results showing membrane failure as the temperature is decreased below ~145 °C. Membrane failure is marked by a sharp increase in the helium leak rate through the membrane.

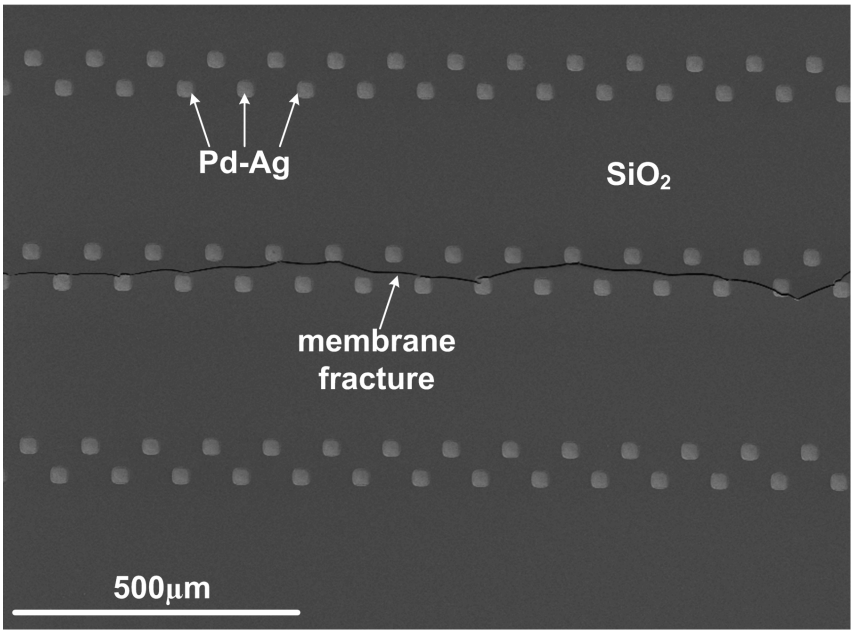

Figure 5.8: SEM image of the top surface of a cracked membrane taken after measuring hydrogen permeation rate at temperatures below 150 °C.

On every microfabricated membrane there are 480 separate windows etched through the Si to expose the metal surface. After cooling down below 150 °C there were typically anywhere from 5 to 20 individual windows that had fractured as shown in Figure 5.8.

Insight into this failure mode is enabled by interpretation of the permeation behavior in the context of the improved model. The transition in activation energy of permeation above 150 °C is caused by the electronic contribution to the excess potential, indicating that the absorbed hydrogen concentration is high. Hydrogen absorption causes a volumetric expansion of the metal film lattice. As the film is cooled below 150 °C the physical expansion of the membrane induced by hydrogen absorption causes the free-standing composite PdAg-SiO_2 structure to bow away from the edges which are constrained by the underlying Si. The out-of-plane bending, and resulting tensile stress on the top surface of the SiO_2 layer, results in brittle fracture of the membrane. This failure mode has important ramifications for future work on Pd-based alloy membranes.

It might be argued that the observed failure could be caused by hydrogen embrittlement of a Pd-rich region in the Pd-Ag membrane. These regions could result from micro-alloying during the deposition process or could be the product of diffusion of the metal atoms during testing. Due to the larger size of the Ag atom it is expected that some segregation towards the membrane surface and into grain boundaries will occur. However, the observed failure behavior can be attributed to brittle fracture of the topside SiO_2 support as opposed to an embrittlement failure of the underlying Pd-Ag layer based on the macroscopic nature of the failure. Under the temperatures used in this work, the diffusion velocity for substitutional diffusion of Ag in Pd is on the order of 1nm per week (conservatively estimating the diffusion coefficient as 10^{-24} m^2/s) [81]. Therefore it is

impossible for any large-scale variations of the film composition to occur which can be responsible for failure along the entire length of the 3.5mm windows. If this failure was caused by embrittlement of a locally Pd-rich region in the membrane it is expected that these regions would be highly localized (much smaller than the 25μm square features in the topside SiO_2) and uniformly distributed over the entire membrane surface. Since the observed failure is macroscopic and there are only a few discrete fractures rather than a uniform distribution, this failure can be attributed to brittle fracture of the SiO_2 structure upon expansion of the underlying Pd-Ag layer due to absorption of hydrogen.

For high temperature applications, the need to closely match the coefficients of thermal expansion of membrane materials is an obvious consideration. These results indicate that low temperature operation has a similar problem, but there is no readily available solution. It is unlikely that any substrate will exhibit exactly the same volumetric dependence on hydrogen pressure as the Pd-alloy film and therefore hydrogen absorption will always lead to structural mismatch. For a rigid substrate, the volumetric expansion of the Pd-alloy film will lead to large interfacial stress and likely result in adhesion problems and, ultimately, delamination. This problem may be addressed by the use of a flexible substrate. If the substrate can deform to accommodate the expansion of the metal film without failing then low temperature operation may be sustainable. In addition to mechanical flexibility, this substrate material will need to be porous, chemically inert, packageable without leaks, and able to withstand a reasonable pressure difference. This represents a significant area of research for the future of Pd-based alloy membranes.

5.5 Membrane H_2-He Selectivity Decay After Extended Testing

In addition to the abrupt fracture which occurs when the temperature was decreased below 150 °C, another failure mechanism was observed. Several membranes were kept at elevated temperature (>200 °C) and tested intermittently over a period of several weeks. Performance was consistent for the first few weeks, but after testing for 4-5 weeks the membrane selectivity would deteriorate over the span of a few days. The membranes were then removed from the fixture and inspected. An SEM image of the top membrane surface after extended testing is shown in Figure 5.9. Numerous pin-holes have formed in the metal leading to the increased helium leak rate.

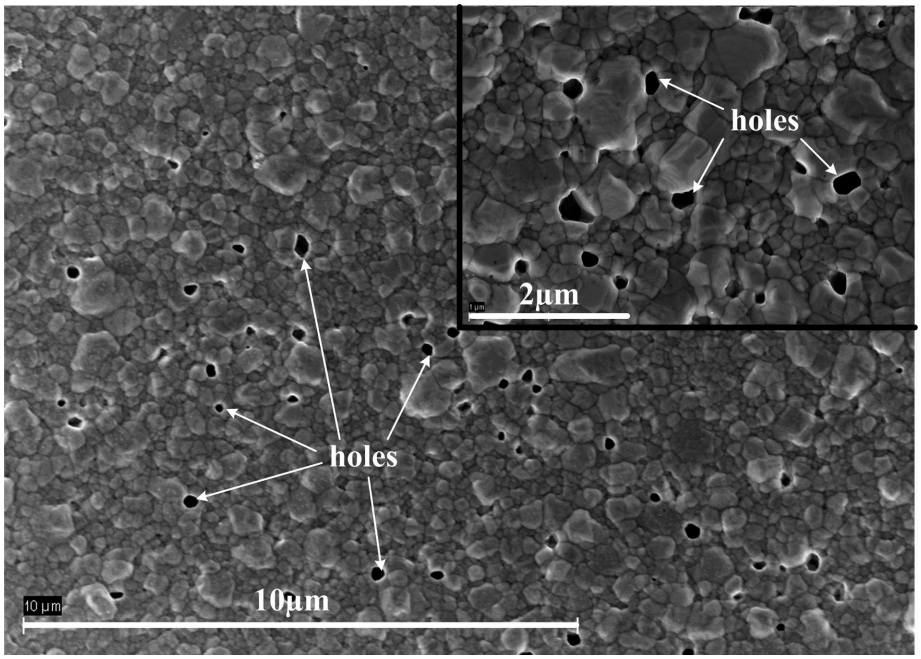

Figure 5.9: Membrane surface after testing over a period of 4-5 weeks. Numerous pin-holes are shown which cause a decrease in membrane selectivity (Inset at higher magnification).

The formation of pin-holes after an extended period of time at elevated temperature is due to structural relaxation of the internal stress in the film. Although no rigorous characterization was performed, the stress in the sputter-deposited Pd-Ag film was found to be tensile by measuring the curvature of the Si wafer both before and after

deposition. The formation of voids in the free-standing membrane reduces the internal stress in the metal lattice and is therefore a result of the system approaching thermodynamic equilibrium. As such, nothing can be done to stop the formation of voids in a tensile film.

In practical applications this failure mode should be easily avoided by ensuring that the as-deposited metal layer is compressive rather than tensile. The internal stress of a sputter-deposited metal film can be controlled by adjusting the gas pressure during deposition. Switching from tensile to compressive stress can be accomplished by increasing sputtering gas pressure [142].

5.5 Influence of Microstructure on Hydrogen Permeation

During testing, each membrane initially exhibits low hydrogen permeation rates. After ~2 hours at 450 °C the permeation rate has increased from 0.25 mol/m^2/s to almost 1 mol/m^2/s, as shown in Figure 5.10. Subsequent experiments on the same membrane did not exhibit this transient response indicating an irreversible change has occurred during initial testing. Due to the time span over which the performance enhancement occurs, the thermally activated nature, and the asymptotic approach towards a maximum value, it was postulated that this increase could be related to the evolving microstructure of the metal film upon exposure to elevated temperature.

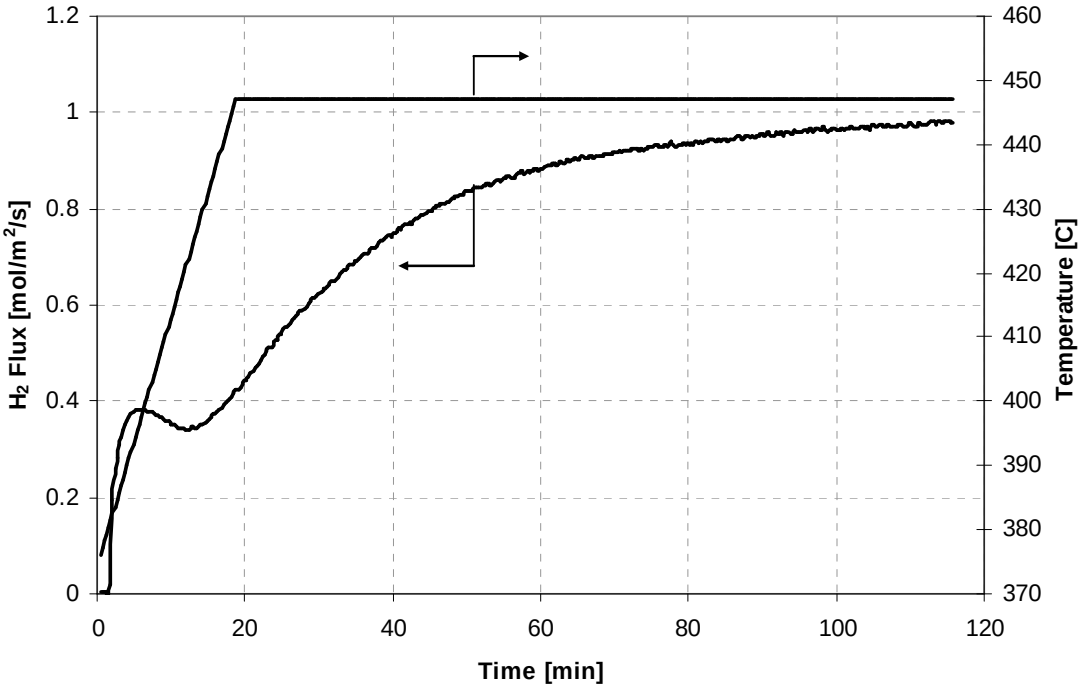

Figure 5.10: Transient response during initial testing of a fresh membrane with a thickness of 1μm and an upstream inlet pressure of 36.8 kPa. Arrows indicate appropriate axes.

To verify this hypothesis the membrane microstructure was characterized using scanning electron microscopy (SEM). The morphology of the as-deposited membrane is well described by the structure zone models (SZMs) developed to categorize structural evolution of thin films during physical vapor deposition (PVD) [143-145]. The SZMs represent the PVD process by recognizing that the critical parameters affecting film microstructure are bulk metal atom diffusion within the film and surface diffusion on the free surface where deposition occurs. In the case of a magnetron sputtered film, the appropriate metrics for these phenomena are the sputtering gas pressure and the reduced temperature (T_s/T_m), defined as the ratio of the substrate temperature during deposition (T_s) to the melting temperature of the deposited material (T_m). Reduced temperature captures the effects of bulk self-diffusion and grain boundary motion, while gas pressure

in the sputtering chamber has been shown to be the primary factor affecting adatom energy at the film surface via gas phase collisions prior to arrival. The adatom energy level effectively determines how far the adatom will diffuse along the surface prior to being incorporated into the film. Near the substrate the grain structure is nearly amorphous due to the limited surface mobility attributed to the Ti adhesion layer. As film thickness grows, two factors allow the grain structure to coarsen. The adatom surface mobility increases as the free surface moves away from the Ti sublayer and the surface temperature drastically increases as a result of the energetic bombardment by the Pd-Ag vapor molecules [146]. The resulting morphology is the dense columnar film with increasing grain size in the thickness direction. As Figure 5.11 shows, simply releasing the film at ambient temperature does not provide adequate energy for grain coarsening near the previously constrained surface. Only after elevating the temperature during annealing can the microstructure relax and minimize surface energy associated with both grain boundaries and the free surface area by grain coalescence.

Since the grain size is much smaller on the constrained surface (bottom) of the deposited film a characterization procedure needed be developed to enable inspection of both the top and bottom surfaces after a specified annealing treatment. A method was developed whereby a test-film was deposited onto a Si wafer under identical conditions as in actual membrane fabrication. Upon dicing the Si wafer, the tensile stress in the film allowed small pieces to be grasped along the diced edges and peeled from the substrate. These samples allowed imaging of both the top and bottom surface of the metal film. The SEM images of the as-deposited film are shown in Figure 5.11(a-b). The as-

deposited constrained surface exhibits no clear structure while the free-surface has well-defined grains.

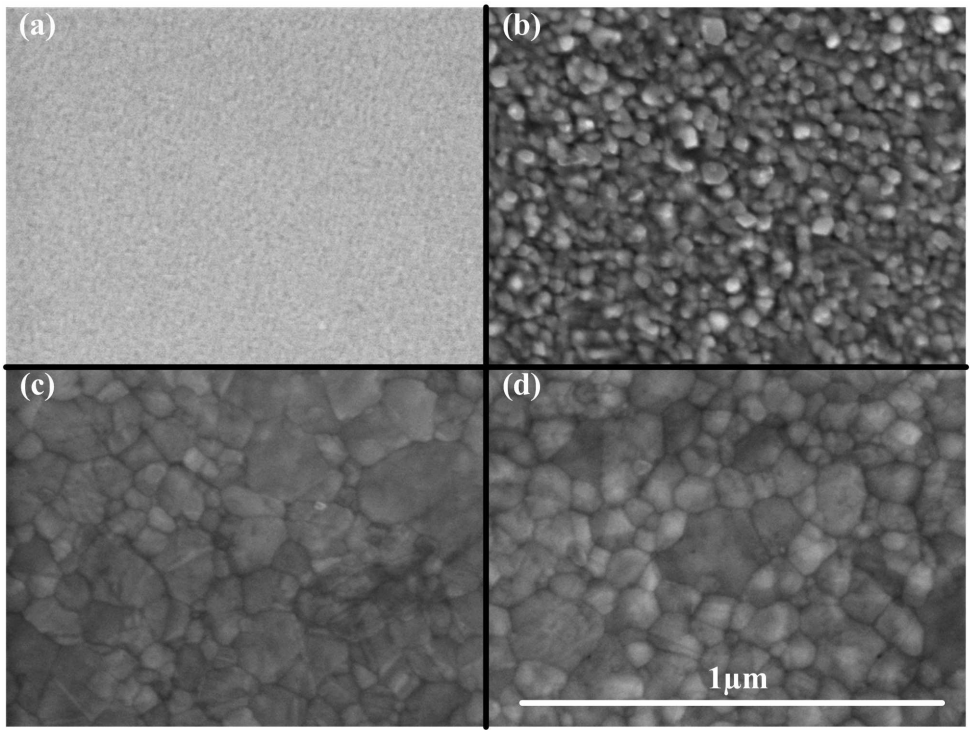

Figure 5.11: SEM images of (a) As-deposited, constrained surface (bottom), (b) As-deposited, free surface (top), (c) 45 minute anneal at 450 °C, constrained surface, and (d) 45 minute anneal at 450 °C, free surface.

The samples were subjected to a controlled annealing process and then inspected to determine the average grain size as a function of annealing treatment. Grain size was estimated using the linear intercept method where a line of known length is superimposed on the image and the number of grain boundary intersections is counted. Dividing the length of the line by the number of intersections gives an average grain size. To ensure accurate representation of the sample the intercept method is repeated with the line oriented at 0, 45, 90, and 135 degrees. The number of intersections counted varied between 110 and 450 depending on the sample; samples with larger grain size exhibited more variability in size and required averaging over a larger number of grains to calculate

and accurate average size. The annealing was done in an inert argon environment while the temperature was below 175 °C and switched to a hydrogen environment above this temperature. The annealing ramp rate while increasing temperature was ~40 °C per minute and decreasing temperature was ~15 °C per minute and limited by the natural cooling rate of the annealing fixture. In addition to a prescribed holding time at 450 °C, the initial microstructure evolution was captured by heating to 250, 350, and 450 °C and then immediately cooling without holding at high temperature. The results of this annealing study are summarized in Figure 5.12. These results are superimposed on the transient increase in hydrogen flux in Figure 5.13. There is a clear correlation between grain growth and the increase in permeation rate exhibited by the microfabricated membranes.

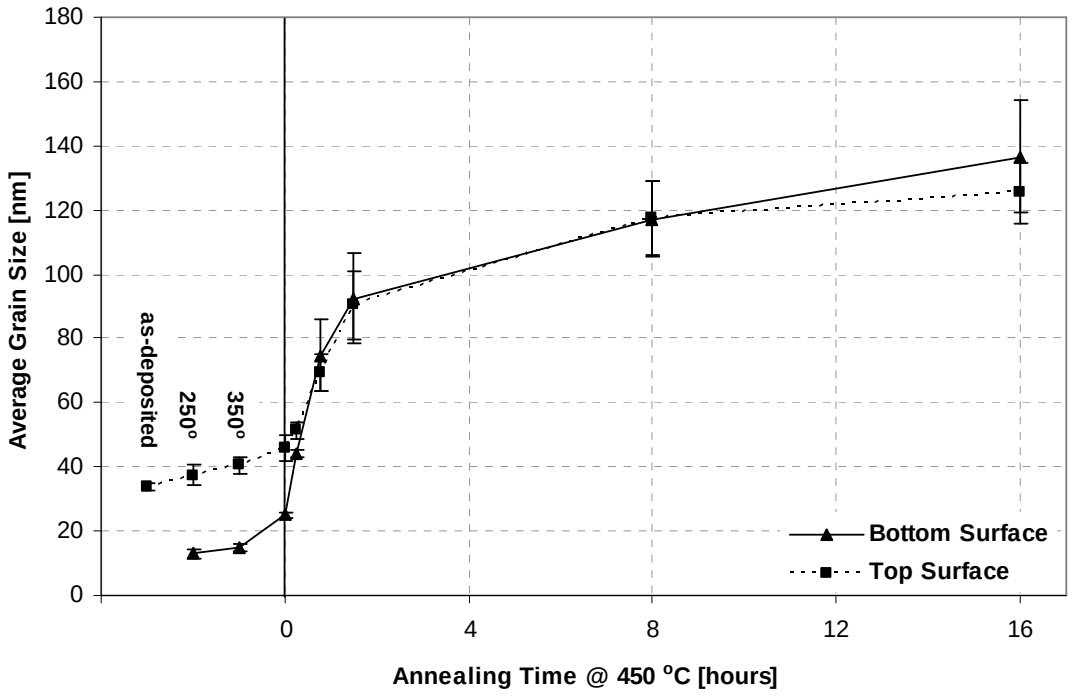

Figure 5.12: Average grain size in the Pd-Ag alloy membrane as a function of annealing time at 450 C. The grains were too small to measure in the as-deposited state on the bottom surface. Error bars are one standard deviation for the average size calculated from differenct intercept lines.

This result can be interpreted as a result of the trapping behavior of hydrogen in grain boundaries. Due to a distribution of site energies in the grain boundary, the diffusion coefficient in the boundary is highly dependent on hydrogen concentration. At low concentration only the low-energy sites are occupied and diffusion must proceed by jumping up into sites of higher energy resulting in a decrease in the diffusion coefficient. At higher concentrations the low-energy sites become full and diffusion occurs as jumping between high energy sites with little required activation energy resulting in fast diffusion along the grain boundaries [147, 148]. The situation is complicated by the solubility behavior in grain boundaries. The larger free volume within the boundary as compared to the metal lattice enhances hydrogen solubility. It is suspected that the initial peak in the hydrogen flux (at ~6 minutes and 398 °C in Figure 5.10) is due to a reduction in the hydrogen concentration in the grain boundaries as the temperature is increased. Above ~400 °C only the low energy sites are occupied and therefore the grain boundaries act as traps that the hydrogen must circumvent to traverse the membrane. As the grain structure coarsens through annealing the trapping effect is reduced and the permeation rate increases.

From a practical standpoint there are two useful conclusions that can be drawn from these results. First, for a sputter-deposited Pd-Ag alloy film, the majority of the grain growth is confined to a period of roughly two hours if annealed at 450 °C, defining the necessary annealing time to yield repeatable results. Second, due to the agreement between our permeation results and those available in the literature, it can be concluded that for an average grain size above ~120nm, grain boundaries have very little effect on the hydrogen permeability above 150 °C.

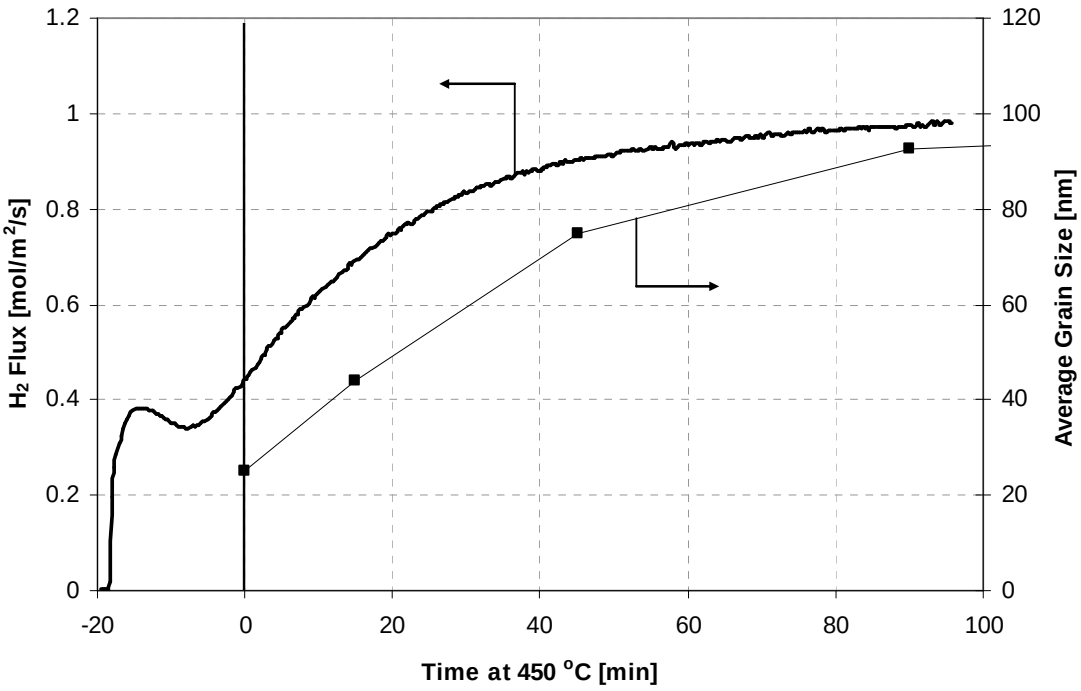

Figure 5.13: Comparison of grain growth with transient hydrogen permeation results.

The effects of grain boundaries on the hydrogen permeation rate in this system need further characterization. The interplay between increased solubility and decreased diffusion coefficient in boundaries at elevated temperature needs clarification. The possibility of utilizing grain boundaries as fast diffusion pathways at low temperatures represents a useful extension to this work and could potentially increase the hydrogen permeation rate provided that structural failure at low temperature can be avoided.

CHAPTER 6
CONCLUSIONS AND RECOMMENDATIONS

6.1 Conclusions

There are two main thrusts in this body of work, one is of a fundamental nature and the other is directed towards practical applications. A theoretical model for hydrogen permeation has been developed based on first-principles and was validated using literature data as well as careful experimental characterization of thin, free-standing Pd-Ag alloy (23% weight Ag) membranes. This thesis research yields the following conclusions:

- Diffusion-limited hydrogen permeation through Pd-Ag alloy membranes has been shown to undergo a transition in activation energy from a value of ~5-10 kJ/mol to a value of ~30 kJ/mol at temperatures below ~200 °C, which is caused by the non-ideal absorption (solubility) behavior in the metal lattice. Currently available models do not account for the non-ideal behavior and therefore cannot predict this transition. The improved model developed in this work predicts this transition and provides theoretical insight into its physical origin.
- Hydrogen permeation through Pd-Ag alloy membranes has been shown to be limited by the diffusion process even at a thickness down to 600 nanometers and temperatures above 150 °C.
- Operation of microfabricated free-standing Pd-Ag membranes at temperatures below 150 °C leads to brittle failure of the SiO_2 support structure utilized in this work due to expansion of the Pd-alloy film upon increasing hydrogen absorption.

- The tensile stress in the sputter-deposited Pd-Ag alloy films leads to degradation of the H_2/He selectivity of the fabricated membranes after extended testing due to formation of pin-holes through the metal layer.
- Annealing of the sputter-deposited metal film results in grain growth from an average size of ~30 nanometers to ~140 nanometers after 16 hours at a temperature of 450 °C in a H_2 environment.
- An increase in average grain size to ~95 nm in the first two hours of high temperature operation causes a fourfold increase in the hydrogen permeation due to a reduction in the number of grain boundaries which act as hydrogen 'traps' in the membrane and slow permeation.
- Above an average grain size of ~140 nm the grain boundaries have little effect on the hydrogen permeation rate under the temperatures and pressures studied in this work.

6.2 Recommendations

There are several areas where additional research would be a natural extension of this thesis and provide valuable insight. The recommendations for future work include:

- Refining of the regression constants in the improved model based on a more complete data set to improve the predictive capabilities of the model, including application of the permeation model developed to other metal-hydrogen systems.
- Careful control over the stress levels in the SiO_2 support structure or development of more flexible support structures for microfabricated Pd-alloy membranes to enable testing at temperatures below 150 °C.

- Extension of the present work to compressive Pd-alloy films to ensure long-term stability by avoiding formation of pin-holes, including investigation of the effects of thin-film stress on hydrogen solubility and specifically how the stress level affects the non-ideal solution behavior and change in activation energy at low temperature.
- More rigorous characterization of the effects of grain size on the hydrogen solubility and diffusion coefficient, including first principle DFT calculations, investigation of the possibility of utilizing grain boundary diffusion at low temperatures to enhance hydrogen permeation rate, and the effects of segregation of impurities into grain boundaries on grain boundary diffusion.
- Investigation of the permeation properties of thin Pd-alloy films in the presence of contaminating gas species (H_2O, CO_2, CO, H_2S, etc.) which is of key importance to a number of practical applications.

REFERENCES

[1] M. P. Ramage, et al., The Hydrogen Economy: Opportunities, Costs, Barriers and R&D Needs, The National Academy Press, Washington, DC, 2004.

[2] D. Hart, P. Freud, and A. Smith, *Hydrogen Today and Tomorrow*, International Energy Agency Greenhouse Gas Programme (IEA GHG), 1999.

[3] J. Ogden, *Hydrogen Applications: Industrial Uses and Stationary Power*, Institute of Transportation Studies, University of California, Davis, http://www.its.ucdavis.edu/education/classes/pathwaysclass/7-StationaryH2(Ogden).pdf, 2004.

[4] N. W. Ockwig and T. M. Nenoff, Membranes for hydrogen separation, Chemical Reviews 107 (2007) 4078.

[5] J. G. Stichlmair and J. R. Fair, Distillation: Principles and Practice, Wiley-VCH, New York, 1998.

[6] F. G. Kerry, Industrial Gas Handbook: Gas Separation and Purification, CRC Press, Boca Raton, 2007.

[7] J. A. Ritter and A. D. Ebner, State-of-the-art adsorption and membrane separation processes for hydrogen production in the chemical and petrochemical industries, Separation Science and Technology 42 (2007) 1123.

[8] S. Sircar and T. C. Golden, Purification of hydrogen by pressure swing adsorption, Separation Science and Technology 35 (2000) 667.

[9] R. W. Spillman, Economics of Gas Separation Membranes, Chemical Engineering Progress 85 (1989) 41.

[10] S. Sircar, Pressure swing adsorption, Ind. Eng. Chem. Res. 41 (2002) 1389.

[11] J. Stocker, M. Whysall, and G. Q. Miller, *30 Years of PSA Technology for Hydrogen Separation*, UOP LLC, 1998.

[12] A. B. Hinchliffe and K. E. Porter, A comparison of membrane separation and distillation, Chemical Engineering Research & Design 78 (2000) 255.

[13] W. K. Ng, K. Kolmetz, and S. H. Lee, Energy Optimization of Cryogenic Distillation, Distillation 2005 (2005)

[14] K. E. Porter, A. B. Hinchliffe, and B. J. Tighe, Gas separation using membranes .2. Developing a new membrane for the separation of hydrogen and carbon monoxide using the targeting approach, Ind. Eng. Chem. Res. 36 (1997) 830.

[15] Palladium Alloy Diffusion Process for Hydrogen Purification: First commecial-scale plant in operation, Plat. Met. Rev. 6 (1962) 47.

[16] R. J. Gardner, R. A. Crane, and J. F. Hannan, Hollow Fiber Permeater for Separating Gases, Chemical Engineering Progress 73 (1977) 76.

[17] W. J. Schell and C. D. Houston, Spiral-Wound Permeators for Purification and Recovery, Chemical Engineering Progress 78 (1982) 33.

[18] W. J. Koros and G. K. Fleming, Membrane-Based Gas Separation, J. Membr. Sci. 83 (1993) 1.

[19] W. S. W. Ho and K. K. Sirkar, Membrane Handbook, Chapman & Hall, New York, 1992.

[20] S. A. Stern and S. Trohalaki, Fundamentals of Gas-Diffusion in Rubbery and Glassy-Polymers, Acs Symposium Series 423 (1990) 22.

[21] B. D. Freeman, Basis of permeability/selectivity tradeoff relations in polymeric gas separation membranes, Macromolecules 32 (1999) 375.

[22] B. Freeman and I. Pinnau, Separation of gases using solubility-selective polymers, Trends in Polymer Science 5 (1997) 167.

[23] L. M. Robeson, Correlation of Separation Factor Versus Permeability for Polymeric Membranes, J. Membr. Sci. 62 (1991) 165.

[24] L. M. Robeson, The upper bound revisited, J. Membr. Sci. 320 (2008) 390.

[25] H. Verweij, Y. S. Lin, and J. H. Dong, Microporous silica and zeolite membranes for hydrogen purification, Mrs Bulletin 31 (2006) 756.

[26] H. Verweij, Ceramic membranes: Morphology and transport, J. Mater. Sci. 38 (2003) 4677.

[27] S. C. A. Kluiters, *Status review on membrane systems for hydrogen separation*, Energy Center of The Netherlands, 2004.

[28] S. Adhikari and S. Fernando, Hydrogen membrane separation techniques, Ind. Eng. Chem. Res. 45 (2006) 875.

[29] R. M. de Vos and H. Verweij, High-selectivity, high-flux silica membranes for gas separation, Science 279 (1998) 1710.

[30] T. Norby, Solid-state protonic conductors: principles, properties, progress and prospects, Solid State Ionics 125 (1999) 1.

[31] J. Guan, et al., Transport properties of BaCe0.95Y0.05O3-alpha mixed conductors for hydrogen separation, Solid State Ionics 100 (1997) 45.

[32] J. Guan, et al., Transport properties of SrCe0.95Y0.05O3-delta and its application for hydrogen separation, Solid State Ionics 110 (1998) 303.

[33] S. M. Saufi and A. F. Ismail, Fabrication of carbon membranes for gas separation - a review, Carbon 42 (2004) 241.

[34] J. Chabot, et al., Fuel Cleanup System - Poisoning of Palladium-Silver Membranes by Gaseous Impurities, Fusion Technology 14 (1988) 614.

[35] E. Serra, et al., Hydrogen and deuterium in Pd-25 pct Ag alloy: Permeation, diffusion, solubilization, and surface reaction, Metallurgical and Materials Transactions a-Physical Metallurgy and Materials Science 29 (1998) 1023.

[36] S. N. Paglieri and J. D. Way, Innovations in palladium membrane research, Sep. & Pur. Methods 31 (2002) 1.

[37] G. L. Holleck, Diffusion and Solubility of Hydrogen in Palladium and Palladium-Silver Alloys, J. Phys. Chem. 74 (1970) 503.

[38] S. Uemiya, State-of-the-art of supported metal membranes for gas separation, Sep. & Pur. Methods 28 (1999) 51.

[39] T. Pietrass, Carbon-based membranes, Mrs Bulletin 31 (2006) 765.

[40] M. B. Rao and S. Sircar, Performance and pore characterization of nanoporous carbon membranes for gas separation, J. Membr. Sci. 110 (1996) 109.

[41] M. B. Rao and S. Sircar, Nanoporous Carbon Membranes for Separation of Gas-Mixtures by Selective Surface Flow, J. Membr. Sci. 85 (1993) 253.

[42] S. Sircar, M. B. Rao, and C. M. A. Thaeron, Selective surface flow membrane for gas separation, Separation Science and Technology 34 (1999) 2081.

[43] L. J. Wang and F. C. N. Hong, Effects of surface treatments and annealincy on carbon-based molecular sieve membranes for gas separation, Appl. Surf. Sci. 240 (2005) 161.

[44] T. Graham, On the absorption and dialytic separation of gases by colloid septa, Phil. Trans. Roy. Soc. Lond. 156 (1866) 399.

[45] J. B. Hunter, A New Hydrogen Purification Process, Plat. Met. Rev. 4 (1960) 130.

[46] W. J. Koros and R. Mahajan, Pushing the limits on possibilities for large scale gas separation: which strategies?, J. Membr. Sci. 175 (2000) 181.

[47] R. Baker, Membrane Technology and Applications, John Wiley and Sons, New Jersey, 2004.

[48] H. Sakaguchi, et al., Hydrogen Separation Using Lani5 Films, J. Less-Common Met. 126 (1986) 83.

[49] G. Y. Adachi, H. Nagai, and J. Shiokawa, Lani5 Film for Hydrogen Separation, J. Less-Common Met. 97 (1984) L9.

[50] S. Uemiya, T. Matsuda, and E. Kikuchi, Hydrogen Permeable Palladium Silver Alloy Membrane Supported on Porous Ceramics, J. Membr. Sci. 56 (1991) 315.

[51] S. Uemiya, et al., A Palladium Porous-Glass Composite Membrane for Hydrogen Separation, Chemistry Letters (1988) 1687.

[52] S. Uemiya, et al., Preparation of Thin Palladium Films by Use of an Electroless Plating Technique, Nippon Kagaku Kaishi (1990) 669.

[53] S. Uemiya, et al., Separation of Hydrogen through Palladium Thin-Film Supported on a Porous-Glass Tube, J. Membr. Sci. 56 (1991) 303.

[54] J. Shu, et al., Structurally stable composite Pd-Ag alloy membranes: Introduction of a diffusion barrier, Thin Solid Films 286 (1996) 72.

[55] T. L. Ward and T. Dao, Model of hydrogen permeation behavior in palladium membranes, J. Membr. Sci. 153 (1996) 211.

[56] S. V. Karnik, M. K. Hatalis, and M. V. Kothare, Towards a palladium micro-membrane for the water gas shift reaction: Microfabrication approach and hydrogen purification results, J. Microelectromech. Sys. 12 (2003) 93.

[57] F. C. Gielens, et al., Microsystem technology for high-flux hydrogen separation membranes, J. Membr. Sci. 243 (2004) 203.

[58] B. A. Wilhite, M. A. Schmidt, and K. F. Jensen, Palladium-based micromembranes for hydrogen separation: Device performance and chemical stability, Ind. Eng. Chem. Res. 43 (2004) 7083.

[59] Y. Zhang, et al., Hydrogen permeation characteristics of thin Pd membrane prepared by microfabrication technology, J. Membr. Sci. 277 (2006) 203.

[60] J. T. F. Keurentjes, et al., High-flux palladium membranes based on microsystem technology, Ind. Eng. Chem. Res. 43 (2004) 4768.

[61] H. D. Tong, et al., Microsieve supporting palladium-silver alloy membrane and application to hydrogen separation, J. Microelectromech. Sys. 14 (2005) 113.

[62] H. S. C. Deville and L. Troost, C. r. hebd Seanc. Acad. Sci. 57 (1863) 965.

[63] F. A. Lewis, The Palladium/Hydrogen System, Academic Press Inc., New York, 1967.

[64] G. Alefeld and J. Volkl, eds., Hydrogen in Metals I, Topics in Applied Physics, Vol. 28, Springer-Verlag, Berlin, 1978.

[65] G. Alefeld and J. Volkl, eds., Hydrogen in Metals II, Topics in Applied Physics, Vol. 29, Springer-Verlag, Berlin, 1978.

[66] H. Wipf, ed., Hydrogen in Metals III, Topics in Applied Physics, Vol. 73, Springer, Berlin, 1997.

[67] Y. Fukai, The Metal-Hydrogen System, Springer, New York, 2005.

[68] W. M. Mueller, J. P. Blackledge, and G. Libowitz, G., Metal Hydrides, Academic Press, Inc., New York, 1968.

[69] M. Fullenwider, Hydrogen Entry and Action in Metals, Pergamon Press, Inc., New York, 1983.

[70] M. Sastri, B. Viswanathan, and S. Murthy, Metal Hydrides: Fundamentals and Applications, Springer-Verlag, New York, 1998.

[71] A. Sieverts, palladium and hydrogen, Zeitschrift Fur Physikalische Chemie--Stochiometrie Und Verwandtschaftslehre 88 (1914) 103.

[72] A. Sieverts, Palladium and hydrogen. II., Zeitschrift Fur Physikalische Chemie--Stochiometrie Und Verwandtschaftslehre 88 (1914) 451.

[73] A. Sieverts and W. Krumbhaar, Solubility of gases in metals and alloys., Berichte Der Deutschen Chemischen Gesellschaft 43 (1910) 893.

[74] H. Pfeiffer and H. Peisl, Lattice Expansion of Niobium and Tantalum Due to Dissolved Hydrogen and Deuterium, Phys. Lett. A 60 (1977) 363.

[75] G. G. Libowitz, The Solid State Chemistry of Binary Metal Hydrides, W. A. Benjamin, Inc., New York, 1965.

[76] A. Sieverts and A. Gotta, About the properties of several metal hydrides, Zeitschrift Fur Anorganische Und Allgemeine Chemie 172 (1928) 1.

[77] A. Sieverts and A. Gotta, Regarding the characteristics of some metal hydrogens II, Zeitschrift Fur Anorganische Und Allgemeine Chemie 187 (1930) 155.

[78] D. P. Smith, Hydrogen in Metals, University of Chicago Press, Chicago, 1948.

[79] G. Borelius, Solubility and diffusion of hydrogen in metals, Annalen Der Physik 83 (1927) 0121.

[80] A. L. Hines and R. N. Maddox, Mass Transfer: Fundamentals and Applications, Prentice Hall, New Jersey, 1985.

[81] H. Mehrer, Diffusion in Solids, Springer, New York, 2007.

[82] S. A. Steward, *Lawrence Livermore National Laboratory Report, UCRL-53441 DE84 007362*, 1983.

[83] K. S. Rothenberger, et al., Evaluation of tantalum-based materials for hydrogen separation at elevated temperatures and pressures, J. Membr. Sci. 218 (2003) 19.

[84] J. E. Lennard-Jones, Processes of adsorption and diffusion on solid surfaces., Transactions of the Faraday Society 28 (1932) 0333.

[85] D. O. Hayward and B. M. Trapnell, Chemisorption, Butterworth and Co. Ltd., London, 1964.

[86] N. Boes and H. Zuchner, Diffusion of Hydrogen and Deuterium in Ta, Nb, and V, Physica Status Solidi a-Applied Research 17 (1973) K111.

[87] R. E. Buxbaum and A. B. Kinney, Hydrogen transport through tubular membranes of palladium-coated tantalum and niobium, Ind. Eng. Chem. Res. 35 (1996) 530.

[88] D. J. Edlund and J. Mccarthy, The Relationship between Intermetallic Diffusion and Flux Decline in Composite-Metal Membranes - Implications for Achieving Long Membrane Lifetime, J. Membr. Sci. 107 (1995) 147.

[89] D. Edlund, et al., Hydrogen-Permeable Metal Membranes for High-Temperature Gas Separations, Gas Separation & Purification 8 (1994) 131.

[90] R. E. Buxbaum and T. L. Marker, Hydrogen Transport through Nonporous Membranes of Palladium-Coated Niobium, Tantalum and Vanadium, J. Membr. Sci. 85 (1993) 29.

[91] N. M. Peachey, R. C. Snow, and R. C. Dye, Composite Pd/Ta metal membranes for hydrogen separation, J. Membr. Sci. 111 (1996) 123.

[92] K. S. Rothenberger, et al., Hydrogen permeability of tantalum-based membrane materials at elevated temperature and pressure., Abstracts of Papers of the American Chemical Society 224 (2002) U583.

[93] U. S. D. o. Energy, Fuel Cell Handbook, Morgantown, WV, 2000.

[94] H. Yokoyama, H. Numakura, and M. Koiwa, The solubility and diffusion of carbon in palladium, Acta Materialia 46 (1998) 2823.

[95] J. W. Park and C. J. Altstetter, The Diffusivity and Solubility of Oxygen in Solid Palladium, Scripta Metallurgica 19 (1985) 1481.

[96] A. D. LeClaire, Ch. 8: Diffusion of C, N, and O in metals in Diffusion in Solid Metals and Alloys, Springer-Verlag, New York, 1990.

[97] L. J. Gillespie and L. S. Galstaun, The palladium-hydrogen equilibrium and new palladium Hydrides, Journal of the American Chemical Society 58 (1936) 2565.

[98] H. Bruning and A. Sieverts, The electrical resistance of hydrogen charged palladium filaments between 160 degrees and 310 degrees., Zeitschrift Fur Physikalische Chemie-Abteilung a-Chemische Thermodynamik Kinetik Elektrochemie Eigenschaftslehre 163 (1933) 409.

[99] H. Frieske and E. Wicke, Magnetic Susceptibility and Equilibrium Diagram of Pdh, Berichte Der Bunsen-Gesellschaft-Physical Chemistry Chemical Physics 77 (1973) 48.

[100] J. R. Lacher, A theoretical formula for the solubility of hydrogen in palladium, Proceedings of the Royal Society of London Series a-Mathematical and Physical Sciences 161 (1937) 0525.

[101] J. R. Lacher, The statistics of the hydrogen palladium system, Proceedings of the Cambridge Philosophical Society 33 (1937) 518.

[102] C. Wagner, On the solubility of hydrogen in palladium compounds., Zeitschrift Fur Physikalische Chemie-Leipzig 193 (1944) 407.

[103] G. Alefeld, Phase-Transitions of Hydrogen in Metals Due to Elastic Interaction, Berichte Der Bunsen-Gesellschaft Fur Physikalische Chemie 76 (1972) 746.

[104] J. D. Eshelby, In *Solid State Physics,* Academic Press, New York, 1956.

[105] R. P. Griessen, In *Hydrogen in Disordered and Amorphous Solids,* Plenum Press, New York, 1986.

[106] Brodowsk.H, Das System Palladium/Wasserstoff, Zeitschrift Fur Physikalische Chemie-Frankfurt 44 (1965) 129.

[107] Brodowsk.H, Non-Ideal Solution Behavior of Hydrogen in Metals, Berichte Der Bunsen-Gesellschaft Fur Physikalische Chemie 76 (1972) 740.

[108] R. P. Griessen and T. Riesterer, Hydrogen in Intermetallic Compounds I, Springer, Berlin, 1988.

[109] T. Massalski, Binary Alloy Phase Diagrams, ASM International, Materials Park, OH, 1990.

[110] O. W. Richardson, J. Nicol, and T. Parnell, The diffusion of hydrogen through hot platinum., Philosophical Magazine 8 (1904) 1.

[111] C. J. Smithells and C. E. Ransley, The diffusion of gases through metals, Proceedings of the Royal Society of London Series a-Mathematical and Physical Sciences 150 (1935) 0172.

[112] C. J. Smithells and C. E. Ransley, The diffusion of gases through metals. IV. The diffusion of oxygen and of hydrogen through nickel at very high pressures, Proceedings of the Royal Society of London Series a-Mathematical and Physical Sciences 157 (1936) 0292.

[113] J. S. Wang, On the diffusion of gases through metals, Proceedings of the Cambridge Philosophical Society 32 (1936) 657.

[114] R. Ash and R. M. Barrer, Permeation of Hydrogen through Metals, Philosophical Magazine 4 (1959) 1197.

[115] R. J. Behm, K. Christmann, and G. Ertl, Adsorption of Hydrogen on Pd(100), Surf. Sci. 99 (1980) 320.

[116] M. A. Pick and K. Sonnenberg, A Model for Atomic-Hydrogen Metal Interactions - Application to Recycling, Recombination and Permeation, J. Nucl. Mater. 131 (1985) 208.

[117] D. A. King and M. G. Wells, Reaction-Mechanism in Chemisorption Kinetics - Nitrogen on (100) Plane of Tungsten, Proc. Roy. Soc. Lond. A 339 (1974) 245.

[118] P. Kisliuk, The Sticking Probabilities of Gases Chemisorbed on the Surfaces of Solids, J. Phys. & Chem. Solids 3 (1957) 95.

[119] P. Kisliuk, The Sticking Probabilities of Gases Chemisorbed on the Surfaces of Solids .2., J. Phys. & Chem. Solids 5 (1958) 78.

[120] R. J. Behm, et al., Evidence for Subsurface Hydrogen on Pd(110) - an Intermediate between Chemisorbed and Dissolved Species, J. Chem. Phys. 78 (1983) 7486.

[121] H. Conrad, G. Ertl, and E. E. Latta, Adsorption of hydrogen on palladium single crystal surfaces, Surf. Sci. 41 (1974) 435.

[122] J. F. Lynch and T. B. Flanagan, An investigation of the dynamic equilibrium between chemisorbed and absorbed hydrogen in the palladium/hydrogen system, J. Phys. Chem. 77 (1973) 2628.

[123] H. Yoshida, S. Konishi, and Y. Naruse, Effects of Impurities on Hydrogen Permeability through Palladium Alloy Membranes at Comparatively High-Pressures and Temperatures, J. Less-Common Met. 89 (1983) 429.

[124] A. S. Darling, Hydrogen Separation by Diffusion Through Palladium Alloy Membranes, Symposium on the Less Common Means of Separation (1963)

[125] H. Yoshida, S. Konishi, and Y. Naruse, Preliminary Design of a Fusion-Reactor Fuel Cleanup System by the Palladium-Alloy Membrane Method, Nuclear Technology-Fusion 3 (1983) 471.

[126] H. Amandusson, L. G. Ekedahl, and H. Dannetun, The effect of CO and O-2 on hydrogen permeation through a palladium membrane, Appl. Surf. Sci. 153 (2000) 259.

[127] H. Amandusson, L. G. Ekedahl, and H. Dannetun, Hydrogen permeation through surface modified Pd and PdAg membranes, J. Membr. Sci. 193 (2001) 35.

[128] A. B. Antoniazzi, A. A. Haasz, and P. C. Stangeby, The Effect of the Surface-State on the Permeation of Hydrogen through Palladium, Journal of Vacuum Science & Technology a-Vacuum Surfaces and Films 5 (1987) 2325.

[129] A. B. Antoniazzi, A. A. Haasz, and P. C. Stangeby, The Effect of Adsorbed Carbon and Sulfur on Hydrogen Permeation through Palladium, J. Nucl. Mater. 162 (1989) 1065.

[130] E. Wicke and J. Blaurock, New Experiments on and Interpretations of Hysteresis Effects of Pd-D2 and Pd-H2, J. Less-Common Met. 130 (1987) 351.

[131] E. Wicke and J. Blaurock, Equilibrium and Susceptibility Behavior of the Pd/H2 System in the Critical and Supercritical Region, Berichte Der Bunsen-Gesellschaft-Physical Chemistry Chemical Physics 85 (1981) 1091.

[132] A. Bejan and A. D. Kraus, Heat Transfer Handbook, John Wiley & Sons, 2003.

[133] R. K. Shah and A. L. London, Supplement 1 to Advances in Heat Transfer, Academic Press, New York, 1978.

[134] J. A. Basford, et al., Recommended Practice for the Calibration of Mass Spectrometers for Partial-Pressure Analysis, Journal of Vacuum Science & Technology a-Vacuum Surfaces and Films 11 (1993) A22.

[135] Y. A. Balovnev, Rules of Hydrogen Diffusion in Palladium, Zhurnal Fizicheskoi Khimii 48 (1974) 719.

[136] B. H. Howard, et al., Hydrogen permeance of palladium-copper alloy membranes over a wide range of temperatures and pressures, J. Membr. Sci. 241 (2004) 207.

[137] S. A. Koffler, J. B. Hudson, and G. S. Ansell, Hydrogen Permeation through Alpha-Palladium, Transactions of the Metallurgical Society of Aime 245 (1969) 1735.

[138] B. D. Morreale, et al., The permeability of hydrogen in bulk palladium at elevated temperatures and pressures, J. Membr. Sci. 212 (2003) 87.

[139] F. J. Ackerman and G. J. Koskinas, Model for Predicting Permeation of Hydrogen-Deuterium Inert Gas-Mixtures through Palladium Tubes, Industrial & Engineering Chemistry Fundamentals 11 (1972) 332.

[140] F. J. Ackerman and G. J. Koskinas, Permeation of Hydrogen and Deuterium through Palladium-Silver Alloys, Journal of Chemical and Engineering Data 17 (1972) 51.

[141] M. Nishikawa, et al., Permeation rate of hydrogen isotopes through palladium-silver alloy, Journal of Nuclear Science and Technology 33 (1996) 774.

[142] D. W. Hoffman and J. A. Thornton, Internal-Stresses in Cr, Mo, Ta, and Pt Films Deposited by Sputtering from a Planar Magnetron Source, Journal of Vacuum Science & Technology 20 (1982) 355.

[143] J. A. Thornton, Influence of Apparatus Geometry and Deposition Conditions on Structure and Topography of Thick Sputtered Coatings, Journal of Vacuum Science & Technology 11 (1974) 666.

[144] B. A. Movchan and A. V. Demchisin, Study of the Structure and Properties of Thick Vacuum Condensates of Nickel, Titanium, Tungsten, Aluminum Oxide and Zirconium Dioxide, Fiz Metallov i Metalloved 28 (1969) 653.

[145] R. Messier, A. P. Giri, and R. A. Roy, Revised Structure Zone Model for Thin-Film Physical Structure, Journal of Vacuum Science & Technology a-Vacuum Surfaces and Films 2 (1984) 500.

[146] L. R. Shaginyan, et al., Evolution of film temperature during magnetron sputtering, Journal of Vacuum Science & Technology A 24 (2006) 1083.

[147] R. Kirchheim, Hydrogen Solubility and Diffusivity in Defective and Amorphous Metals, Progress in Materials Science 32 (1988) 261.

[148] R. Kirchheim, et al., Hydrogen in Amorphous and Nanocrystalline Metals, Materials Science and Engineering 99 (1988) 457.